(Annual Report) 1998-1999

1. Depth Encoding of Point-of-interaction in Thick Scintillation Cameras

Takehiro Tomitani, Yasuyuki Futami, Yasushi Iseki[1], Shigeru Kouda[2], Teiji Nishio[3], Takeshi Murakami, Atsushi Kitagawa, Mitsutaka Kanazawa, Eriko Urakabe, Munefumi Shinbo and Tatsuaki Kanai
([1]Toshiba Co., [2]Instit. Molecular Science, [3]Nat. Cancer Center)
Keywords: *gamma camera, position arithmetic, maximum likelihood estimate*

The secondary beam generator/separator was built last year at HIMAC, from which positron emitting nuclei beams such as ^{10}C, ^{11}C, ^{18}Ne and ^{19}Ne are available. We intend to develop a positron camera to image end point distribution of positron emitting beams. Scintillation cameras have been adopted in such fields as PET, positron cameras and gamma ray astronomy. In these applications, thick NaI(Tl) crystals are adopted to image high energy gamma rays and collimators are not used, which causes a two-dimensional position error that depends on depth-of-interaction. In principle, depth-of-interaction can be obtained from the depth dependency of light distribution. The present study theoretically analyzed the possibility of the detection for depth encoding of point-of-interaction.

Three-dimensional position arithmetic can be derived from maximum likelihood estimation. Here we assume that the number of photoelectrons generated at the photocathode of a photomultiplier (PMT) follows Poisson distribution. Photons emitted at position (x, y, z) in the crystal are shared among PMTs. Let n_k denote the number of photoelectrons generated at the k-th PMT and $\lambda_k(x, y, z)$ denote its ensemble average. Then the likelihood, L, that m PMTs detect $\{n_1, n_2, ..., nm\}$ photoelectrons is

$$L(n_1, n_2, ..., nm|x, y, z) = \prod_{k=1}^{m} p_k(nk|x, y, z), \qquad (1)$$

where p_k, Poisson distribution, is by definition

$$p_k(nk|x, y, z) = \frac{\lambda_k{}^n}{n_k!} e^{-\lambda k}. \qquad (2)$$

A sufficient condition which maximum likelihood estimate (MLE), $(\hat{x}, \hat{y}, \hat{z})$ must satisfy is

$$\frac{\partial \ln L}{\partial x} = \sum_{k=1} \frac{\partial \lambda_k}{\partial x}\left(\frac{n_k}{\lambda_k} - 1\right) = 0,$$
$$\frac{\partial \ln L}{\partial x} = \sum_{k=1} \frac{\partial \lambda_k}{\partial y}\left(\frac{n_k}{\lambda_k} - 1\right) = 0,$$
$$\frac{\partial \ln L}{\partial x} = \sum_{k=1} \frac{\partial \lambda_k}{\partial z}\left(\frac{n_k}{\lambda_k} - 1\right) = 0, \qquad (3)$$

MLE, $(\hat{x}, \hat{y}, \hat{z})$, is determined from this set of equations. Note that each equation is implicitly dependent on x, y and z through λ (x, y, z) and transcendental, and hence can only be solved numerically by Newton-Raphson's approximation.

Depth resolution depends on the light distribution, that strongly depends on the mechanism of reflection on the reflector. In the case of perfectly diffusive reflection, the light distribution has a broad maximum near the reflector and the estimate of depth is two-valued, so that the depth cannot be determined. If the reflector is a mirror whose reflection coefficient ranges from 0 to 1, then the depth dependency of the light distribution is monotonic and depth information is available. 3D spatial resolutions are shown in Fig. 1 as function of depth,

in which reflection coefficients are 1 (left side graphs), and 0 (right side graphs), respectively. In view of 2D position arithmetic, perfectly diffusive reflection is superior to mirror reflection, yet depth information cannot be derived. Depth information can be obtained in the case of mirror reflection with reflection coefficients ranging from 0 to 1, that is, opaque to mirror reflection at a cost of 2-D spatial resolution. The choice seems dependent on the pposes of a particular application. For parallax correction, moderate depth information may suffice, while in other applications such as gamma ray astronomy, depth information may be more important to determine the gamma ray direction.

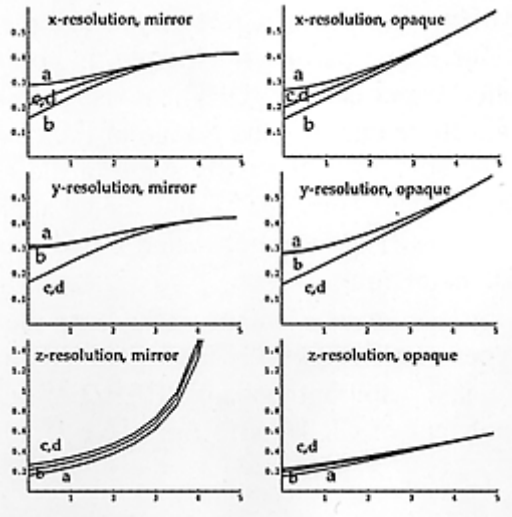

Fig.1. Spatial resolution as a function of light source depth. The ordinate is spatial resolution in cm FWHM and the abscissa is depth in cm. Curves a, b, c and d refer to the positions just under the center of a PMTs in the x-direction, midway between two adjacent PMTs in the y-direction and midway among three OMTs, respectively.

2. Track Sensitivity and Surface Roughness Measurement of CR-39 Surface with Atomic Force Microscope

Nakahiro Yasuda , Mikio Yamamoto, Mieko Kurano, Kuniaki Amemiya [1], Hiroyuki Takahashi [1] and Koichi Ogura [2]([1] Univ. of Tokyo; [2] Nihon Univ.)

Keywords: *CR-39, atomic force microscope, roughness measurement, track sensitivity*

Research on lowering CR-39 track registration threshold is important in order to extend its application fields. The CR-39 (HARZLAS (TD-1)) manufactured by Fukuvi Chemical Industry Co. Ltd., Japan has the high sensitivity to low LET (Linear Energy Transfer) particles, recording normally incident protons up to the energy of 20 MeV. Recently, new CR-39 (TNF-1) developed by Ogura et al. (1997) can record normally incident protons up to the energy of 27 MeV. Since these tracks are observed as shallow tracks, it is difficult to distinguish them from background of the rough surface caused by chemical etching. Moreover, the ragged mouth of the track and locally non-uniform etching cause fluctuation in track sensitivity and limit the charge and mass resolution of CR-39 as a consequence. By clarifying the relationship between sensitivity and roughness of the surface, it is possible to improve efficiently the sensitivity and quality of the surface of CR-39. By using the AFM (atomic force microscope) technique, in contrast to the optical microscope (OPT), it is possible to observe a three-dimensional profile of the track and the etched surface in the early stage of the etching process. In this study, AFM has been applied to evaluate the surface roughness and track sensitivity for CR-39 detectors.

The surface measurements have been done for three types of CR-39, pure CR-39 (BARYOTRACK), CR-39 doped with antioxidant (HARZLAS (TD-1)) and copolymer of CR-39/NIPAAm (TNF-1); all were manufactured by Fukuvi Chemical Industry Co. Ltd., Japan. The samples of CR-39 were prepared by cutting a sheet (0.9 mm thick) into square-shaped pieces of 1 x 1 cm^2. These pieces were etched in 7N NaOH solution at 70°C using a water bath incubator. The etching time was varied from 1 to 24 hours. The surface roughness was measured by AFM. In order to compare the track sensitivity, two types of CR-39 (BARYOTRAK and TD-1) were exposed to several kinds of heavy ions from shown in Table.1. These samples were etched in 7N NaOH solution at 70°C for 24 hours. The track etch pits were measured by AFM and OPT.

The surface roughness was evaluated using the RMS roughness (Rq). The surface of BARYOTRAK is almost flat even if the etching time is prolonged, while the surface roughness of TD-1 and TNF-1 becomes significant with passage of etching time. It was experimentally and quantitatively confirmed that the CR-39 having high sensitivity shows a rough surface after etching and the CR-39 with low sensitivity keeps its good surface quality even for a long etching time. Fig.2 shows AFM images of a track etch pit with the surface profiles on BARYOTRAK and TD-1. The samples were irradiated with 200 MeV/n Ne ions and etched for 24 hours. Due to the rough surface, the shape of the track edge on TD-1 is not so clear in contrast to BARYOTRAK. A ragged feature appears on the fringe of the opening mouth of the track on TD-1 in the cross-sectional image of a track. The curing conditions of polymerization for TD-1 and BARYOTRAK were the same, but differed from TNF-1. The monomer used for the polymerization of TD-1 and BARYOTRAK was purified in order to exclude oligomers. The surface roughness and the track sensitivity would be affected by the difference in the manufacturing process of the materials.

The variations of sensitivities are summarized with ion energy in Table.1. The track sensitivities of BARYOTRAK are lower than those of TD-1 and BARYOTARCK shows a steep response for the LET value in contrast to TD-1. Its track registration threshold is about 40 keV/μm. An inverse correlation was experimentally confirmed between the track sensitivity and the roughness of the detector surface after etching, i.e. the surface of CR-39 with high sensitivity is roughened by etching, while the BARYOTRAK with low sensitivity keeps its original surface clarity, even for a long etching. The characteristics of BARYOTRAK, such as the surface clarity and the steep response curve, are expected to make it ideal for the detection of cosmic-ray Fe isotopes.

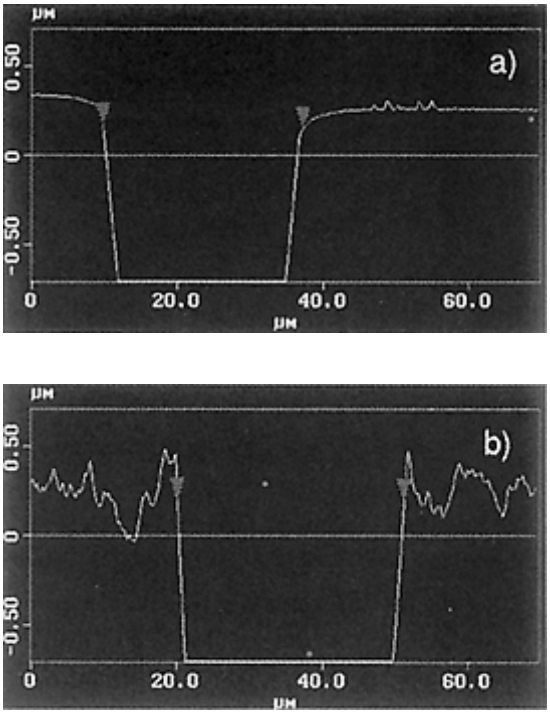

Fig.2. AFM images of a track etch pit with the surface profiles on BARYOTRAK(a) and TD-1(b).
The samples were irradiated with 200MeV/n Ne ions and etched for 24 hours.
Height scale perpendicular to the fetector surface was normalized to 1.4 μm.

Table 1. The results of sensitivity measurements.

Exposed ion	Energy (MeV/n)	REL_{200eV} (MeV cm^2)	Sensitivity BARYOTRAK	Sensitivity TD-1
Ne	200	233	0.05 ± 0.01	0.83 ± 0.03
Si	470	296	0.11 ± 0.01	0.86 ± 0.07
Ar	530	466	0.74 ± 0.05	1.49 ± 0.07
Ar	200	783	2.95 ± 0.18	4.05 ± 0.39

Publications:

1) Takahashi H., Amemiya K., Yasuda N., Yamamoto M., et al.: Nucl. Inst. and Meth., A422, 751-755, 1998.
2) Yamamoto M., Yasuda N., et al.: Nucl. Inst. and Meth., B152, 349-356, 1999.

3. Quantitative Evaluation Method for Lung Tumor with Fractal Analysis of X-ray CT Images

Mikio Yamamoto[1], Mieko Kurano[1], Ryohei Ogawa[1,2], Hideya Fukuoka[3] Hironao Kawashima[2], Hironobu Ohmatsu[4], Noriyuki Moriyama[5]

([1]NIRS; [2]Keio Univ.; [3]Tokyo Univ. of Agriculture; [4]National Cancer Center Hospital East; [5]National Cancer Center Hospital)

Keywords: *lung tumor, fractal dimension, helical X-ray CT*

It is important to provide a qualitative diagnosis of malignancy or benignancy in diagnosing a lesion in the lung area. Introducing image processing into the qualitative diagnosis have contributed to diagnosis for early treatment. With development of a newer X-ray CT scanner, high quality diagnosis can be expected using image processing. In this study, we used the morphological features of the intratumoral division structure and the property of the tumor limb (boundary between a tumor and the circumference of a normal lung). The quantification of the quality of the umor in the lung area was tried using its outside (exterior) and inside (interior) features.We used chest X-ray CT images from the National Cancer Center Hospital. Images were photographed using a helical X-ray CT scanner. Only the lung piece was reconstructed with 512x512 pixels in an image. The slice (1mm interval) image was obtained under the conditions that the X-ray beam was 2mm wide and the CT value was in the region of -4096HU and +3046. We
looked at 15 cases (six benign examples, nine malign zed. 2) It is reasonable to suspect lung cancer on spiculation, corona radiata and a notch with deep lobation. 3) A benign tumor (hamartoma) takes on the shape of a well-defined circular limb. In order to distinguish the benign tumor from a malignant tumor, we tried quantification in the marginal region using the degree of gray-change and the shape factor. We confirmed that the gray-change was clear and the shape factor was high for a benign image, but the gray-change was complicatedly irregular and circular shape was low for a malignant image. As shown in Fig.3, the degree of gray-change can be extracted by the total number of gray level gradient directions.
For quantification in an interior tumor, differential diagnosis with the benign growth lesion is difficult for poorly differentiated adenocarcinoma and squamous cell carcinoma since they show the solid growth shadow. Dispersion and uniformity of the gray level in the intratumoral division are also noticed, making interpretation difficult. We then noted the value of each pixel of image datum, since a locationally approached pixel has a relation to other pixels. As treatment, which quantified the aspect of this arrangement, we tried quantification using a fractal dimension and entropy analysis. The fractal dimension analysis may possibly show complexity of the surface shape in a noninteger dimension, and the entropy analysis shows uniformity of the image.
We chose the central part of five slices from each case, and used a total of 75 slices. The number of the gray level gradient directions, the fractal dimension, and the entropy were placed in the three-dimensional space from the tumor division in each slice. The secondary discriminant function (three-dimensional space is divided by cutting it into a secondary curve) was used as discriminant of the benign and malignancy groups. As a result of these analyses, we were able to distinguish benign and malignant tumors at probabilities of 93.3% and 97.7%, respectively. The morphological analysis using these indexes seems to be effective for the qualitative diagnosis of the tumor. In the future, we will examine a practical application by adapting many cases with a minute analysis for an individual index.

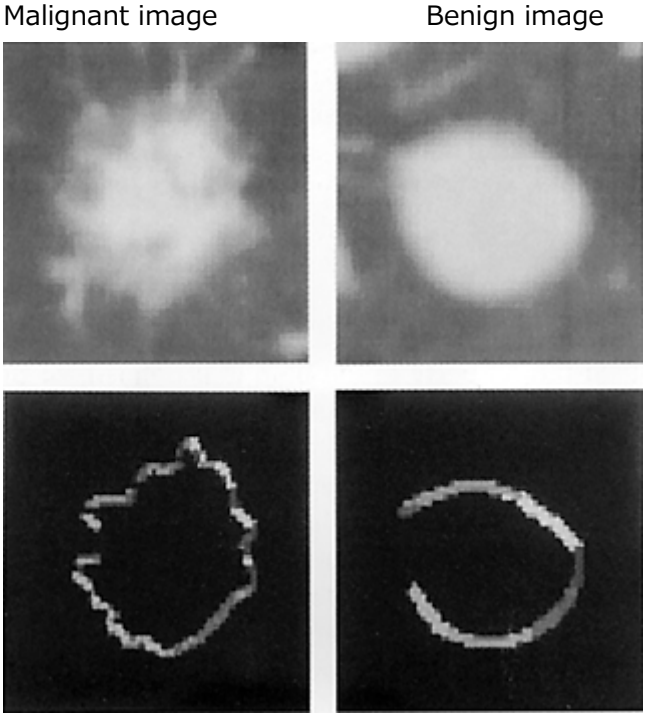

Fig.3. Extraction of the gray level gradient directions.

4. New Method for High Resolution Autoradiography Using CR-39 Solid State Track Detectors and Atomic Force Microscopy

Kuniaki Amemiya[1,2], Nakahiro Yasuda[1], Mikio Yamamoto[1], Hiroyuki Takahashi[2], Masaharu Nakazawa[2] and Koichi Ogura[3]

([1]NIRS; [2]Univ. of Tokyo; [3]Nihon Univ.)

Keywords: *CR-39, atomic force microscope, radiography; autoradiography*

Recently, the atomic force microscope (AFM) has been applied to measurements of very small etch pits on CR-39 solid state track detectors. In this technique, the CR-39 is etched for a short time and then the etched surface is scanned with the AFM. The technique also allows high resolution imaging of charged particle tracks without a complicated setup and it is expected to be applicable to high resolution charged particle autoradiography.

Autoradiographic applications often require accurate positioning between the sample and the particle tracks in order to determine the radiation dose distribution inside the sample. As a fiducial marker for positioning, aluminum patterns were deposited on the CR-39 surface using a photolithography technique. The marked CR-39 was etched in 7N NaOH solution at 70°C for 5 minutes. The aluminum pattern was dissolved during the etching process leaving pattern-shaped steps on the surface of the CR-39 detector as shown in Fig. 4. The level difference of the step was about 70 nm. Thus, it is a suitable marker that can be measured using AFM and positioning between the sample and the etch pits in autoradiography should be possible with good accuracy.

The resolution of the imaging mentioned above is determined by the size of the etch pits which can be observed with the AFM. A small CR-39 (BARYOTRAK-P) cut into 1 x 1 cm^2 was irradiated with 1 MeV helium ions using the Tandetron accelerator at RCNST. Irradiated CR-39 was etched in 7N NaOH solution at 70°C for 2 minutes and observed with the AFM. Fig. 5 shows a typical cross-sectional view of an etch pit observed with the AFM. The diameter of the mouth of the etch pit was about 80 nm. In this condition, the position resolution of imaging for the charged particle track was 30 nm (FWHM). Because the intrinsic resolution of the AFM is extremely high, varying etching conditions (i.e. the concentration and the temperature of etchant and the etching time) should make the etch pit smaller than in the present result. The surface roughness of BARYOTRAK-P was about 2 nm even after etching process. Therefore the ultimate resolution of this method was thought to be of the order of several nanometers.

This method provides a new technique for subcellular scale radiation imaging that is required in microdosimetry.

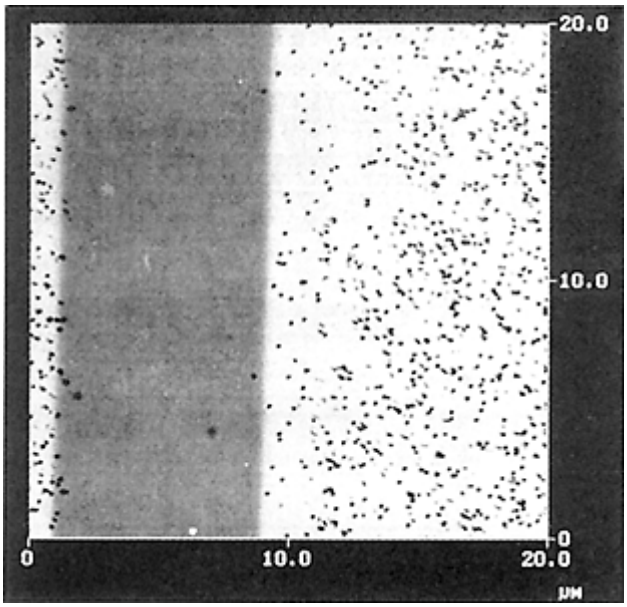

Fig.4. The AFM image of the dark band of the pattern with etch pits for 1 MeV carbon ions.

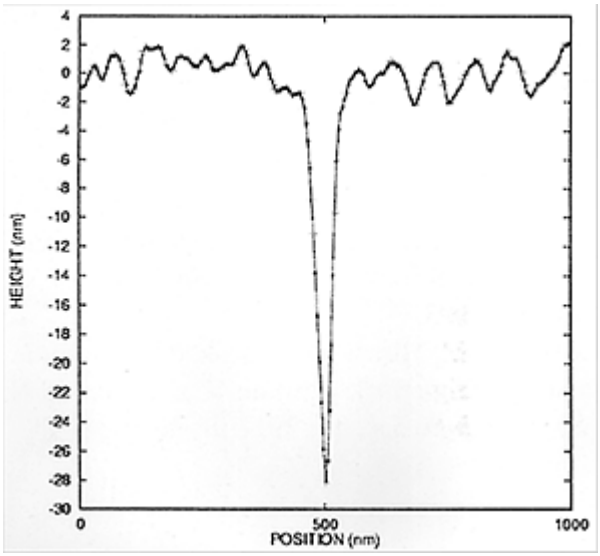

Fig.5. The cross-sectional AFM image of an etch pit for 1MeV helium ions.

Publications:

1) Takahashi H., Amemiya K., Nakazawa M., Yasuda N., Yamamoto M., et al.: Nucl. Instr. and Meth., A422, 751-755, 1999.

2) Amemiya K., Takahashi H., Nakazawa M., Yasuda N., Yamamoto M., Ogura K., et al.: Nucl. Instr. and Meth., B, in press.

5. Categorization with Temperature Distribution of the Human Hand Surface

Hideyuki Kokubo, Mikio Yamamoto, Masahiko Hirasawa and Junko Taniguchi

Keywords: *skin surface, palm, 2-dimensional pattern, categorization, thermal vision*

It is known that serotonin of the pineal body increases when NATase activities are blocked by external qi. A rise of serotonin concentration in blood leads to a blood flow increase and the temperature of the body surface becomes higher than that during rest. Particularly in studies by thermal vision, the temperature of the human hand surface is often measured as an indicator of the peripheral blood flow change. However, the degree of the increase of temperature is assumed to be dependent on differences of the peripheral blood flow distribution in the skin. These differences show variations of the patterns of temperature distribution of the body surface. The authors surveyed patterns of 2-dimensional temperature distributions on the palm surface of 81 healthy volunteers during rest. The sampled population showed that females' had an average temperature of 32.4 degree, and it was 0.6 degree higher than that of males ($p<0.01$). There was no correlation between age and temperature ($r=0.07$). Differences in patterns of 2-dimensional distributions showed all data can be classified into four groups (Fig. 6): 1) high temperature in the middle of the palm (C); 2) high temperature at both thenar and hypothenar eminences (TH); 3) intermediate type (CT); 4) combination type (CTH). Average temperatures differed 2-3 degrees for the types, but not for sex in each type. There was a weak correlation between age and temperature for the group of high temperature at both eminences ($r=0.32$), but other groups had no correlation ($r<0.2$).

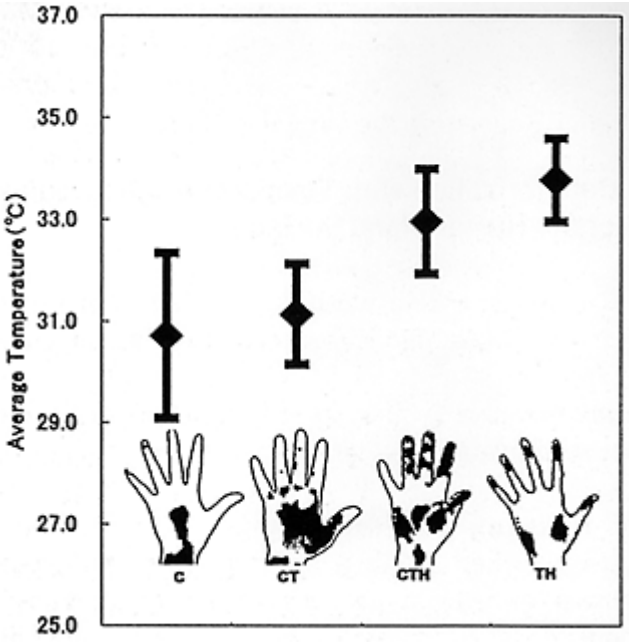

Fig.6. Average temperature of the hand surface and patterns.

Publications:

1) Kokubo H, Taniguchi J, Yamamoto M and Hirasawa M: J. Intl. Soc. Life Info. Sci., 16, 247-254, 1998.

6. EEG Analysis of Implicit Perception in External Qigong

Mikio Yamamoto, Masahiko Hirasawa, Hideyuki Kokubo, Kimiko Kawano* and Tomoko Kokado

(*Nippon Medical School, Tokyo)

Keywords: *implicit perception, qigong, somatic sensation, EEG*

We analyzed electroencephalograms (EEGs) of healthy volunteers who experienced external qigong without normal sensory transmission.

The short distance condition: a Chinese qigong master (sender), who claimed to emit external qi from his hands, put his right hand into a metal box, covered by a cloth, on a table. A receiver (healthy volunteers) was eye-masked and his/her hand was laid over the box without contact. A screen was placed between the sender and the receiver. The sender emitted external qi during a randomly selected half minute period in a continuous one minute period and the receiver attempted to perceive the time zone. In over 20 trials for the receivers' right/left hands, the receivers were unable to guess the correct sending time zone with any statistical significance. However, a statistically significant difference was observed on the alpha wave mean amplitude in receiver's EEGs between the sending and non-sending time zones at the corresponding region to their somatic sensory area in a period of 13 to 17 seconds from the start of the task.

The long distance condition (approximately 11 m): a Japanese qigong master (sender) and his pupil (receiver) were placed in two different rooms in a sensory-shielded state. The sender attempted to transmit external qi within a few seconds at a randomly selected time in a 80-second period. The receiver, who was seated in an electromagnetic shielded cage, attempted to perceive the transmission time and pushed a switch to record her guessed time. In over 30 trials, the receiver's guessed time was not statistically significant for the sending time. However, the analysis of the receiver's EEG from 20 seconds before to 20 seconds after the qi emission showed that a statistically significant increase of alpha wave mean amplitude at the C3 point occurred around 15 seconds after starting qi emission. The C3 point corresponds to the sensory area of the right hand in which the receiver held the switch.

We suggest that the receivers' EEG changes were caused by implicit perception. Additionally, response areas of EEG were inferred to be affected by the receivers' attention.

Publications:

1) Yamamoto M, Hirasawa M, Kokubo H, Kawano K, Kokado T, Hirata T and Yasuda N: J. Intl. Soc. Life Info. Sci., 15, 88-96, 1997

2) Yamamoto M, Kokado T, Hirasawa M, Kawano K, Kokubo H and Sakaida H: J. Intl. Soc. Life Info. Sci., 16, 274-283, 1998.

3) Yamamoto M, Hirasawa M, Kokado T, Kokubo K, Yamada T, Taniguchi J, Kawano K and Fukuda N: J. Intl. Soc. Life Info. Sci., 17, 191-197, 1999.

7. Studies on Dosimetry for Therapeutic Carbon Beams

Akifumi Fukumura, Takeshi Hiraoka, Kaname Omata, Mitsue Takeshita, Yutaka Noda, Kiyomitsu Kawachi, Tatsuaki Kanai, Takeshi Murakami, Naruhiro Matsufuji, Yasuyuki Futami and Guenther H. Hartmann*

(*DKFZ, Germany)

Keywords: *carbon beam, dosimetry, range, fragmentation*

Since 1994, the National Institute of Radiological Sciences (NIRS, Japan) has been carrying out clinical trials of cancer treatment using high-energy carbon ion beams. Establishing carbon beam dosimetry is essential to performing the trials. Objects of this studies include absolute dosimetry, relative dosimetry, range measurements and beam attenuation due to nuclear fragmentation.

Regarding the absolute dosimetry, we employed three different methods, ionization chamber, calorimeter and fluence measurement methods. Measurement were performed at zero depth for 290 MeV/u carbon beams with the ionization chamber and fluence methods, and at a depth of 12 cm in water for 6-cm modulated 290 MeV/u carbon beams with the calorimeter and ionization chamber methods. Values obtained with the different methods were in good agreement with each other. In particular, the discrepancy between results by the ionization chamber and calorimeter methods was less than 1 %. We also carried out dosimetry intercomparison between two groups from different carbon beam facilities, NIRS and GSI-DKFZ in Germany. Values estimated individually by each group were in good agreement, within 0.5 %. The consistency established an international common framework for carbon beam dosimetry.

Carbon beam treatment requires not only absolute dosimeter, but also relative dosimetry. Several characteristics of small p-type silicon diodes were investigated with irradiation of heavy ion beams. The diodes showed favorable characteristics as relative dosimeter in terms of stability for carbon beam irradiation. The diodes were applied to practical verification of the treatment planning in the pre-clinical examination carried out at HIMAC.

In an ordinary range measurement, a combination of a phantom and detector is employed. Such a measurement requires much time and an assumption of constant range during it. We developed a simple range measurement method using visible rays generated in a bare plastic scintillator block. This method allows real-time measurements with high spatial resolution of less than 0.5 mm.

We also investigated nuclear fragmentation of carbon beams. Attenuation of carbon beams caused by fragmentation in an energy absorber may possibly change the fluence of carbon beams which is planned for patient irradiation. The survival of primary carbon beams after passing through an absorber was measured with Δ E plastic scintillator. The results showed that polyethylene and PMMA were water-equivalent in terms of the nuclear reactions and appropriate as energy absorbers to shift the range of the primary beams. The charge-changing cross sections of several materials for carbon beams were also deduced from the slope of the attenuation.

Publications:

1) Fukumura A.: Doctoral dissertation, Tohoku Univ., 1999

2) Fukumura A., Hiraoka T., Omata K., Takeshita M., Kawachi K., Kanai T., Matsufuji N., Tomura H., Futami Y., Kaizuka Y. and Hartmann G. H.: Phys. Med. Biol. 43, 3459-3463, 1998.

3) Fukumura A., Noda Y., Omata K., Hiraoka T., Futami Y., Matsufuji N., Murakami T. and Kanai T.: Nucl. Instr. and Meth. in Phys. Res. A 416, 148-151, 1998.

8. Measurement of Absorbed Dose by Solid Calorimeter

Kaname Omata, Takeshi Hiraoka, Suoh Sakata, Akifumi Fukumura and Mitsue Takeshita

Keywords: *calorimetry, dosimetry, carbon calorimeter, absorbed dose, radiation detector*

To determine an absorbed dose for proton and heavy ion beams, a quasi adiabatic solid calorimeter with a carbon absorber was designed and constructed. The absorber was a graphite block with 2.5cm diameter and 4mm thickness.

For the purpose of heat insulation the absorber was covered with a carbon jacket which was fixed inside an acrylic vacuum chamber, and then installed inside a Styrofoam box which was evacuated by a rotary pump for several hours before the measurement. The absorber contained three thermistors, one was used as a detector for the absorbed energy which appears as a temperature rise and the other two were electrical temperature calibrators. DC bridge was used for measuring change of resistance of the thermistors installed inside the absorber. The electrical calibrations without irradiation, done between every real measurement with irradiation, determine the calibration factors which convert the change of the potential difference of the bridge caused by the heat due to irradiations to the energy delivered to the absorber. Tolerance for radiation damage of the thermistors was checked by irradiation of 1kGy delivered to five thermistors of the same type as used for the carbon calorimeter in a Ne-20 beam of 123.8MeV/u with LET of 62.4keV/mm and no change was recognized in the response of temperature versus resistance of the thermistors before and after irradiation.

The variance of coefficient of the calibration factors acquired above was less than 0.4%, which means the calibrations can be done with good reproducibility. The measurement showed even the dose rate of 0.5Gy/min caused a change of 10 μV per minute in the potential difference of the bridge. It was confirmed the system had a sufficient reliability to make measurements of absorbed dose in a particle beam for dose rate larger than 0.5Gy/min.

Voltage output of the bridge was amplified by a nano-voltmeter, and data of 7-digit precision were acquired through the GPIB interface and analyzed by means of personal computers. The method allowed the change of the potential difference of the balanced bridge to be acquired as digital data and to be processed statistically. It reduced uncertainty of measured values and it made objective evaluation of the results possible. It should be noted measurements can be carried out with better precision than before even under conditions with much noise induced electromagnetically. Although it is difficult to handle the thermistors, for example with respect to the thickness of the lead wires because the thermistors themselves are very small, they are useful probes with respect to characteristics of temperature response and toughness against irradiation. The whole circuit sysytem for measurements was digitized, measured values were acquired by means of personal computers and an attempt was made to have automatic processing of acquisition and analysis of data as far as possible, for example in the data analysis a calculation code for absorbed dose was prepared. As a result of the automatic processing, there was a drastic improvement in analysis of data and carrying out measurements through a big cut in labor needed for these tasks.

Publications:

Omata, K., Hiraoka, T., Sakata, S., Fukumura, A., Takeshita, M.: Jpn. J. Med. Phys. 18, 327-332, 1998.

9. Physical Performance of a PET Scanner with Adjustable Data-acquisition Parameters

Hideo Murayama and Tomoyuki Hasagawa*

(*Kitasato Univ.)

Keywords: *three-dimensional data acquisition, positron emission tomography, nuclear medicine*

The three-dimensional (3D) mode of a positron emission tomography (PET) scanner offers a high sensitivity, but undesirable problems have arisen due to the larger axial field-of-view (FOV) with retracted septa. In the 3D mode, scatter fraction and random coincidence increase, and spatial resolution and sensitivity differ from the center to the circumference of the FOV. In one of the latest 3D PET scanners, ECAT EXACT HR+, the data-acquisition parameter defining the largest absolute difference in ring numbers accepted in coincidence detection (maximum ring difference or mrd), which is closely related to the acceptance angle, can be defined. In addition, there are other adjustable data-acquisition parameters which affect the physical performance.

Measurements were performed in principle by the National Electrical Manufacturers Association (NEMA) protocol with minor modifications. An acrylic cylindrical vessel phantom (20 cm inner diameter and 18.5 cm inner length) was set at the center of the scanner. It was filled with water containing F-18 radioactivity of 1.6 kBq/ml. Plane sensitivities were calculated from total counts of sinogram planes. For the 3D mode, the single slice rebinning algorithm was used to define the sinogram planes. The plane sensitivity in the 3D mode for various mrd parameters is shown in Fig.7. The flat region was about one-third of the total axial FOV in the default condition of data acquisition. The total sensitivity, as a function of mrd, showed that the default parameters had higher sensitivities close to the maxima.

A stainless steel needle (1.0 mm inner diameter and 1.5 mm outer diameter) filled with water containing F-18 radioactivity was positioned parallel to the scanner axis at various radial distances to the central axis. Images were reconstructed using a ramp filter with a cut-off at the Nyquist frequency and transverse spatial resolutions were calculated as the full width at the half maxima. A plastic tube (1.4 mm inner diameter and 5 mm long) filled with water containing F-18 radioactivity was positioned vertical to the scanner axis in the tangential direction. Axial spatial resolution was measured at five radial distances of 0, 5, 10, 15, and 20 cm, and at seven axial positions corresponding to plane numbers of 2, 7, 12, 17, 22, 27, and 32. The transverse spatial resolution in the tangential direction was almost independent of the radial position, while that in the radial direction increased with the radial position. There was discontinuous degradation toward the end planes in the 3D mode. The central flat regions were smaller for large radial distances. For larger mrd values, the axial spatial resolution was markedly degraded in the off-center region.

This study clarified the importance of understanding scanner performance dependence on data-acquisition parameters. The results are useful for maximizing the efficiency of PET measurements by selecting better acquisition parameters for each specific clinical application.

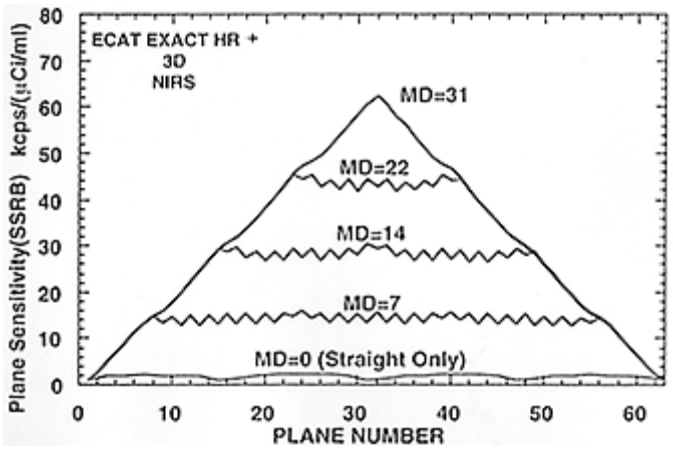

Fig.7. Plane sensitivity as a function of the plane number for various maximum ring difference (mrd) values in the 3D mode.

Publications:

Hasegawa, T., et al.: IEEE Trans. Nucl. Sci., 46, 652-658, 1999.

10. Essential Dynamics of DNA Repair Enzyme T4 Endonuclease V

J.G. Siebers and Hiroshi Yamaguchi

Keywords: *T4 endonuclease V, molecular dynamics, essential dynamics*

The exposure of DNA to ultraviolet (UV) radiation is an important mechanism that causes the production of pyrimidine dimers which are lethal and mutagenic for organisms. T4 endonuclease V acts as a repair enzyme for the thymine photodimer lesions of double- stranded DNA. We have conducted a 600 ps molecular dynamics simulation, including 100 ps for temperature and density adjustment as well as system equilibration, to study the properties of this system in detail.

The essential dynamics (ED) method was used to reduce the multidimensional configurational space to a subspace of only about 10 degrees of freedom. To achieve this the C backbone atoms were chosen to represent the slow motions of the protein. For this selection the average structure and the covariance matrix of the fluctuations about the average were calculated. Diagonalization of the covariance matrix gives eigenvectors and eigenvalues, where a small subset accounts for more than 90% of the overall vibrational motion of the protein. These eigenvectors span the essential subspace and are of particular interest.

The left hand drawing in Fig. 8 shows the secondary structure of T4 endonuclease V obtained from crystallographic data along with its water accessible surface. For the active sites GLU23, ARG3, ARG22, and ARG26, the side chain atoms are also displayed. The right hand drawing shows snapshots of the C atoms moving along the first essential eigenvector. We note the relative rigidity of the protein in the region of the active sites.

In the next step of this study we will compare the essential subspaces of T4 endonuclease V with the essential subspaces of the mutants E23Q and R3Q.

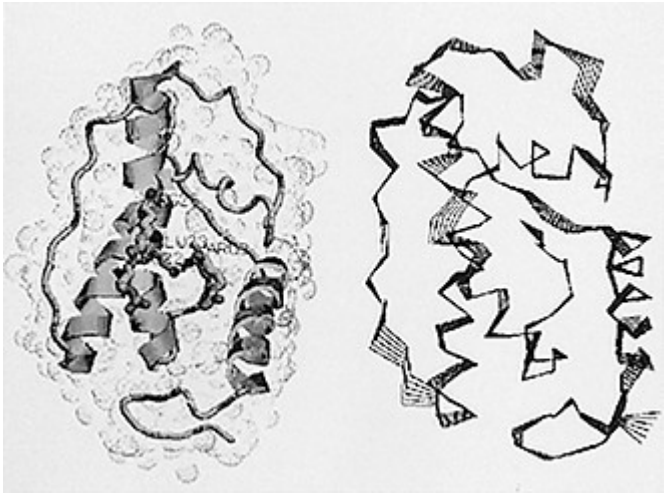

Fig.8. The left hand drawing shows the secondary structure and the water accessible surface of T4 endonuclease V.

The right hand one shows snapshots of the C atoms moving along the first essential eigenvector.

11. Comprehensive Study on the Fragment Reaction of Relativistic Heavy Charged Particles for Heavy Ion Radiotherapy

Naruhiro Matsufuji, Toshiyuki Kohno and Tatsuaki Kanai

Keywords: *beam quality, fragments, LET, particle identification, radiotherapy*

The production of projectile fragments is one of the important, but not yet completely solved, problems to be considered when planning for the utilization of high-energy heavy charged particles for radiotherapy. The aims of this study are to experimentally investigate fluence of the fragments and LET spectra produced from various incidents to elucidate the physical quality of the beams. The results are also compared with those by a fragment reaction simulation code to identify weakness of the code (L. Sihver et al.: Jpn. J. Med. Phys. 18, 1-21 (1998)).

An experiment was carried out at a beam port for biological experiments at HIMAC. Incident beams were as follows: 150 MeV/n ^{4}He; 290 MeV/n ^{12}C; 400 MeV/n ^{20}Ne; 490 MeV/n ^{28}Si; and 550 MeV/n ^{40}Ar. A beam was broadened in the same manner as in the case of therapy, i.e., both laterally and axially by a pair of wobbler magnets and a ridge filter, respectively.

PMMA, as a substitute for the human body, was used as a target. A binary filter made of PMMA plates was installed 300 mm upstream from the irradiating point. A ΔE-E counter telescope with a NE102 plastic scintillator (5 mm in thickness) and a BGO scintillator (300 mm in thickness) was positioned at the irradiating point to identify the kind of fragment particles based on differences in the elements. To monitor any gain drifting of the ΔE-E counters, stabilized green light emitted from a 1N6094 LED was used.

A gas-flow proportional counter was combined with the counter telescope system to measure LET spectra. P10 (Ar-90% / CH_4-10%) was used as a counting gas because it has the most uniform gas multiplication among other easily-obtained gases. Besides, stopping power of P10 gas relative to water for carbon ions can be regarded as being constant within 3 % even in a non-relativistic energy region. The thickness of the gas layer was 5 mm at NTP. Energy loss of a 290 MeV/n beam of carbon ions in the 5 mm thickness of P10 gas equals that in a 6.9 μm thick film of liquid water, which is close to the thickness of an individual cell.

The energy of the primary particles after passing through any thickness of PMMA was deduced by comparing its depth-dose profile measured with a parallel-plate ionization chamber with results calculated by the fragment reaction simulation code.

Response of the BGO and NE102 scintillators were obtained in this energy region for the first time. Particle-species dependency of the responses was parameterized by AZ^2 of the incident particles. Fragment particles produced between incident particles and the PMMA target were well identified down to hydrogen by the ΔE-E scatter plot, and the fluence of each fragment element was deduced. The difference between experimental and simulation code results suggests the need for theoretical research and the establishment of a reliable

nuclear reaction model in this energy region. The LET spectra were also derived for each element (Fig.9). These results indicate that the greater part of the dose is delivered by primary particles, though many light fragments are produced.

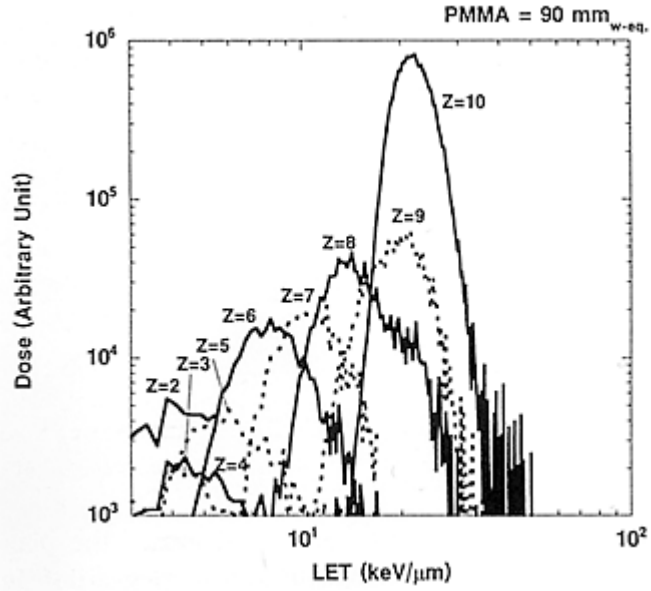

Fig.9. LET spectra of 400 MeV/n - ^{20}Ne beam fir each fragment element at PMMA thickness of 90mmw-eq.

Publications:

1)Matsufuji, N., Kanai, T. and Kohno, T. submitted to Rad. Res.

2) Matsufuji, N., Kanai, T., Komami, H. and Kohno, T. Nucl. Instr. and Meth. In Phys. Res. A in press.

3) Matsufuji, N., Kanai, T., Komami, H. and Kohno, T. Nucl. Instr. and Meth. In Phys. Res. A 430, 60-68, 1999.

4) Kohno, T., Kiyota, T., Matsufuji, N. and Kanai, T. Nucl. Instr. and Meth. In Phys. Res. A in press.

12. Comparison between Calculations and Experimental Data for a Microbeam Technique

Yukio Sato and Fuminori Soga

Keywords: *cell killing, microbeam technique, quadratic dependence, high-LET, single track*

Recent results on cell killing with a microbeam technique were analyzed using three parameters (k, L, L_1, where *k* is the mean number of lethal particles per cell nucleus, L [keV/μm] is the track-average LET in cells, and L1 [keV/μm] is a critical value for inducing lethal damage by a single track. Analysis showed that the model calculation $\{k(L/L_1)^2=1\}$ is consistent with two data sets from Pugliese and from Hei.

Findings obtained with the model are as follows: a quadratic dependence on the LET of the cellular effects (LET^2) is clear in the high-LET region between 30-500 keV/μm; L1 of 152 ± 0 keV/μm gives the best fit for the results of broad-beam experiments with light ion species from boron to neon, and the sensitive area of cell nucleus (A) is 49 ± 3 μm^2 for Chinese hamster V79 cells; RBE reaches a maximum at around L=170 keV/μm ($1.12L^1$), and the obtained A value agrees well with the Pugliese's result (49 ± 7 μm^2). In microbeam experiments on cell killing with several MeV α particles, the relationship between k and L for V79 cells is expressed as $L = 152(k)^{-1/2}$.

Under a given survival level (37%), we studied the difference in the required LET (L) between the microbeam and conventional broad-beam experiments. Results are shown in Fig.10. For Pugliese's data set, L of 4.3MeV α particles was evaluated as 105 keV/μm, under which we calculated the critical k-value as 2.1 ± 0.1. This value agrees well with his value of 2.2 ± 0.3 obtained for Chinese hamster V79 cells. Hei's result is 3.7 for human-hamster hybrid (A_L) cells using 5.5MeV α particles with L of 90 keV/μm. This value is somewhat larger than the value we calculated (2.9 ± 0.2). Taking account of the experimental variation in different cells (V79 and A_L cells), Hei's result is not far from our calculation. Using Maclaurin expansion L(n), expressed as $L_1\{-\ln(1-1/n)\}^{1/2}$ for n > 1 in broad-beam experiments, we can rewrite the model as $L(n) = L1(n^{-1} + 1/2n^{-2} + 1/3n^{-3} + 1/4n^{-4} + - - - -)^{1/2}$. In microbeam experiments $\{ L_1(1/k)^{-1/2}\}$ corresponds to the first term of this expansion. We note that L(n) is always larger than L(k), suggesting that many over-killed cells with several traverses are involved in broad-beam experiments, particularly with high-LET region. Experimentally, both n and k are the effective (in average) numbers per cell nucleus, however their characteristics are quite different; n is mainly considered as the effect of a stochastic property in particle hits, while k is attributed to effects of the energy spread and fluctuation in radiosensitivity of individual cells.

In conclusion, the expression of $L = 152(k)^{-1/2}$ is applicable for analyzing single-track events of V79 cells under the conditions at high-LET and with light ion beams.

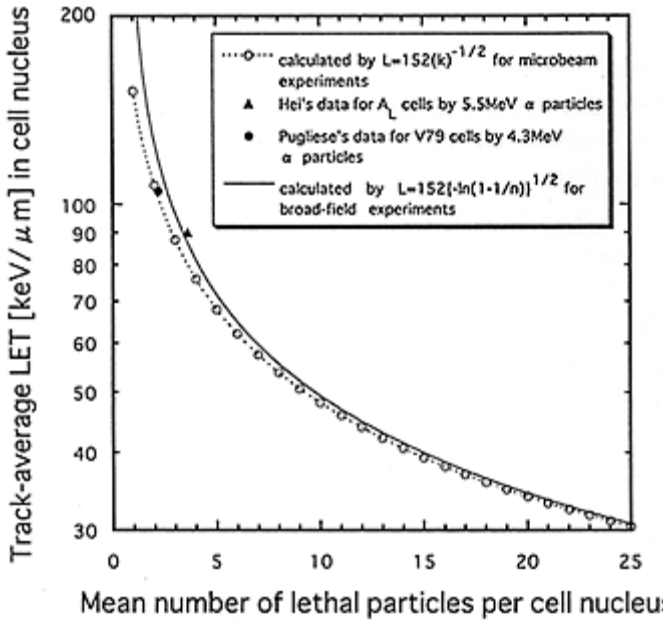

Fig.10. Calculated critical number of traversed heavy ions per cell nucleus of V79 cells vs. their track-average LET[keV/μ] in cells. The dotted line shows values calculated by $L=152(k)^{-1/2}$ for microbeam experiments (each symbol ○ corresponds to an integer). The solid line shows values calculated by $L=152\{-\ln(1-1/n)\}^{1/2}$ for broad-beam experiments.

The area above the curve is the lethal region. ● and ▲ are Pugliese's results (2.2 at 105 keV/μm) and Hei's results (3.7 at 90 keV/μm), obtained using Chinese hamster V79 cells and human-hamster hybrid (A_L) cells, respectively.

Publications:

[1] Sato Y. and Soga F.: Int. J. Radiat. Biol., 75, 1015-1019, 1999.

13. A Build-up Model for Thickness Gauging of Steel Plates Based on Gamma-ray Transmission

Yoshiyuki Shirakawa

Keywords: *build-up effect, thickness gauging, steel plate, gamma-ray transmission, linear attenuation coefficient*

A non-linear build-up model for thickness gauging of steel plate, which is based on a gamma-ray transmission technique, has been proposed. Its performance was evaluated by experiments using a real ^{137}Cs thickness gauge installed on a heavy plate mill used in steel manufacturing.

A conventional gamma-ray thickness gauge employs many linear measurement models as given by eq. (1),

$$I=I_0\exp(-\mu X_i) \quad (1)$$

where I_0 and I are the number of incident gamma-rays and the number of transmitted ones respectively, $\mu(cm^{-1})$ is a linear attenuation coefficient of measured objects, in this case steel plates, and X_i (cm) is thickness in the i-th measuring range. The models deal with only a small measurement range each and the same number of standard steel plates is needed for model parameter calibration.

The proposed model with a variable linear attenuation coefficient (cm^{-1}) is shown in eq. (2),

$$I=I_0\exp(-\mu(X)X),\ \mu(X)=(\mu_0/\beta)[\exp(-\alpha X)+(\beta-1)] \quad (2)$$

where μ_0 is the ideal linear attenuation coefficient obtained under the condition of $X\rightarrow 0$, and α and β are positive constants given by previous experiments, includes build-up effects in $\mu(X)$. Although it is a little more complicated to solve X in eq. (2) than in eq. (1), the new model has advantages that it can cover a much wider range of measurements and it requires a fewer calibration plates.

It was shown that the values calculated with the non-linear model of eq. (2) were in good agreement with experimental data obtained by the gamma-ray thickness gauge in the range of 0-10cm thickness. The relative accuracy of thickness measurements was within ± 0.05% and the absolute accuracy was within ± 2 μm in the thickness range of 0-10cm. Hence the new model has a potential for real use in current thickness gauging and meets requirements of simplicity and easy handling.

Publications:

1)Shirakawa Y., Horikoshi K. and Amano H.: SICE,35,5,693-695,1999.
2)Shirakawa Y., Horikoshi K. and Amano H.:IMEKO-15th,TC-14,165-170,1999.

14. Estimation of Distance between the Metal Complex Ion and the Closest Solvent Water Molecules from Density Data

Katsumi Kurotaki

Keywords: *aqueous solution, metal complex, density*

Contrary to Archimedes' principle, the level of water in a test tube drops when electrolytes such as $CuSO_4$ are dissolved in the water and dissociate into ions. This is due to the interaction between ions and water molecules around the ions; water molecules in the hydrogen-bonded network of water are oriented toward an ion by the strong electrostatic force of the ion leading to an increase of packing fraction of water molecules and an abnormal negative V^0 calculated from density data for these ions, where V^0 is the molar volume of ion at infinite dilution in water. Electrolyte solution theory predicted the magnitude of the electrostatic effect on V^0. However, the V^0 of multivalent metal ion deviates from the theoretical one because multivalent metal ions interact with water molecules by coordination bond formation as well as electrostatic force. On the other hand, the metal complex ions and peroxyanions, $[ML_n]^{z\pm}$ whose M have no electrons for a bond with water molecules, interact with water in a purely electrostatic way (where M is metal ion of all kinds, L is NH_3, diamine/2, F^-, Cl^-, CN^-, NO_2^- and O, $1 \leqq z \leqq 4$). Then the V^0 of $[ML_n]^{z\pm}$ was analyzed on the basis of electrolyte solution theory and scaled particle theory (SPT). For a series of $[ML_n]^{z\pm}$ having an identical L, linear relationships are observed between the M-X bond distance, r_{MX} and the intrinsic volume, $V_{cav}(ML_n)$ which is equal to the volume of water displaced by them, where X is the coordination atom. The value of $dV_{cav}(ML_n)/dr_{MX}$ increased with increasing r_{MX}. These data were analyzed with the model of an MX_n core where the sphere M* (radius r_{M*}) is overlapped by n spheres (radii r_X) which are apart by r_{MX} from M. Assuming that $r_{M*} = (r_{MX} + r_X)\cos\theta$, a self-consistent set of r_{M*} and θ is determined from the experimental value of $dV_{cav}(ML_n)/dr_{MX}$ which is equal to $\cos\theta\, dVcav(M*_{sphere})/dr_{M*}$, where θ is the angle between the MX bond and the closest water molecules in contact with M*. The sum of r_{M*} and the radius of water molecule (155 pm), r_w is equal to the distance between M and the closest water molecules, $r_{Mw'2}$. Table 2 shows the values of $r_{Mw'2}$, $n_{w'2}$ and $dV_{cav}(ML_n)/dr_{MX}$, where $n_{w'2}$ is the hydration number. These data are consistent with the structural data determined by X-ray diffraction. This is the first evidence that there is a clear relationship between thermodynamic and structure data for aqueous electrolyte solution.

Table 2. Structural data of the aqueous solutions of $[ML_n]^{z\pm}$} determined from the solution densities.			
	$dV_{cav}(ML_n)/dr_{MX}$ / $cm^3\ mol^{-1}\ pm^{-1}$	$rM_{w'2}$, pm^{-1}	$n_{w'2}$
$[MF_6]^{z-}$	0.54	393	13-14
$[M(am)_6]^{z+}$ $[M(CN)_6]^{z-}$ $[M(ox)_3]^{z-}$	0.62	407	13-14
$[MCl_6]^{z-}$	0.83	461	13-14
MO_4^{z-}	0.32	359	11

am is NH_3 or diamine/2, ox is ethane-1,2-dioato ion.

Publications:

Kurotaki, K. and Kawamura, S.: J. Chem. Soc. Faraday Trans., 94, 2939- 2943, 1998.

15. The Oxidation of Linoleic Acid by Copper(II) Complexes

Jun-ichi Ueda and Toshihiko Ozawa

Keywords: *linoleic acid, copper(II) complexes, lipid peroxidation, HPLC*

The oxidation of lipid by active oxygen species or metal ions has been hypothesized to play a critical role in diverse biological processes including carcinogenesis and radiation damage. Then, we intended to investigate how linoleic acid, one of the main constituents of lipid in membrane, is oxidized by metal ions such as Cu(II) complexes. The following Cu(II) complexes were used: $Cu(BC)_2$ (BC: bathocuproine); $Cu(CyHH)_2$ (CyHH: cyclo(L-histidylhistidyl)); $Cu(OP)_2$ (OP: o-phenanthroline); Cu(HGG) (HGG: L-histidylglycylglycine): and $Cu(en)_2$ (en: ethylenediamine).

Lipid peroxidation proceeds through a chain reaction initiated by the abstraction of a hydrogen atom from polyunsaturated fatty acids containing unconjugated 1,4-dienes to yield conjugated dienes with a characteristic UV absorption around 234 nm. The absorbance at 234 nm observed during Cu(II)-catalyzed oxidation of linoleic acid increased with incubation time, reached a maximum level, and decreased thereafter. HPLC chromatograms due to oxidation products indicated the appearance of peaks corresponding to four isomers of linoleic acid hydroperoxide (LOOH) and subsequent complete decomposition of LOOH. The time to reach the maximum absorbance at 234 nm within 24 h was in the following order: $Cu(II)(BC)_2$ > $Cu(II)(CyHH)_2$ = $Cu(II)(OP)_2$ > $Cu(II)(en)_2$ > Cu(II)(HGG). This result suggests that $Cu(II)(BC)_2$ can produce LOOH from linoleic acid more rapidly than Cu(II)(HGG) and it can decompose the LOOH generated more easily. Also lipid peroxidation, i.e. the formation of lipid hydroperoxide, may depend on the redox potential of Cu(II) complexes, since that of $Cu(II)(BC)_2$ of 620 mV (versus NHE) is the highest among the five Cu(II) complexes and the redox potentials of the other four Cu(II) complexes have the following order: $Cu(II)(CyHH)_2$ > $Cu(II)(OP)_2$ > Cu(II)(HGG) > $Cu(II)(en)_2$. It has been reported that the change in redox potential of copper markedly influenced the rate of oxidation of lipids induced by copper.

Further, whether the decomposition of LOOH was caused by these Cu(II) complexes was investigated. The absorbance at 234 nm due to LOOH, which was separately synthesized from the reaction of linoleic acid with soybean lipoxygenase, decreased rapidly with incubation time in the presence of Cu(II) complexes. HPLC also indicated the disappearance of LOOH and the appearance of unidentified degradation products.

These results suggest that Cu(II) complexes can not only oxidize linoleic acid, but also decompose LOOH generated from it.

16. Stereoselective Synthesis of Alexine Stereoisomers from (S)-Pyroglutamic Acid

Nobuo Ikota and Hidehiko Nakagawa

Keywords: *polyhydroxylated pyrrolizidine alkaloid, glyosidase inhibitor, (S)-pyroglutamic acid, diastereoselective allylation, chiral synthesis*

Alexines1 are polyhydroxylated pyrrolizidine alkaloid with a carbon substituent at C-3 and five adjacent asymmetric carbons. They have been shown to possess interesting biological activities such as inhibitory activity toward glucosidase and antiviral activity. In a continuation of our synthetic studies to utilize optically active pyroglutamic acid derivatives for natural product synthesis, we describe here a stereocontrolled synthesis of 1-epialexine 11 and 1,7-diepialexine 12 via a non-carbohydrate based approach utilizing (S)-pyroglutamic acid derivative (Fig. 11).

An enone 3was obtained by the reaction of (3R,4R,5R)-1-(tert-butoxycarbonyl)-3,4-isopropylidenedioxy-5-trityloxymethyl-2-pyrrolidinone 2, prepared from the unsaturated lactam 1 by dihydroxylation with a catalytic amount of OsO_4 in the presence of N-methylmorpholine N-oxide followed by isopropylidenation, with vinylmagnesium bromide in tetrahydrofuran (THF) at -40 to -50°C in 93% yield. Redution of 3 with NaBH4 in the presence of CeC_3 in MeOH gave an allylic alcohol 4 as a mixture of diastereomers in 91% yield. Mesylation of 4 followed by cyclization with potassium tert-butoxide in THF gave the pyrrolidine 5 as an inseparable diastereomeric mixture in 68% yield, from which the diols 6 and 7 were isolated by treatment with ozone followed by NaBH4 reduction in EtOH in 60% and 25% yields, respectively.

The carbon unit required for the pyrrolizidine ring was introduced using a diastereoselective allylation of the aldehyde derived from the alcohols 6 and 7. 6 was oxidized by the method of Swern to afford the corresponding aldehyde , which was very unstable, and only a trace of aldehyde was obtained after aqueous workup. Therefore, allylmagnesium chloride in THF was directly added to the crude Swern oxidation mixture of 6 in THF at -78°C to afford allylic alcohols 8a and 9 in 52% and 25% yields after column chromatography, respectively. The hydroxy group in 8a was protected as the methoxymethyl ether (chloromethyl methyl ether, N,N-diethyl-aniline, methylene chloride), and selective transformation of the N-tert-butoxycarbonyl group in 8b into the N-benzyl group was done by treatment with tert-butyldimethylsilyltrifluoro-methane-sulfonate in the presence of 2,6-lutidine followed by successive treatments with tetrabutylammonium fluoride in THF and benzyl bromide in the presence of potassium carbonate in acetone to furnish 8c in 58% yield. Ozonolysis of 8c followed by reductive workup with $NaBH_4$ gave the alcohol 10 in 58% yield. Mesylation of 10 gave a mesylate, which was spontaneously cyclized to give the pyrrolizidine derivative. After hydrogenation of the protected pyrrolizidine with 10% palladium on carbon in EtOH under hydrogen in the presence of hydrogen chloride to remove the N-benzyl group, acidic treatment with 10% HCl-MeOH (1:1) at 70°C to cleave the acetonide and trityl groups afforded the 1-epialexine 11 ($[\alpha]D^{20}$ +34.8° (c=0.5, H_2O)), in 52% yield after purification by ion exchange chromatography (Dowex 50W-X8, H^+ form). By a parallel series of reactions, the allylic alcohol 9 was converted to 1,7-diepialexine 12($[\alpha]D^{20}$ +37.0° (c=0.7, H_2O), in 15% yield.

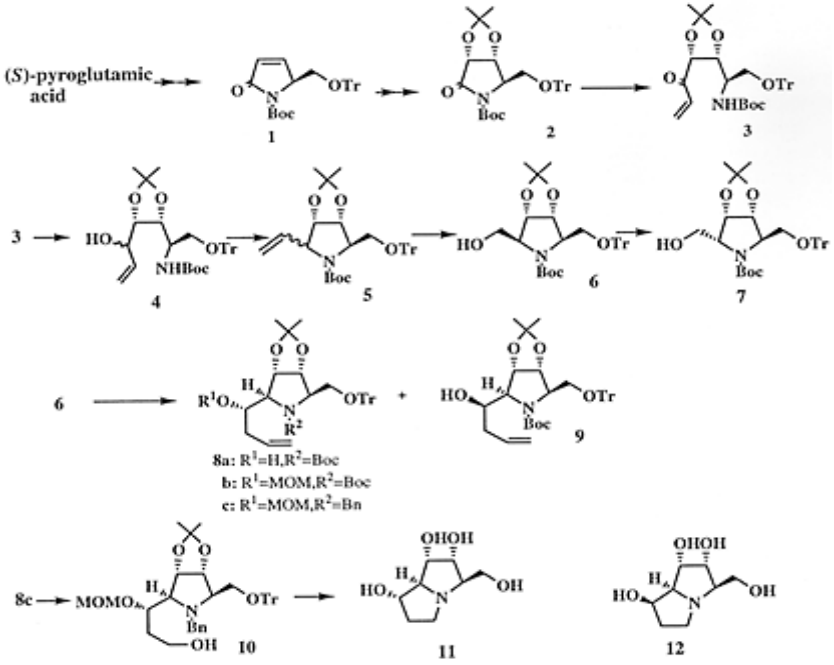

Fig.11. Synthetic scheme for 1-epi and 1,7-diepialexine.

Publications:

Ikota N., Nakagawa H., Ohno S., Okuyama K., Noguchi K. : Tetrahedron, 54, 8985-8998 , 1998.

17. Change of Redox Property of Cytochrome C by Peroxynitrite

Hidehiko Nakagawa, Yukiko Ohshima*, Nobuo Ikota and Toshihiko Ozawa

(*Kitasato University)

Keywords: *peroxynitrite, cytochrome c, oxidation, 5-methoxytryptamine, lipoic acid, photospectrometry*

Reactive oxygen species (ROS) and/or reactive nitrogen species (RNS) are considered to be involved in the pathogenesis of various diseases. Nitric oxide and superoxide, ROS/RNS species, are endogenous and important compounds in physiological reactions such as vasodilatation, signal transduction, and protection from infection. However, when overproduced, these compounds also have toxic effects on various endogenous biological substances. Peroxynitrite (PN) is a product from a rate-limiting reaction between nitric oxide and superoxide. It is considered to be produced not only in vitro, but also in vivo systems. PN production proceeds oxidative reactions with various biological components, so that PN is considered to cause various types of oxidative damage to tissues and cells, such as LDL oxidation, lipid peroxidation, DNA strand breakage, and so on. One of the most characteristic reactions of PN is the nitration of free tyrosine and protein tyrosine residues. The presence of nitrotyrosine in tissues or cell cultures is often used as a marker for the production of PN. In this study, the effect of peroxynitrite on cytochrome c, which is one of the components of the mitochondrial electron transfer system, was examined. The inhibitory effect of 5-methoxytryptamine and lipoic acid, which we previously reported are peroxynitrite scavengers, was also tested.

Peroxynitrite was synthesized from NaN_3 and ozone. Briefly, NaN_3 was dissolved in an alkaline solution adjusted to pH 12, followed by bubbling of an oxygen stream containing ozone while the solution was kept in an ice bath. After bubbling, the solution was frozen by cooling in a dry ice-acetone bath and stored at -20°C until use. The concentration of the peroxynitrite solution was determined spectrophotometrically by measuring of the absorbance at 302nm (ε =1670$M^{-1}cm^{-1}$). Hypoxanthine and xanthine oxidase were added to a solution of cytochrome c (0.02mM) or peroxynitrite-pretreated cytochrome. The redox status of cytochrome c was monitored by measuring absorbance at 550nm (the characteristic absorption band in the reduced form of cytochrome c). Cytochrome c was reduced once by superoxide, and then oxidized by hydrogen peroxide, which had been produced from the dismutation of superoxide, using the hypoxanthine/ xanthine oxidase system. The oxidation rate of the reduced form of cytochrome c was increased, dose-dependently, for pretreatment with peroxynitrite. This acceleration of the oxidation in cytochrome c was depressed by pretreatment with 5-methoxytryptamine or lipoic acid prior to the peroxynitrite treatment, but the rate was not changed by treatment with the oxidized form of glutathione. Because the treated peroxynitrite was considered to be completely decomposed until addition of the hypoxanthine/ xanthine oxidase system, the change of the oxidation rate was due to the modification of cytochrome c by peroxynitrite. This acceleration was effectively reduced by the pretreatment with 5-methoxytryptamine. Since the oxidation rate of the intact cytochrome c was not affected by 5-methoxytryptamine which is a selective inhibitor of the nitration of tyrosine residue, the modification of cytochrome c was assumed to be due to the nitration of tyrosine residues (Fig. 12).

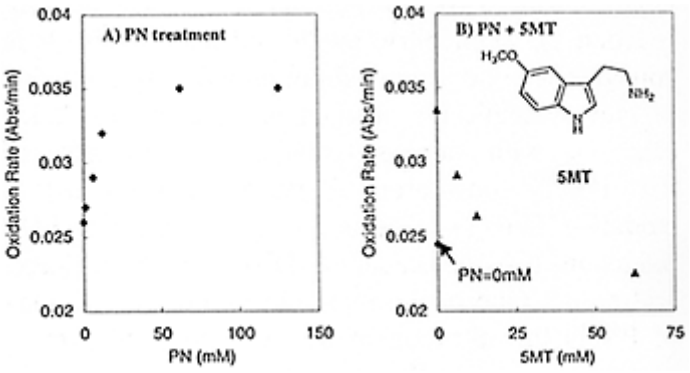

Fig.12. Oxidation rate of peroxynitrite-treated cytochrome c. Oxidation rate (change of absorbance at 550nm per minute) was determined from the reduction and oxidation reaction of cytochrome c with hypoxanthine and xanthine oxidase system. A) Oxidation rate of peroxynitrite-treated cytochrome c. B) Oxidation rate of 5MT (5MT: 5-methoxytryptamine) and peroxynitrite-treated cytochrome c.

Publications:

Nakagawa H., Sumiki E., Ikota N., Matsushima Y., Ozawa T.: Antiox. Redox Signaling, 1, 239-244, 1999.

18. Simple Removal of Iron by Non-ionic Resin of Macro-reticular Type from Chloride Solution

Kiyoko Imai, Kazuo Watari and Takao Morimoto*

(*Japan Chemical Analysis Center)

Keywords: *simple removal, iron, non-ionic resin, chloride solution, hydrochloric acid*

Solvent extraction is widely used as a separation or purification method in the fields of chemistry, pharmaceutice and biology. In particular, extraction by ether is often used for the removal of iron prior to radiochemical analysis, because ferric hydroxide is a coprecipitant of many radionuclides in various solutions. However, experimental techniques for solvent extraction are usually rather troublesome and time-consuming. Moreover, use of organic solvents has recently become an issue because of concerns with health effects, waste disposal and fire prevention.

We preciously found that ^{59}Fe, ^{68}Ga, and ^{198}Au as chloro complex anions (MCl_4^-) were peculiarly adsorbed on non-ionic macro-reticular resin (XAD-7 resin) from concentrated chloride solutions. An adsorption method using a granular resin is more effective and simpler than conventional solvent extraction and other methods. This report deals with the removal of iron by an adsorption method with XAD-7 in the place of solvent extraction by ether.

Effect of agitation time on adsorption of iron was first examined by a batch method, using 0.1g of XAD-7 and 10 ml of 8-9M hydrochloric acid containing 0.1mg of iron spiked with ^{59}Fe. Adsorption reached equilibrium within a 24-hour agitation.

Next, effect of concentration of iron carrier on adsorption was studied using 0.1g of XAD-7 and 10ml of 9M hydrochloric acid solution containing 0.02- 20.0mg of iron with a 24-hour agitation. Adsorption of iron was quantitative on XAD-7 from the solution with iron carrier below 0.1mg, and decreased with increasing iron carrier. From these results, we saw that the adsorption capacity of XAD-7 for iron is about 30mg per 1.0g of dried resin.

Under the same conditions, other elements, such as cobalt, zinc, nickel, were not adsorbed.

Based on the results obtained in the batch experiments, adsorption of iron by column operation was carried out using a column (1.2cm in diameter) containing 3.0g of XAD-7. One hundred ml of 8M hydrochloric acid solution containing 0.1 mg of iron carrier were passed through the column at various flow rates. Iron was adsorbed quantitatively at a flow rate below 1.5ml/min.

The iron adsorbed on the XAD-7 column was easily eluted with 0.1- 0.2M nitric acid solutions. We concluded that adsorption and desorption behaviors of iron on XAD-7 provide similar results as by extraction with ether and back extraction behavior with nitric acid.

The effect of hydrochloric acid concentration on adsorption of iron on XAD-7 and extraction of iron with isopropyl ether is shown in Fig.13. Adsorption and extraction of iron are similar in that they increase with concentration of hydrochloric acid and their maxima appear in 8-10M hydrochloric acid.

From this study, we showed that non-ionic resin (XAD-7) can be used for the effective separation of iron in place of solvent extraction by ether.

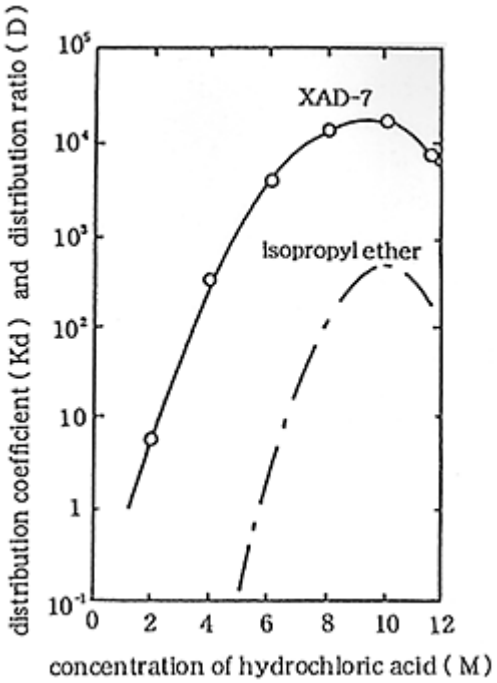

Fig.13. Relation between adsorption on XAD-7 and extration with isopropyl ether.

19. Radiation Effects on Phospholipase Signaling Pathways in Cultured Rat Liver Cells

Tetsuo Nakajima and Osami Yukawa

Keywords: *diacylglycerol, phospholipase C, phospholipase A_2, tyrosine phosphorylation, rat liver cells*

Our previous work demonstrated that radiation induces protein kinase C (PKC) activation due to translocation of PKC molecules from cytosol to membranes in cultured rat hepatocytes, and that the PKC activation is related to lipid peroxidation. In addition, we showed that radiation induces biphasic production of diacylglycerol(DAG), one of the endogenous PKC activators, in rat hepatocytes. On the other hand, it has been reported that the biphasic production of DAG is observed in the cases of treatment of cells with growth factors, H_2O_2 or UV and then DAG is produced by phospholipase C or D. We have already demonstrated that hydroxyl radical induces DAG production through phosphatidylinositol-specific phospholipase C(PI-PLC). Some oxidative stresses are known to induce activation of PLC-γ1, one of the PI-PLCs, through its tyrosine phosphorylation. In this study, PLC-γ1 phosphorylation in hydroxyl radical or radiation-induced DAG production was investigated. Additionally, we assessed radiation effects on phospholipase A_2(PLA_2), which is related to PKC activation and lipid peroxidation. Hydroxyl radical and radiation could not induce tyrosine phosphorylation of PLC-γ1 at the time when DAG was produced by hydroxyl radical or radiation. Therefore, the increase of DAG content by them seems to be through other PI-PLCs, or to be due to phosphorylation-independent PLC-γ1 activation. As for PLA_2, irradiation with 0.5 Gy to 50 Gy induced no change in PLA_2 activity within 3 hours after irradiation in cultured rat hepatocytes. However, in cultured non-parenchymal cells from rat liver, PLA_2 activity increased 1.5-fold 30 min after irradiation with 5 Gy and the increase was maintained for to 2 hours after irradiation. These results suggest that radiation effects on phospholipase signaling pathways in hepatocytes are different from those in liver non-parenchymal cells. Radiation effects on liver cells might be mediated by cell-to-cell interactions between hapatocytes and non-parenchymal cells, for example, through arachidonic acid.

20. Correlation between mRNA Structure of the Coding Region and Translational Pauses: Spider Silk Fibroin Spidroin 2

Mitsuo Zama

Keywords: *mRNA structure, translational pauses, spider silk fibroin*

Transient accumulations of discrete size nascent polypeptide chains during translational elongation have been observed for some proteins. This is due to pauses or discontinuities in the translational process, which may occur at specific sites in mRNA templates. In a series of studies for such proteins, silkworm fibroin, type I collagen, colicin A, chloroplast photosystem II reaction center protein D1 and globin, we have so far presented evidence to support the view that the pauses may be attributable to the mRNA secndary structure of the protein-coding region.

Discontinuous translational elongation of polypeptides is observed during spider dragline silk fibroin synthesis. The spider major ampullate (dragline) silk of Nephila clavipes consists of the two subunit proteins, Spidroin 1 and Spidroin 2. In the present study, we tried to analyze Spidroin 2, which exhibits an entirely different repetitive amino acid sequence motif than Spidroin 1, to examine the possible correlation between mRNA structure and translational pauses for this protein.

The repeating segment of Spidroin 2 consists of alternate alanine-rich and proline-rich regions. It was found that the calculated free energy of the secondary structure of Spidroin 2 mRNA per nucleotide for the alanine-rich region is about the same as that for the successive proline-rich region. The small stability changes of local mRNA secondary structures along the mRNA chain suggest that the translational pauses observed for dragline silk fibroin synthesis may not be correlated with Spidroin 2 mRNA structure, in contrast to Spidroin 1 mRNA structure which may explain the translational pauses as has been suggested in our preceding study.

21. Recognition and Organization of Specific DNA Structures by Human Chromatin-associating Factors

Masahiko Takahagi and Kouichi Tatsumi

Keywords: *DNA junction, DNA binding protein, chromatin organization*

Specific DNA structures are of interest as transient and activated states in the course of genetic processing. Since they occur at biological active sites, it is important to know their structures and metabolic processes. In particular, during DNA replication, recombination and repair, dynamic changes of DNA structure have been observed in both prokaryotes and eukaryotes. Many activities are known to link with specific DNA structures. In this study, we focused on a peculiar DNA junction structure, the "Holliday junction", which is an intermediate formed during recombination. It is a well known target not only because of its processing factors but also because of its architectural components like chromatin-relating factors. For example, non-histone proteins HMG1/ HMG2 have a specific affinity for the Holliday-like junction as well as for DNA bending sites, and they possess a cooperative potential with histone H1 or provide substitutive roles for it on chromatin template. Also, histone H1 preferentially binds to Holliday-like DNA junctions. These facts suggest that a sort of DNA junction is topologically equivalent to the putative looping cross-over which HMG1/2 and H1 can recognize at nucleosome linker sites, indicating that Holliday-like junctions are structural analogues to putative DNA looping at nucleosomal linkers. Recently, a specific interaction with Holliday-like junctions has been identified in another functional factor, SWI/SNF complex, which is involved in chromatin organization for transcriptional regulation.The biological significance of junction types of DNA makes it important to search for interactive proteins from human cell extracts. We separated major DNA binding proteins from cell nuclei through DNA affinity chromatographic procedures. In addition to five major chromatin-associating proteins, i.e. histone H1 nucleolin, hnRNP U, HMG1 and HMG2, DNA-dependent protein kinase catalytic subunit (DNA-PKcs) and Ku were identified as abundant elements. Gel mobility shifl assay with their purified preparations demonstrated that six of the proteins, excluding Ku, specifically bound to common junction types of DNA, suggesting that their targets could be shared and their functions may be associated.To analyze the putative molecular organization on damaged DNA, we developed a technique using formation of the molecular aggregate as a probe as is the case of matrix attachment region binding proteins including histone H1, Topoisomerase II and lamins. We found that human nuclear extract formed a selective aggregation with damaged types of DNA. Further, to separate the relating proteins from contaminant proteins and nucleic acids, DNA affinity column chromatography was carried out. We detected a series of proteins to co-aggregate with denatured types of DNA. According to the results of amino acid sequencing and western blotting, we identified the major components as DNA-PKcs, Ku and nucleolin.In order to confirm the potential to aggregate DNAs, their isolated preparation was tested. We observed an ability specific to nucleolin for single stranded DNAs, but not for double-stranded DNAs. Similarly, either DNA-PKcs or hnRNP U was able to aggregate single-stranded DNAs. This evidence emphasized that the three factors may be involved in the organization of common DNA targets.The existence of a multivalent DNA target for major nucleoproteins leads us to ask how they are functionally specialized and how they interact at the target sites; these are topics for future study.

22. Analysis of Plasmid DNA Structure after γ -irradiation by Atomic Force Microscope

Masahiro Murakami, Akira Furukawa, Kiyomi Eguchi-Kasai, Reiko Kanda, Hideo Hirokawa* and Isamu Hayata

(*Max-Planck Institute for Molecular Genetics, Germany)

Keywords: *DNA damage, atomic force microscope, plasmid DNA*

DNA damage (DNA single-strand break, DNA double-strand break, etc.) induced with ionizing radiation is considered one of the main causes of cell inactivation. Several methods including agarose gel electrophoresis, pulsed-field gel electrophoresis, neutral filter elution method, neutral sedimentation and electron microscopy have been applied to analyze this type DNA damage.

A new method employing an atomic force microscope (AFM) for nanometer-level structure analysis of DNA damage induced with γ-irradiation was established. Formal changes of plasmid DNA (about 3 kbp; length about 1μm) after irradiation with ^{60}Co γ-rays at doses of 1.9k, 5.6k, and 8.3kGy were visually analyzed by AFM. The tortile feature of the plasmid DNA was depicted better with AFM than with a transmission electron microscope (TEM). Three forms of plasmid DNA, closed circular (intact DNA), open circular (DNA with a single-strand break) and linear form (DNA with a double-strand break) were observed in the sample irradiated with γ-rays at the dose of 1.9kGy. On the other hand, in the samples irradiated with γ-rays at doses of 5.6 kGy and 8.3 kGy, open circular and linear forms were observed, but no closed circular form was observed. A shortening of the length of the linear form of DNA irradiated with 5.6kGy and 8.3kGy γ-rays was observed by AFM. The average lengths of the linear form of DNA irradiated with 1.9kGy, 5.6kGy and 8.3kGy of γ-rays were 0.96±0.06 μm, 0.69±0.04 μm and 0.69±0.04 μm, respectively. Shortening of the length of the linear form of DNA under experimental conditions of 5.6kGy and 8.3kGy γ-ray irradiation were significant when T-test was applied ($p<0.05$). The shortening of the linear form is possible as a result of the destruction of DNA secondary structure caused by complicated DNA damage, such as the combination of DNA single-strand break(s), DNA double-strand break or DNA base damage(s) on the same DNA molecule, induced with low LET-ionizing radiation. Shortening of the DNA strand has also been observed as a result of cisplatin-DNA interaction by TEM [Macquet JP, Butour JL. : Biochimie 60, 901-914, 1978] and AFM [Onoa GB, Cervantes G, Moreno V, Prieto MJ. : Nucleic Acids Research 26, 1473-1480, 1998]. The present observations support our interpretation, because DNA damage caused by cisplatin-DNA interaction other than multiple DNA double-strand breaks produces shortening of the DNA length. Our findings indicate the possibility that AFM imaging may be able to visualize a novel type of structural change to DNA following ionizing radiation, which is not observed by gel electrophoretic analysis.

23. Liver Damage and Oxidative Stress Caused by Irradiation of Heavy Ion Beams

Keizo Takeshita, Hideyuki Majima and Toshihiko Ozawa

Keywords: *in vivo ESR, radical, heavy ion beam, radiation, liver, reactive oxygen species*

Heavy ion beam irradiation is a promising therapeutic technique for inveterate cancers because of its excellent dose distribution and high biological effects. It is very important to know the damage mechanisms by heavy ion beams to prevent the damage of normal tissues and to obtain the best therapeutic effects. However, the damage mechanisms for normal tissues are not fully clear. To clarify them, we examined the relation of oxidative stress to liver damage caused by whole body irradiation of heavy ion beams to mice.

Heavy ion beams (290 MeV/u carbon beams, 6 cm spread-out Bragg Peak, 60 KeV/mm LET) were generated with the Heavy Ion Medical Accelerator at NIRS. Body weight and liver wet weight of mice decreased after more than 16 h with a 7.5 Gy irradiation. A remarkable increase of serum GOT was also observed 16 h after irradiation. Thiobarbituric acid-reactive substances (TBARS) in liver homogenates significantly increased more than 2 days after irradiation, indicating occurrence of lipid peroxidation in liver. The mortality was about 30 % on the 4th day after a 15 Gy irradiation, and liver TBARS of surviving mice were similar to those for the 7.5 Gy irradiation.

To evaluate enhancement of in vivo radical reaction, the in vivo ESR technique was used with a nitroxyl redox probe, 3-carbamoyl-2,2,5,5-tetramethylpyrrodine-1-yloxy (carbamoyl-PROXYL), which is known to be converted to an ESR-silent form by reaction with oxygen radicals and other reducing compounds. In vivo ESR measurements were made at the upper abdomen of mice immediately after intravenous injection of an aqueous solution of probe. Signal decay rate of probe (spin clearance) increased at 1-2 h after the 7.5 Gy irradiation and then decreased after more than 16 h. Spin clearance measured at 1-2 h after the 15 Gy irradiation was similar to that after the 7.5 Gy irradiation. This dose response was different from that for X-rays which we have reported previously. This may reflect difference in biological effects of heavy ion beams and X-rays.

Increases of liver TBARS and spin clearance at the upper abdomen suggest the possibility of oxidative stress in liver. The early increase of spin clearance may reflect enhancement of the radical reaction in the initial stage of heavy ion damage. Increases of spin clearance prior to damage have been reported with animals which received various oxidative stresses, including liver damage by carbon tetrachloride and ammonia-induced gastric ulcer. In these cases, the increase of spin clearance was reduced by administration of radical scavengers, indicating that the increase of spin clearance resulted from radical reactions in animal bodies. To clarify the meaning of the increase of spin clearance observed in this study, further experiments are necessary.

24. Measurement of Membrane Permeability of a Spin Trap, 5,5-Dimethyl-1-pyrroline-N-oxide (DMPO) by ESR Spectrometry

Kazunori Anzai, Yoshiko Furukawa*, and Toshihiko Ozawa(*Kyoritsu College of Pharmacy)

Keywords: *liposome, DMPO, ESR, spin-trapping, membrane permeability*

Oxygen-derived radicals have been detected by using a spin-trapping technique with ESR spectrometry, mainly in solutions containing subcellular components. With this technique, very short-lived oxygen-derived radicals react with spin traps to yield long-lived radicals. On the other hand, few successful results have been reported using this technique with cellular systems. One reason fot the poor success with cellular systems is that a membrane-permeable spin trap must be used to detect oxygen-derived radicals generated inside the cells. No measurements have been reported on membrane permeability of various spin traps. In the present study, we tried to measure the membrane permeability of the most useful spin trap, 5,5-dimethyl-1-pyrroline-N-oxide (DMPO) with a liposomal system.

Liposomes were made with egg phosphatidylcholine by a reverse-phase evaporation method. Large unilamellar vesicles corresponding to the size of living cells can be prepared by this method. Hydroxyl radicals (*OH) were generated by the reaction of H_2O_2 with Cu complex (Cu(II)en_2) or homolysys of H_2O_2 upon UV-irradiation. The radical adduct between DMPO and *OH (DMPO-OH) was detected with an ESR spectrophotometer (FR-30, JEOL, Tokyo, Japan).

DMPO-OH was prepared and this was mixed with liposomal suspension. The ESR signal derived from outside the liposomes became invisible on using a membrane-impermeable spin-broadening reagent, potassium tris(oxalato) chromate(III). The time course of the ESR signal of DMPO-OH derived from inside the liposomes gave us information on the membrane permeability of DMPO-OH. Even at the first observed point in the time course (at 43 s), we observed a large signal intensity and this intensity slowly decreased. This meant that the permeation of DMPO-OH through the liposomal membrane was rapid and was completed within 43 s.

Next, we tried to measure the membrane permeability of intact DMPO. Liposomes containing Cu(II)en_2 inside were mixed with DMPO and an aliquot of the mixture was mixed with membrane-permeable H_2O_2. The time course of the intensity of the ESR signal derived from DMPO-OH formed inside the liposomes should give us information about the membrane-permeation rate of DMPO. We detected a significant signal intensity at 30 s after the mixing and the intensity remained almost constant during 26 min. We tried a different procedure to measure the DMPO-permeation through the liposomal membrane: *OH was produced by UV irradiation of H_2O_2 in the presence of the liposomes and *OH outside the liposomes was quenched with a high concentration of polyethylene glycol 4000. This experiment also gave the same result that the membrane-permeation rate of DMPO was fast. These results suggested the possibility of detecting radicals generated inside cells by using DMPO.

25. Effect of X-Irradiation on NOS Activity in L1210 Cells

Toyoko Arimoto, Hidehiko Nakagawa, Keizo Takeshita, Hideyuki Majima, Junichi Ueda, Nobuo Ikota and Toshihiko Ozawa

Keywords: *nitric oxide, nitric oxide synthase (NOS), irradiation, α-tocopherol*

Nitric oxide (NO) is an important mediator of cellular communication in several biological systems. NO is formed by nitric oxide synthase (NOS), which requires 02- dependent oxidation of L-arginine to citrulline and NO. An inducible type of NOS (iNOS) is expressed by cytokines, such as tumor necrosis factor-α (TNF-α) and interleukin 1β (IL-1β), as well as lipopolysaccharide (LPS) in many types of cells including macrophages and smooth muscle cells. Overproduction of NO by iNOS in response to inflammatory cytokines has been observed to trigger apoptotic cell death in several types of cells.

This study was conducted to determine the effect of exposure to X-irradiation on NOS activity in L1210 cells. When cells were irradiated with 6 Gy, the level of nitrite in the culture medium increased 48 h after the irradiation. L-mono methyl-L-arginine (L-NMMA), a potent inhibitor of NOS, suppressed the nitrite production, suggesting that iN0S was expressed. The expression of iNOS requires activation of NF- κB, a pleiotropic transcriptional regulatory factor responsive to reactive oxygen species (ROS). Activation of this factor is essential for iNOS gene induction by cytokines and LPS. To examine whether ROS are involved in the accumulation of nitrite after exposure to X-irradiation, the effect of the antioxidant, α- tocopherol (α-Toc), on X-ray-induced nitrite production was examined. Addition of α-Toc to the medium of L1210 cells, no significant effect on nitrite production was observed. The mechanism underlying the effect of exposure to X-irradiation on NOS activity in L1210 cells requires examination.

26. Effect of Nitric Oxide-Releasing Agent upon the Activity of Rat Ovarian P450 Enzyme.

Keiko Suzuki

Keywords: *nitric oxide, P450, ovary*

Nitric oxide is a bioregulator which is involved in various biological phenomena such as vasodilation. It exhibits high affinity to hemoproteins. The effect of nitric oxide upon the activity of ovarian P450 enzyme was examined.

Ovarian homogenates were prepared from eCG(equine chorionic gonadotropin)-treated immature female rats. The supernatant fraction was obtained by the centrifugation at 10,000×g for 20 min. The enzyme preparation was incubated with 3H-labeled 17α-hydroxyprogesterone at 37°C for 60 min to assay the activity of steroid C-17-C-20 lyase. The products were separated by TLC, and the radioactivity of the product, androstenedione, was measured. Three kinds of nitric oxide-releasing agents were investigated for their effect on the enzyme activity. NOC 7, NOC 5 and NOC 12 are known to release nitric oxude at half lifves of 5, 25 and 100 min respectively. When 50 μM of NOC 7, NOC 5 and NOC 12 were included in the assays, the activities of the enzyme were 23, 33 and 90% of the control respectively, whereas they were 92, 87 and 99% of the control at the concentration of 5 μM. NOC 12 was less effective probably becausse of its longer half life, as the incubation time was only 60 min. Thus , it was suggested that nitric oxide may inhibit the activity of P450 enzymes.

27. Dose Rate Effects on Cell Killing by γ-irradiation in Ataxia Telangiectasia Lymphoblastoid Cells

Ikuko Furuno-Fukushi and Kouichi Tatsumi

Keywords: *ataxia telangiectasia, dose rate effect, double-strand break repair*

To investigate the dependency of dose rate effect on ATM gene, loss of the clonogenicity of lymphoblastoid cells derived from a patient with ataxia telangiectasia (AT1-1) was studied after exposure to γ-rays at dose rates of 30 Gy/h, 0.21 Gy/h and 0.0048 Gy/h. AT1-1 cells were very sensitive to killing by high dose rate γ-rays, and showed a comparable sensitivity to those for scid (XRCC7) and LX830 (XRCC4) cells. Survival curves showed an increase in D_0 when AT1-1 cells were irradiated at the lower dose rates as compared to the high dose rate. Split-dose experiments for γ-rays of 30 Gy/h were also carried out in AT1-1 cells. When results for two 0.5 Gy doses, separated by a variable interval, were compared with those of a single dose of 1 Gy, dividing the dose into two fractions was seen to have little effect on cell survival. It was determined that scid and LX830 cells were defective in the repair of DNA double-strand breaks (DSBs) and that the two cell lines failed to show the dose rate effect of γ-rays. Radiation hypersensitivity in AT cells has been believed to result from cell-cycle checkpoint defects, especially since no substantial defect in the capacity to rejoin DNA DSBs has been successfully detected for AT cells following irradiation. Hence, it was suggested that the dose rate effect on cell killing by γ-rays was strongly associated with the efficient repair processes of DNA DSBs.

28. Changes in the Proliferative Activity of Epidermal Melanocytes in Serum-free Primary Culture during the Development of UVB-induced Pigmented Spots in Mice

Tomohisa Hirobe

Keywords: *melanoblast, melanocyte, keratinocyte, UVB, proliferation, differentiation*

Long-term exposure to ultraviolet radiation B (UVB) induced pigmented spots in the dorsal skin of hairless mice. To clarify the cellular mechanism for the development of these UVB-induced pigmented spots, changes were investigated in the proliferative activity of epidermal melanoblats and melanocytes in the dorsal skin at various weeks after UVB irradiations. Epidermal cell suspensions from the dorsal skin of hairless mice were cultured in a serum-free medium supplemented with dibutyryl adenosine 3':5'-cyclic monophosphate (DBcAMP) and basic fibroblast growth factor (bFGF). The suspensions were prepared from the dorsal skins of mice exposed to UVB for 4 weeks (the stage of hyperpigmentation), and from those of mice 3 (the stage of depigmentation), 8 (the stage of appearance of pigmented spots), 20 (the stage of development of small-sized pigmented spots), and 37 (the stage of development of medium-sized pigmented spots) weeks after the cessation of UVB exposures for 8 weeks. At the stage of hyperpigmentation the proliferative activity of melanocytes was suppressed. With the development of pigmented spots, the proliferative activity of undifferentiated melanoblasts gradually increased, and then followed the increase in the proliferative activity of differentiated melanocytes. These results suggest that the proliferative activity of epidermal melanoblasts and melanocytes in UVB-irradiated skin increase with the development of pigmented spots.

29. Establishment and Characterization of Tartrate-resistant Acid Phosphatase (TRAP) Positive Cell Clones from Hamster Bone Marrow: 1. Cartilage Degrading Activity

Hisako Sakiyama, Koichi Nakagawa, Riako Masuda, Kazuko Kuriiwa, Modori Honjo, Yuki Takada and Kazuko Yoshida

Keywords: *TRAP, clone, morphology, cartilage, degradation*

Long bones develop from cartilage, devoid of blood and lymph capillaries, and consisting of amorphous cartilage matrix and chondrocytes. Chondrocytes are programmed to die after differentiating from resting, proliferating, maturing and hypertrophic cells, and the cartilage is replaced by bone marrow from where endochondral ossification starts. The calcified cartilage matrix decreases in parallel with chondrocyte hypertrophic differentiation. Degenerative enzymes such as MMP-9 and complement C1s are secreted during this process. After the programmed cell death of hypertrophic chondrocytes, the remaining sepia of the cartilage matrix is resorbed by cells such as septoclasts. Tartrate-resistant acid phosphatase (TRAP) positive cells which are considered to play a role in the remodeling are often observed at epiphyseal/metaphyseal and metaphyseal/diaphyseal borders. TRAP is used as a marker enzyme for chondroclast/ osteoclast differentiation, the function of which is considered to relate to cartilage/bone resorption. TRAP dephosphorylates bone phosphoproteins, and mice lacking TRAP have been shown to be delayed in cartilage mineralization and defective in osteoclastic bone turnover. However, cartilage resorbing TRAP positive cells (chondroclasts) and bone resorbing TRAP positive cells (osteoclasts) have not been proven to be different cells.

Osteoclast differentiation has been studied by a model system, the coculture of mouse stromal cells and bone marrow cells. Using this system, Chen and Li have immortalized osteoclastogenic cells with SV4OT antigen. Four out of 72-isolated cell lines were induced to generate TRAP positive osteoclast precursor cells when cocultured with stromal cells in the presence of 1^{α}, 25-$(OH)_2D_3$, but none became TRAP positive when cultured alone. From p53-/-mouse bone marrow cells, Miyamoto et al. established a macrophage-like cell line which differentiated to osteoclasts in the presence of stromal sells and l^{α}, 25-$(OH)_2D_3$.

In our laboratory, coculture of hamster bone marrow cells with irradiated hamster chondrocytes and establishment of TRAP positive clones were carriedout. In this system, 1^{α}, 25-$(OH)_2D_3$, a stimulator of TRAP positive cell formation, was not required. Growth characterization and chondrolytic activities of these clones were examined. The isolated clones were designated as CCP-1 through CCP-16. CCP-1, CCP-2, CCP-6 and CCP-7 were mainly used in this study. Morphologically, the clones resembled macrophages, having numerous vacuoles in the cytoplasm, and filopodia and microvilli on the cell surface. The clones fused to form multinuclear giant cells. Their growth was stimulated by chondrocyte-conditioned medium and human M-CSF. The clones were cultured on hamster epiphyseal or human articular cartilage in order to investigate their physiological functions. All tested clones were observed to degrade and invade the cartilage matrix, and also

deposit calcified materials in the matrix. However, electron microscopic examinations showed that the cells did not from a ruffled border or clear zone, both of which are characteristics of osteoclasts.

To date, the clones still remain TRAP positive after four years maintenance in the absence of stromal chondrocytes and 1^{α}, 25-$(OH)_2D_3$.

Publications:

1) Sakiyama, H., Kaji K., Nakagawa, K. and Nagino, K. : Cell Biochem. Func. 16, 159-163, 1998.

2) Inoue, N., Saito, T., Masuda, R., Suzuki, Y., Ohtomi, M. and Sakiyama, H.: Hum. Genet. 103, 415-418, 1998.

3) Nakagawa, K, Sakiyama, H., Tuchida, T., Yamaguchi, K., Toyoguchi, T., Masuda, R. and Moriya, H.: Ann. Rheum. Dis. 58, 175-181, 1999.

4) Suzuki, G., Sawa, H., Kobayashi, Y., Nakagawa, K., Uzawa, A., Sakiyama, H., Kakinuma, H., Iwabuchi, K. and Nagashima, K.: J. Immunol. 162, 5981-5985, 1999.

5) Takada, Y., Sakiyama, H., Kuriiwa, K., Masuda, R., Inoue, N., Nakagawa, K., Itano, N., Saito, T., Yamada, T. and Kimata, K.: Cell Tissue Res., in press.

30. Effect of Heavy Ion Exposure on Cell Cycle Checkpoints

Kiyomi Eguchi-Kasai, Hiromi Itsukaichi, Masahiro Murakami, Tatsuaki Kanai

Keywords: *cell cycle check point, heavy ion beam, cultured cells*

For cancer therapy using heavy ion beams, it is important to know the cell cycle progression for different cell types after irradiation because daily fractionated doses are given to both normal and tumor tissues. We studied the cell cycle progression in cells of normal human fibroblasts (NB1RGB) or rodent cells (V79) after irradiation with carbon ion beams.

Cells were irradiated by carbon ion beams at the Heavy Ion Medical Accelerator in Chiba (HIMAC) and the Cyclotron Facility. Initial accelerated energies of carbon ions were 135 and 290 MeV/nucleon at the HIMAC and 12 MeV/nucleon at the Cyclotron Facility. Linear energy transfer (LET) of the beams at the target was changed by inserting the plastic plate in front of the target. The LET range was 30 - 250 keV/μm at the sample center. The dose rate ranged from about 1 - 5 Gy/m. The reference radiation was 200 kVp X-rays filtered through 0.5 mm Al and 0.5 mm Cu with a dose rate of 0.9 Vy/m. After irradiation, cells were incubated with 5 μM bromodeoxyuridine (BrdU) if needed. Cells were then trypsinized and fixed with 70% ethanol. Cells were stained both with propidiumiodide for the DNA and anti-bromodeoxyuridine-fluorescein, and analyzed with a flowcytometer. Cell cycle distribution was analyzed with the ModiFit LT (Becton Dickinson).

For the asynchronous V79, more than 80% of the cells accumulated in the G2/M phase from 4 to 12 h with a peak at around 6h after irradiation. The maximum value and the width of the peak increased for both LET and radiation dose. Relative biological effectiveness (RBE) of G2 arrest was calculated using the width of the peak at the half values. RBE increased with LET up to 180 keV/μm. RBE values for G2 arrest above 30 keV/μm were bigger than those for the cell inactivation for which the RBE-LET curve had a peak around the LET of about 100 keV/μm. More precise analyses were done using BrdU. Because cells were continuously labeled with BrdU after irradiation, cells at the G1 and the S phases at the time of irradiation incorporated BrdU. Labeled cells showed G2 arrest at 6 to 16 h, depending on LET and dose. In contrast, unlabeled cells showed little G2 arrest. Therefore, the large G2 arrest in V79 cells was due to the populations at the G1 and the S phases. There was no G1 arrest for V79 cells. This is natural because p53 of the V79 cells was mutated. In contrast, there was a big arrest at the G1 phase and a small arrest at the G2/M phase for the NB1RGB cells which have the normal p53.

31. Effect of Estradiol on Radiation-induced Chromosome Aberrations in Human Lymphocytes

Reiko Kanda, Yoko Tominaga, Takeko Odaka and Isamu Hayata

Keywords: *chromosome aberration, estradiol, human lymphocytes*

The scoring of chromosomal aberrations in human lymphocytes provides the most sensitive and reliable method for biological dosimetry of radiation. It has been believed that inter-individual variation in the yield of chromosome aberrations is small among healthy individuals. However, it was recently demonstrated that pregnancy increased radiosensitivity of chromosomes in humans and that the variation of radiation sensitivity in the mothers paralleled that of the pregnancy hormones (Ricoul et al., Mutat. Res, 374, 73-78, 1997). In the present study, we examined the effect of estradiol (E2) on the yield of radiation-induced chromosome aberrations in cultured lymphocytes.

Lymphocytes were cultured for 3 days in the medium containing E2 at 0-100000 ng/ml. On the second day, they were irradiated by X-rays at 3Gy, and then 2 % phytohemagglutinin and 0.05 mg/ml colcemid were added to the medium. After further 48 hours, mitotic indices and the yields of chromosome aberrations were examined.

E2 treatment at concentrations above 1000 ng/ml resulted in dose-related inhibition of mitosis. The frequencies of dicentrics plus centric rings induced by the 3 Gy-irradiation in the cultures with 100 ng/ml of E2 seemed to be higher than those in the cultures without E2. On the other hand, the aberration yields slightly decreased due to the treatment with E2 at the concentration of 1ng/ml. These tendencies were exhibited both in the purified lymphocyte culture and in the whole blood culture, although they were more significant in the latter. Difference in the aberration frequencies at 3 dose points, i.e., 0, 1 and 100 ng/ml, was statistically analyzed using the results of 5 whole blood cultures (Table 3). The frequency of dicentrics plus centric rings in the cultures containing 100 ng/ml E2 was significantly ($p<0.05$) higher than that with 0 ng/ml. The frequency of excess fragments was not affected by E2 concentration. The frequency of total breaks was also significantly ($p<0.05$) higher in the whole blood cultures with 100 ng/ml E2 than in those with 1 ng/ml. No dicentrics or centric rings were observed in non-irradiated lymphocytes cultured with 100 ng/ml of E2.

The level of estrogens in the plasma of a woman during the last month of pregnancy is around 100 ng/ml. Therefore, this study may provide direct evidence in humans that radiosensitivities vary in relation to physiological conditions. In the present study, the 20% increase in the number of dicentrics plus centric rings was seen in the lymphocytes treated with 100 ng/ml E2 following irradiation. Their slight, but significant increases, have been reported in the irradiated lymphocytes of hereditary retinoblastoma and Alzheimer's disease patients; their mean values being greater by factors of 1.19 and 1.25, respectively, compared to normal controls. When the radiosensitivity is even slightly accelerated for a long term, it could lead to the increased incidence of some diseases caused by chromosome rearrangements. Furthermore, in view of human populations, a 20 % increase in radiosensitivity may not be acceptable, although it is small for each individual.

Table 3. The effect of estradiol concentration on the frequency of chromosome aberrations (Mean ± SEM, n=5) in human lymphocytes irradiated at 3 Gy.

Estradiol concentration (ng/ml)	0	1	100
Dicentrics plus centric rings per cell	1.00±0.02	0.93±0.05	1.21±0.10a
Excess fragments per cell	0.58±0.05	0.56±0.08	0.60±0.08
Total breaks per cell	2.83±0.05	2.65±0.09	3.39±0.29b

[a, b] Significantly ($p < 0.05$) different from the values of the 0 and 1 ng/ml estradiol by Wilcoxon signed-ranks test, respectively.

Publications:

Kanda R. and Hayata I.: J. Radiat. Res., 40, 95-100, 1999.

32. Effect of Curcumin on the Production of Nitric Oxide by Cultured Rat Mammary Gland

Makoto Onoda and Hiroshi Inano

Keywords: *nitric oxide, nitric oxide synthase, mammary gland, curcumin*

Nitric oxide (NO) is a unique biological messenger molecule that is synthesized from L-arginine by nitric oxide synthase (NOS). NO regulates blood pressure, smooth muscle relaxation, neuronal signaling, immune reactions, and aspects of development, cell motility and differentiation. NOS has at least three distinct isoforms, including the neuronal/brain (nNOS, bNOS or NOS1), inducible (iNOS or NOS2), and endothelial (eNOS or NOS3) types, and these are known to distribute across a wide spectrum of cell types and tissues. In our previous report we showed that three isoforms of NOS are present in the rat mammary gland, and we suggested that these NOS isoforms may correlate with mammary gland development and regulatory functions. Meanwhile, curcumin, the yellow pigment and a major component of turmeric which is a commonly used spice, has been shown to possess anti-carcinogenic and anti-inflammatory activities and inhibitory activity towards reactive oxygen-generating enzymes. We reported that curcumin had a preventive activity towards the promotion of radiation-induced mammary tumorigenesis based on results from an animal model system established in our laboratory. Now, we have examined the effect of curcumin on NO-generation by the rat mammary gland in culture to elucidate the effectiveness and usefulness of curcumin in the pathophysiology of the mammary gland.

Isolated mammary glands from female Wistar-MS rats were diced into approximately 3-mm cubes and each cube was cultured in the well of a 24-multiwell plate containing 2 ml of 5% fetal calf serum/Dulbecco's Modified Eagle Medium in the presence or absence of bacterial lipopolysaccharide (LPS, 0.5 μg/ml) for 2 days in a mixture of 5% CO_2/95% air at 37°C. Curcumin (~100 μM) was added at the same time to the LPS treated cultures. The nitrite concentrations in conditioned media were determined immediately after the termination of the culture with Griess reagent mixture. Tissue homogenates from the incubated mammary glands were also prepared for Western blot analyses of NOS isoforms. NO scavenging activity of curcumin was examined by incubation with NO donor, N-ethyl-2-(1-ethyl-2-hydroxy-2-nitrosohydrazino)-ethanamine (NOC 12) in a reaction mixture held at 37°C for 2 h. At the end of incubation, the reaction mixture was placed on ice and collected for determination of the nitrite concentration.

The amount of NO produced spontaneously by mammary glands in culture was relatively minute for the 2-day culture period, whereas the NO concentration in the conditioned media was significantly increased (almost 20-fold over the control) by the addition of LPS to the culture system. This enhancement of NO production by the mammary gland with LPS was reduced to 76% and to 59% by addition of 30 μM and 100 μM curcumin, respectively, to the culture (Fig. 14.). The iNOS (122 kDa) and eNOS (152 kDa) isoforms were detected in the mammary gland extracts at the terminus of the organ culture. The quantity of immunoreactive iNOS was apparently increased in the extract treated with LPS, while, the eNOS expression

was clearly diminished in the corresponding tissue extract. Curcumin (100 μM) obviously suppressed the iNOS expression in the mammary glands cultured with LPS, and recovery of the decline in eNOS expression was conversely observed. Incubation of NOC 12 resulted in linear dose-dependent NO production, and the presence of curcumin reduced the NO concentration in the mixture (Fig. 15.). These results indicate that curcumin has an inhibitory activity for iNOS induction by LPS in the mammary gland and a scavenging activity for NO radical, and they suggest that the therapeutic properties of curcumin regarding inflammation, cancer and other pathological conditions of mammary glands might be explained, at least partly, by its ability to inhibit iNOS expression and to scavenge NO.

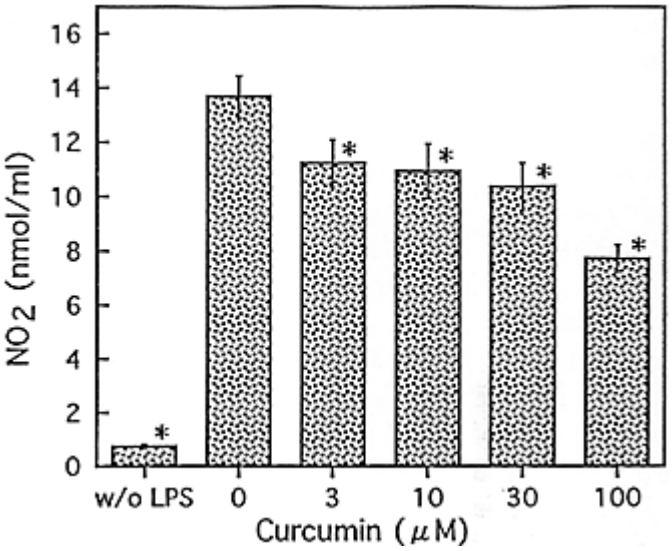

Fig.14. Inhibition of NO production in LPS-stimulated mammary glands by curcumin.
A piece of the mammary gland was cultured, and at the end of culture the conditioned media were collected for the detection of nitrite (NO_2) concentration.
*: Significant difference from LPS alone control, $p < 0.001$.

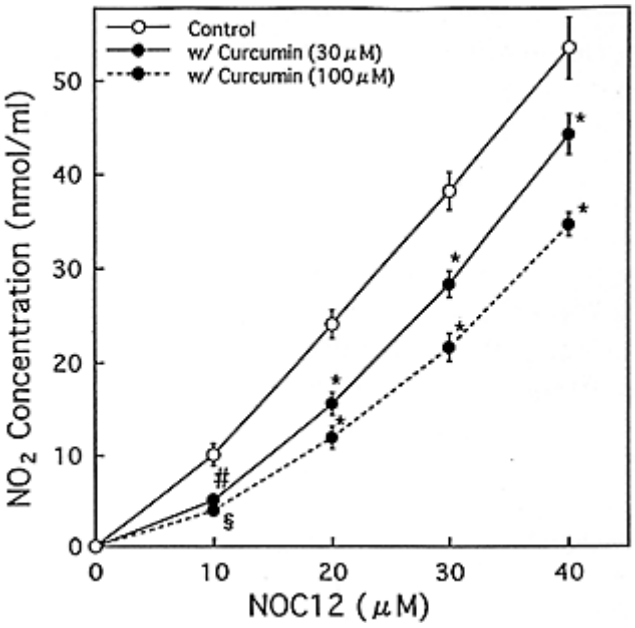

Fig.15. Production of nitric oxide from NOC 12 and NO scavenging by curcumin.

NOC 12 in PBS was mixed with curcumin dissolved in alcohol and incubated at 37°C for 2 h. The nitrite (NO_2) concentration was determined with Griess reagent mixture. Values represent mean ± SE obtained from two independent experiments. Each experiment contained two tubes per replicate.

* : Significant difference from control (NOC 12 alone), $p < 0.001$.

§ : Significant difference from control (NOC 12 alone), $p < 0.01$.

: Significant difference from control (NOC 12 alone), $p < 0.05$.

33. Evidence for mRNA Expression of Vascular Endothelial Growth Factor by X-ray Irradiation in a Lung Squamous Carcinoma Cell Line

Koichi.Ando, Soichiro Ando, Kumie Nojima, Hideyuki Majima, Hiroshi Ishihara, Masao Suzuki, Yoshiya Furusawa, Sachiko Koike, Hiroshi Yamaguchi and Masatake Yamauchi

Keywords: *VEGF, cytokine, inhibitor, Src tyrosine kinase, protein kinase C*

Vascular endothelial growth factor (VEGF) is a multipotent cytokine which plays an important role in various angiogenic conditions as well as in some tumor behaviors. Here we examined the induction of VEGF mRNA by X-ray irradiation in a lung squamous cell carcinoma cell line (RERF-LC-AI). Irradiating the cells with 15 Gy X-rays significantly increased the mRNA expression up to 2.5-fold more than the control at a post-irradiation time of 16-24 h. The induction of VEGF mRNA by X-rays irradiation was completely blocked by treating cells with either genestein (Src tyrosine kinase inhibitor) or H7 (protein kinase C inhibitor). This suggests that the mechanism of induction might be concerned with the pathway which triggers Src tyrosine kinase of the cell surface and the protein kinase C pathway.

Publications:

Ando S., Nojima K., Majima H., Ishihara H., Suzuki M., Furusawa Y., Yamaguchi H., Koike S., Ando K., Yamauchi M. and Kuriyama T. : Cancer Letters 132, 75-80, 1998

34. Studies Of Cellular And Molecular Mechanisms Of High LET Irradiations

Hideyuki Majima, Masao Suzuki, Kumie Nojima, Shizuko Kakinuma and Kazunobu Fujitaka

Keywords: *MnSOD, promoter, DMSO, protection, PCC, mutation, LET, RBE*

1) MnSOD promoter mutations cause gene disfunction

Manganese superoxide dismutase (MnSOD) has been shown to play an important role in preventing the development of cancer. MnSOD activity is reduced in many transformed cells and tumor tissues. We previously showed that the reduced level of MnSOD activity in cancer cells was not due to a defect in the primary structure of MnSOD protein, but rather was due to defects in gene expression. To elucidate the cause for the reduced expression of human MnSOD in cancer, we investigated the nucleoside sequence in the regulatory region of the MnSOD gene in a normal human cell line and various human tumor cell lines. A DNA sequence analysis identified three heterozygous mutations in the proximal region of the promoter in five human tumor cell lines. These mutations, clustered around the G C-rich region of the human MnSOD promoter, change the binding pattern of AP-2 and lead to a reduction in transcription activity using a luciferase reporter assay system. These results suggest that the reduced level of MnSOD expression in some tumor cells is, at least in part, due to a defect in the DNA sequence of the promoter region.

2) Effects of heavy particle irradiation on frozen mammalian cells.

We examined the effect of DMSO on sensitivity to carbon ions in this study. We tested cell growth and colony forming ability of cells that were kept frozen in new made Teflon dishes. We examined the effect of 10 % DMSO on colony ability after radiation by carbon ions of L5178Y and M10 cells. DMSO protected colonizing ability of two cell types.

3)LET dependence for cell death, mutation induction and chromatin damage when irradiated with different kinds of ion beams

We have been studying the LET dependence for cell death, mutation induction and chromatin damage in human cell lines irradiated with different kinds of ion beams. The effect of cell death was detected by colony forming assay. The mutation induction for hprt locus was investigated to measure the 6-TG resistant colony forming ability. The induction of residual chromatin breaks was measured by counting the number of remaining chromatin fragments after a 24-hour post-irradiation incubation, using the premature chromosome condensation (PCC) technique. The results for cell death showed that the RBE values, relative to 200kV X-rays, using 290MeV/n carbon ion beams were 1.44 for 20keV/μm, 1.71 for 40keV/μm, 2.14 for 60keV/μm, 2.69 for 90keV/μm, 2.48 for 101keV/μm, 2.81 for 124keV/μm and 1.11 for 217keV/μm. The induction for mutant clones and residual chromatin breaks depended on LET values; RBE values increased with increasing beam LET values, when using 290MeV/n carbon ion beams (13, 40, 77 101keV/μm). Both mutation induction and residual chromatin- breaks by carbon ion beams were 1.32 to 8.30 times higher than those by 200 kV X-rays.

Publications:

Majima H., Oberley T., Furukawa K., Mattson M., Yen H-C., Szweda L. and St.Clair D.:J.Biol.Chem., 273, 8217-8224, 1998.

35. $p21^{WAF1}$ Expression by Activator of Protein Kinase C is Regulated Mainly at Post-transcriptional Level in Cells Lacking p53: Important Role of RNA Stabilization

Makoto Akashi, Misao Hachiya, Sakae Tanosaki and Yoshiko Kawase

Keywords: *$p21^{WAF1}$, p53, protein kinase C, mitogen-activated protein kinase*

$p21^{WAF1}$ inhibits cyclin/cycline-dependent kinase (Cdk) complexes, causing cell cycle arrest. $p21^{WAF1}$ contains p53-binding sites in its promoter; and expression of $p21^{WAF1}$ is inducedfibroblasts WI38 with PMA also induced the accumulation of $p21^{WAF1}$ without affecting p53 levels. However, PMA did not increase levels of $p21^{WAF1}$ mRNA in cells with either their PKC or mitogen-activated protein kinase (MAPK) pathway blocked. Furthermore, treatment of cells with various derivatives of phorbol esters which activate PKC resulted in the induction of $p21^{WAF1}$ in SKOV-3 cells. In contrast, phorbol esters, which are unable to activate PKC, failed to induce $p21^{WAF1}$ expression. PMA increased the transcriptional rate of $p21^{WAF1}$ and activated the transcription of a luciferase reporter gene controlled by the p21 promoter with or without a p53 consensus binding sequence placed in the SKOV-3 cells. On the other hand, PMA markedly stabilized $p21^{WAF1}$ mRNA; the half-life (t1/2) of $p21^{WAF1}$ in PMA-treated cells was more than 8 hours as compared to less than 1 hour in untreated cells. These findings provide evidence that the PKC pathway induces expression of $p21^{WAF1}$ independent of p53. Our present study also suggests that the accumulation of $p21^{WAF1}$ transcripts by PMA occurs mainly at the post-transcriptional level.

Publications:

Akashi M, Osawa Y, Koeffler HP, Hachiya M.: Biochem. J., 337, 607-616, 1999.

36. Effects of Fractionated Total Body Irradiation on Megakaryocyte Progenitor Cells(CFU-Meg) and Granulocyte-Macrophage Progenitor Cells(CFU-G) in Mice

Kaoru Tanaka and Eiichi Kojima

Keywords: *fractionated total body irradiation, CFU-Meg, CFU-GM, mice*

Hematopoietic systems are the most sensitive to radiation in the body, but effects of fractionated irradiation on hematopoietic systems have not been well established. We previously reported the effects of two equal fractionation doses (3.12Gy×2) upon mouse survival and peripheral blood cell number. The mouse survival increased on increasing intervals up to 5h, at which 90% of the mice survived. With a longer interval, the survival decreased once until about 11h and then increased again. On the other hand, 99% of the mice died around 15 days after the single irradiation of 6.24Gy. From this result, we concluded that the mice died due to bone marrow death. In the present study, we investigated the effects of two equally split doses with 5h intervals on hematopoietic progenitor cells, megakaryocyte progenitor cells (CFU-Meg) and granulocyte-macrophage progenitor cells (CFU-GM), in mice. Spleen weights was also investigated because spleen is one hematopoietic organ.

Female BALB/c mice, 10-14 weeks old, were used. The mice were exposed to total body irradiation with X-rays (200kVp, 20mA, 0.7Gy/min) delivered as a single dose or two equally split doses (0.24-3.12Gy×2) with 5h intervals. After the second irradiation, they were sacrificed, and the femur and spleen were removed. Then femoral bone marrow and spleen cells were cultured.

CFU-Meg were studied by using a fibrin clot culture system for 5h intervals. After 4 days of plating, colonies of 4 or more acetylcholinesterase-positive cells were scored as CFU-Meg. There was a recovery in the survival of femoral CFU-Meg after the fractionated doses of irradiation. A smaller recovery was observed for splenic CFU-Meg than for femoral CFU-Meg. CFU-GM cultures were performed in semisolid medium containing alpha modification of Eagle's medium, WEHI-3b cell line-conditioned medium as a source of colony-stimulating factor, and 0.8% wt/vol methylcellulose. Seven days later, colonies consisting of 50 or more cells were scored as CFU-GM. As shown in Fig.16, there was a recovery in the survival of femoral CFU-GM after the fractionated doses. At high dose (6.24Gy), the difference of femoral CFU-GM survival between single and fractionated irradiations was larger than that at low doses. A small recovery was also observed for splenic CFU-GM at low doses (0.47-2.84Gy) and a large recovery was observed at the high dose.

The spleens of mice were weighed for 30 days after irradiation. Spleen weights decreased similarly in both single and split doses (3.12Gy□~2) of irradiation until 13 days. Weights of split dose groups began to show an increase on 15 days, and then extended beyond a normal level until 20 days. By contrast, single dose groups did not show any increase.

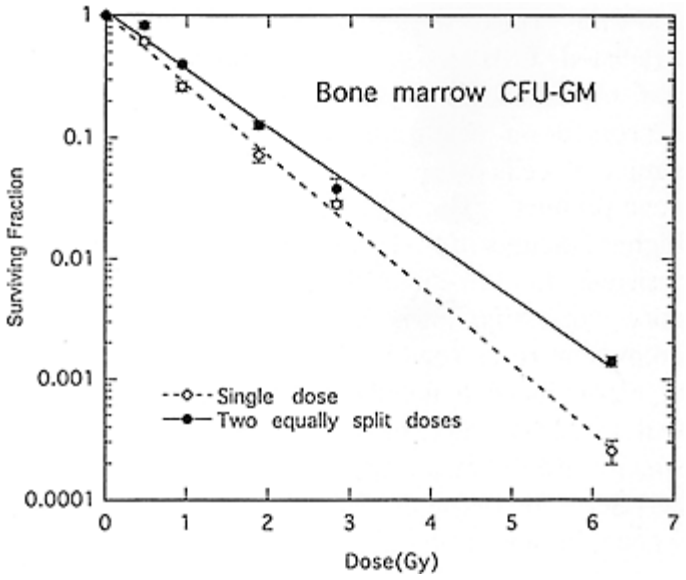

Fig.16. Dose response curves for bone marrow CFU-GM exposed to single or two equally split doses of X-rays.

37. Protection of Retrovirus-induced Disease by Transplantation of Bone Marrow Cells Transduced with MuLV Env Gene via Retrovirus Vector

Shiro Aizawa, Hitoko Kamisaku and Masanobu Kitagawa*

(*Tokyo Medical and Dental Univ.)

Keywords: *gene therapy, bone marrow transplantation, Fv-4, virus resistance, retrovirus vector*

Fv-4 is a mouse gene that dominantly confers resistance to infection by ecotropic murine leukemia virus (MuLV). We have demonstrated previously that bone marrow chimeras in which hematopoietic cells were replaced with cells expressing Fv-4 resistant (Fv-4^r) gene product became refractory to Friend leukemia virus (FLV)-induced leukemogenesis. To induce in vivo resistance against retrovirus-induced diseases by retroviral vector-mediated gene transducton, we introduced Fv-4^r env gene into bone marrow cells of FLV-susceptible C3H/He (C3H) mice with retroviral vector (pLSF) derived from murine Friend spleen focus forming virus (SFFV) and the cells were transplanted into lethally irradiated C3H mice. After the bone marrow transplantation, Fv-4^r gene product was succesfully expressed on erythroid and myeloid cells, while lymphoid cells were only weakly expressing Fv-4^r gene product. The C3H mice expressing relatively higher amounts of Fv-4^r gene product were rendered resistant to FLV-induced erythroleukemia, while mice expressing lower amounts of the Fv-4^r gene product were still susceptible. Effective protection of FLV-induced leukemia in these mice suggested that the Fv-4^r gene expression by erythroid cells which were the major target for FLV infection might be critical for resisting FLV-induced leukemia. Thus, a gene therapy model by transducing Fv-4^r env gene using bone marrow transplantation would provide a useful protection model system of retrovirus-induced diseases.

Publications:

Kitagawa, M., Aizawa, S., Kamisaku, M., Hirokawa, K. and Ikeda, H.: Exp. Hematol. 27, 234-241, 1999.

38. Immunochemical Localization of Novel Nuclear Protein NP95 in Testis

Masahiro Muto, Yasuyoshi Kanari, Eiko Kubo, Kouichi Tatsumi, Takatoshi Uemura* and Toshimichi Ikemura*

(*Dept. Evolutionary Genetics, National Institute of Genetics, Mishima, Japan)

Keywords: *nuclear protein NP95, PCNA, DNA replication, cell cycle, spermatogenesis*

NP95 (nuclear protein, 95 kDa) is expressed during S phase progression but is suppressed during G1 and G2/M phases in normal mouse thymocytes. Cloning and sequencing revealed that NP95 is a novel nuclear protein of 782 amino acids and contains a leucine zipper motif, a zinc finger motif, a putative cyclin A/E-CDK2 phosphorylation site, and RB-binding motifs. We also found abundant expression of Np95 mRNA in the testis. In this organ, the unique organization of the seminiferous epithelium allows precise determination of the temporal expression of specific genes during spermatogenesis. Spermatogenesis has been divided into three phases based on functional considerations: (a) the proliferative phase (spermatogonia) in which cells undergo rapid successive divisions; (b) the meiotic phase (spermatocytes) in which genetic material is recombined and segregated; and (c) the spermiogenic phase (spermatids) in which haploid spermatids differentiate into elongated ones. We studied localization of NP95 in testis sections. Immunostaining using anti-NP95 antibody revealed that NP95 was expressed in almost all cells except those of the lumenal surface of the epithelium, where elongated spermatids exist. When anti-PCNA antibody was used, the stained regions were restricted to the proliferating spermatogonial layers. To study the spatial and temporal localizations of NP95 in meiotic nuclei, we isolated spermatogenic cells and carried out double immunostaining of NP95 and RAD51 which were detected as discrete foci along the synaptonemal complex in early prophase I. The results indicated that RAD51 was detected as foci in spermatocytes, but little staining was observed in round spermatids. In contrast, NP95 was detected as discrete foci in the nuclei of both spermatocytes and round spermatids; co-localization with RAD51 was very rare. Results of the immunohistochemical analysis in testis were consistent with the expression pattern of NP95 that was observed from spermatogonia to round spermatids. RAD51 is involved in recombination and is associated with synaptonemal complex formation in meiotic prophase cells. Since NP95 was not colocalized with RAD51 in meiotic prophase cells, NP95 may not be associated with the synaptonemal complex or involved directly in the recombination process itself. The finding that NP95 was expressed in spermatids where replication does not occur is consistent with the prediction that NP95 might play some role in the mismatch-repair mechanism. As a consequence of homologous recombination and heteroduplex formation, a small amount of DNA is synthesized through mismatch DNA repair. We propose that NP95 is involved in both mitotic and meiotic progression, presumably in a post-replication fashion and is a novel cell-cycle regulator that is associated with DNA fidelity maintenance.

Publications:

1) Fujimori, A., Matsuda, Y., Takemoto, Y., Hashimoto, Y., Kubo, E., Araki, R., Fukumura, R., Mita, K., and Muto, M. : Mammalian Genome , 9, 1032-1035, 1998.

2) Kawai, H., Kitamura, Y., Nikaido, O., Tatsuka, M., Hama-Inaba, H., Muto, M., Ohyama, H. and Suzuki, F. Radiat. Res. 149, 41-51, 1998.

3) Hama-Inaba, H., Wang, B., Mori, M., Matsushima, T., Saitoh, T., Takusagawa, M., Yamada, T., Muto, M., and Ohyama, H. Mutation Research , 403, 85-94, 1998.

39. Calorie Restriction and Spontaneous Hepatic Tumors in C3H/He Mice

Kazuko Yoshida, Tohru Inoue[*] and Yoko Hirabayashi[*]

([*]Cellular and Molecular Toxicology Division National Institute of Health Sciences.)

Keywords: *caloric restriction, hepatic tumors, initiation, promotion*

The extension of life span seen in calorie-restricted rodents is assumed to be mainly due to the reduced incidence of tumors. However, the mechanism underlying this reduced incidence of tumorigenesis is not clearly understood. It is known that some experimental mice, not only the hepatoma-susceptible strain, C3H/He, but also hepatoma-resistant ones, such as C57BL/6, carry a spontaneous Ha-ras mutation; therefore, tumor-promoting factors, including possible "hepatocarcinogen sensitivity gene(s)" other than the Ha-ras mutation, may be important factors in modulating and promoting the development of hepatic tumors. Also, the Ha-ras mutation per se seems to be an important factor defining susceptibility to spontaneous tumorigenesis. Whether caloric restriction modulates the initiation process or the promotion process, or both, during experimental carcinogenesis, is of much interest. We can possibly define this by choosing different modes of caloric restriction; i.e., restriction designed to start before treatment with carcinogen(s) to modulate an initiation process, or restriction starting after treatment to modulate the promotion process. Thus, by irradiating experimental mice before and after caloric restriction, we clearly showed in our previous study that the reduction in radiation leukemogenesis was due not only to changes in an initiating process but also in the promotion process, respectively.

In the present study, we analyzed changes in the incidence of hepatoma and other non-neoplastic lesions in C3H/He mice starting food restriction at two different stages, i.e., at the young adult stage (YA), and at the full-adult stage (FA), specifically focusing on whether there was a delay in onset time, a reduction in the frequency of total spontaneous hepatomata, and consequently, differences in the rate of occurrence of tumors between the two regimes. Also, for small-sized hepatomas, which tend to appear in the later stages of a lifetime carcinogenic study, we focused on possible differences in these same parameters that might be caused by caloric restriction.

Caloric restriction lengthened the life spans of both groups, the YA, and FA. Both groups showed striking reductions of spontaneous hepatomas, from 70.9±3.5% for non-restricted controls down to 35.7±5.7 and 30.4±4.0%, for mice restricted from YA, and from FA stages, respectively; further, the numbers of tumor-free mice in the restricted groups increased by 45.7% and 38.5%, respectively, from 11.5%, in the non-restricted control. The cumulative incidences of hepatoma in the caloric restricted groups showed a delayed and lower incidence compared with those of the non-restricted group; a parallel delay might result from weakened activity in tumor promotion, whereas a lower frequency might reflect a possible reduction of target cells for hepatomata development. Both effects could be assumed to have resulted from caloric restriction. When cumulative incidences of small hepatomas were compared between the two restricted groups, restriction started at the YA stage was assumed to have caused fewer initiation stresses, as well as to have delayed promotion, as clearly evidenced by a flatter curve of incidence with a lower total incidence. Thus, the time at which caloric restriction was started played a critical role in its subsequent effects.

Publications:

Yoshida K., Inoue T., Hirabayashi Y., Nojima K. and Sado T. : The J. Nutri. Health & Aging, 3, 121-126, 1999.

40. Immunohistochemical Changes of the Blood-brain Barrier in Rat Spinal Cord after Heavy Ion Irradiation

Shinobu Okada[*], Riki Okeda[*], Satoru Matsushita and Akihiro Kawano

([*]Tokyo Medical and Dental University)

Keywords: *endothelial barrier antigen, heavy ion, spinal cord, rats*

Changes in the blood-brain barrier (BBB) of the rat spinal cord after irradiation with heavy ions were investigated ultrastructurally and immunohistochemically by using SMI 71, a monoclonal antibody against rat endothelial barrier antigen (EBA), anti-ZO-1, a polyclonal antibody against endothelial tight junctions, anti-rat serum to extravasated serum, and anti-vascular endothelial growth factor (VEGF). The lower thoracic and lumbar cord of male Wistar rats was singly irradiated with a carbon beam at a dose of 30 Gy. Rats were sacrificed before or after the onset of hind limb paralysis. Histologically, white-matter vacuolization was observed from 13 weeks after irradiation, and white-matter necrosis was first noted at 17 weeks. SMI 71 staining decreased or disappeared 13 weeks after irradiation, just prior to the formation of white-matter necrosis, and was almost completely lost in the center and periphery of the white-matter necrosis. Although ZO-1 expression and tight junctions in the ultrastructure were preserved at the time, serum leakage occurred almost completely in parallel with the changes in EBA. Therefore, carbon ion irradiation at a dose of 30 Gy induces BBB breakdown 13 weeks after irradiation. The SMI 71-negative blood vessels were sparsely distributed throughout the entire white and gray matter, and there was no evidence of preferential localization. Immunostaining of smooth muscle actin showed that most of the SMI 71-negative blood vessels were veins or capillaries. These findings suggest that the hyper-permeability of the veins and/or capillaries that occurs after a certain latent period is one of the important factors in the pathogenesis of delayed radiation injury by carbon ions, the same as by X-rays. Radiation-induced functional disturbances of the endothelium and involvement of cytokines such as VEGF are suspected of being the cause of such vascular hyper-permeability.

Publications:

1) Okada, S., Okeda, R., Matsushita, S. and Kawano, A.: Radiat.Res., 150, 304-315, 1998.

2) Okada, S., Okeda, R., Matsushita, S. and Kawano, A.: Neuropathology, 18, 188-198, 1998.

41. Relationship between HL91 Uptake and Blood Flow in Tumor

Tsunehiko Nishimura[1], Mitsuaki Tatsumi[1], Kenji Yutani[1], Takayuki Nakano[1], Osamu Inoue[2], Kyosan Yoshikawa[3]

([1] Tracer Kinetics, Osaka University Graduate School of Medicine, [2] Medical Physics, School of Allied Health Sciences, Osaka University Faculty of Medicine, [3] National Institute of Radiological Sciences)

Keywords: *Tumor hypoxia, HL91, IAP, GLUT1, DG*

Technetium-99m-HL91 (HL91) is a potential agent for imaging hypoxic tissue in vivo. Last year we reported that the HL91 uptake, the C-14-deoxyglucose (DG) uptake, and the expression of glucose transporter type 1 (GLUT1) in the hxpoxic area significantly higher than those in the normoxic area. This year, to elucidate the relationship between hypoxia and blood flow in a tumor, dual-tracer autoradiography with HL91 and C-14-iodoantipyrine, a blood flow tracer, (IAP) was performed in a tumor [Walker 256 (rat mammary carcinoma) cell] bearing rat model. The distribution of each tracer was analyzed visually and semi-quantitatively. In the tumors with central necrotic areas, HL91 uptake was marked around the necrotic areas. IAP uptake was marked at the periphery of the tumors, around the areas of marked HL91 uptake. Normalized HL91 uptake (%HL91) was highest in the low-normalized IAP uptake (%IAP) fraction in the non-necrotic areas. There was a weak negative correlation between %HL91 and %IAP in the non-necrotic areas ($r = -0.322$, $p < 0.0001$). In tumors with few or no necrotic areas, HL91 uptake was observed heterogeneously throughout the tumors, while IAP uptake was predominant at the periphery of the tumors. %HL91 was higher in the inner two-thirds of the tumor than in the outer third. There was also a weak negative correlation between %HL91 and %IAP ($r = -0.354$, $p < 0.0001$). This study confirmed that high HL91 uptake is related to low blood flow. The marked HL91 uptake around the necrotic region suggests the presence of chronic hypoxia in a tumor.

Publications:

M. Tatsumi et al. Eur. J. Nucl. Med. (1999) 26:91-94

42. Ras Gene Mutation in Spontaneous and Gamma-ray-induced Thymic Lymphomas of Scid Mice

Mayumi Nishimura, Shigeharu Wakana, Shizuko Kakinuma, Kazuhide Mita, Hiroko Ishii, Shigeru Kobayashi, Toshiaki Ogiu, Toshihiko Sado and Yoshiya Shimada

Keywords: *thymic lymphoma, Scid mice, gamma-rays, ras gene mutation*

Radiation carcinogenesis is a process in which cells acquire malignancy through cumulative genetic or epigenetic alterations. Characterization of genetic alterations in proto-oncogenes and tumor suppressor genes of spontaneous and radiation induced tumors of experimental animals will aid in further understanding the special gene change(s) underlying tumor development. From the viewpoint of radiation biology, severe combined immunodeficient (Scid) mice are unique in that they have a defect in rejoining of DNA double-strand breaks and thus exhibit not only complete absence of functional T and B cells, but also hypersensitivity to ionizing radiation. It has recently been found that scid mice are highly susceptible to radiation-induced lymphomagenesis. The purpose of the present study was to investigate the contribution of ras gene activation in radiation-induced thymic lymphomas in scid mice and to examine the mutation spectra of ras genes in these tumors.

The incidence of thymic lymphomas increased as a function of the dose after single exposures to gamma-rays at doses of 0.25 to 3 Gy. About 80% of the mice developed thymic lymphomas after the exposure to more than 1 Gy, whereas 40 out of 204 non-irradiated control mice (19.6%) developed thymic lymphomas within one year after exposure. Then both the frequency and the spectrum of Kras and Nras mutations in spontaneous and radiation-induced lymphomas were examined. As shown in Table 4, neither mutated Kras nor Nras genes were detected in spontaneous lymphomas, while Kras mutations increased in a dose-dependent manner in radiation-induced lymphomas. However, Kras mutations were rather infrequent and no mutations were detected in Nras genes, suggesting ras mutation was not significantly involved in the development of thymic lymphomas in scid mice. Analysis of the spectrum of Kras mutations demonstrated unique mutations in both codons 13 (GGC to GAC) and 61 (CAA to CTA) in addition to the commonly identified substitution of GAT for GGT in the codon 12 of Kras, whereas the activating mutation for the Kras gene was a G to A transition in codons 12 and 13 and an A to T transversion in codon 61.

Table 4. Ras gene point mutations.

Dose (Gy)	Lymphoma frequency	Number of tumors with mutation/ number of tumors examined	Kras		Nras	
			Exon 1	Exon 2	Exon 1	Exon 2
0	40/204 (21%)	0/15 (0%)	nd	nd	nd	nd
0.25	32/104 (31%)	0/10 (0%)	nd	nd	nd	nd
1.0	72/106 (68%)	1/18 (6%)	nd	^{61}CAA → CTA	nd	nd
2.0	94/104 (86%)	2/16 (13%)	^{12}GGT → GAT ^{13}GGC → GAC	nd	nd	nd
3.0	78/204 (75%)	3/18 (17%)	^{12}GGT → GAT ^{12}GGT → GAT ^{12}GGT → GAT	nd	nd	nd

nd: Not detected

Publications:

Nishimura, M., Wakana, S., Kakinuma, S., Mita, K., Ishii, H., Kobayashi, S., Ogiu, T., Sado, T. and Shimada, Y.: Radiat. Res., 151, 142-149, 1999.

43. Effects of Clinostat-microgravity and Heavy Particle Radiation on Bone and Calcium Metabolism in Rats

Satoshi Fukuda and Haruzo Iida

Keywords: *clinostat-microgravity, heavy particle beam, bone histomorphometry, bone mineral density, rats*

We have previously developed a clinostat-microgravity rat model as a new ground-based model for clarifying the changes that occur in systemic bone and calcium metabolism in the space environment. The aims of the present study were to examine the effects of (1) a 2-week period of clinostat-microgravity, which is the average period of a space flight, so that the results could be compared with those of previous reports; (2) exposure to heavy particle radiation, a component of cosmic rays; and (3) the combination of clinostat-microgravity and radiation on bone and calcium metabolism in rats. Bone mineral density, histomorphometric values, the breaking force of bone, intestinal calcium absorption, urinary calcium excretion, calcium regulating hormones (PTH and BGP), and weights of adrenal gland and skeletal muscles were measured. The clinostat-microgravity model produced a low bone turnover with decreases in bone formation and resorption, trabecular BMD, intestinal calcium absorption, and BGP concentration, and increase in PTH concentration, but other data remained unchanged or actually increased. Exposure to heavy particle radiation inhibited bone metabolism, e.g. lack of bone labels, with doses of 1.25-5.0 Gy as well as changes in the bones, intestinal calcium absorption, urinary calcium excretion, PTH and BGP concentrations. With a combination of both clinostat-microgravity and radiation, such changes tended to be more pronounced, and noticeable findings were seen as the bone labels in the groups irradiated with 1.25 and 2.5 Gy, but no bone label in the group irradiated with 5.0 Gy. Based on the gathered data, the utility of the clinostat-mirogravity model, the effects of the short-term experiment, the exposure to radiation, and the combination of clinostat-microgravity and radiation can be discussed.

Publications:

Fukuda S. and Iida H.: J. Jpn. Soc. Bone Morphom, 9, 35-44, 1999.

44. Functional Complementation of the Radiation Sensitive Mutant M10 Cell Line by Human XRCC4 cDNA Expression

Masahiko Mori, Hiromi Itsukaichi and Koki Sato*(*Kinki Univ.)

Keywords: *DNA -double strand break repair, XRCC genes*

Nine complementation groups have been reported for Chinese hamster and mouse cell mutants hypersensitive to the lethal effect of ionizing radiation. We isolated several ionizing radiation sensitive mutants from mouse cells. The mouse lymphoma L5178Y cell mutant M10 is defective in DNA double-strand break repairs and is hypersensitive to ionizing radiation. Stackhouse et al (Mutation Research 323, 47-52, 1994) reported the gene that corrects the radiation hypersensitivity of M10 cells is located on chromosome 5 and it is tentatively assigned to the 5q14 to 5pter region. The XRCC4 gene is located on chromosome 5 and is required for the repairs of DNA double-strand break in mammalian cells. Without XRCC4, cells are hypersensitive to ionizing radiation and defective for V(D)J recombination.

To analyze complementation of the radiosensitivity characteristics of M10 cell, the pME18S vector carrying the GFP, GFP-XRCC4 ORF or XRCC4 ORF-GFP was introduced into M10 cells by DNA transfection, and stable transfectants were selected by use of the blasticidin S resistant marker cotransfected pMAM2BSD. The clones, XRCC4 sequences and expressing GFP fusion protein, were corrected for radiation sensitivity similar to that of parental cell, L5178Y (Fig. 17). pME18S GFP showed radiation sensitivity of M10 cells.

Our results demonstrate that human XRCC4 cDNA complemented the ionizing radiation hypersensitivity of M10 cells.

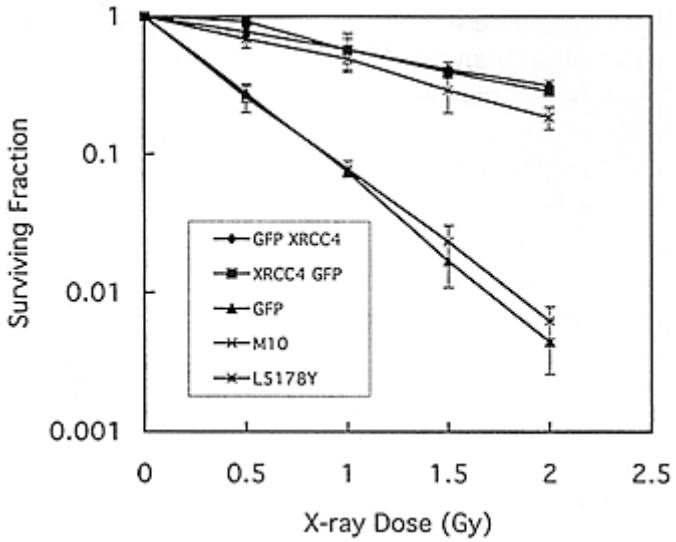

Fig.17. Cell survival after ionizing radiation of transformants. X-ray survival of wild type L5178Y cell, mutant M10 cells, mutant M10 cells transformed with GFP human XRCC4 fused cDNA, or with human XRCC4 GFP fused cDNA, or GFP cDNA.

Error bars represent standard deviation derived from triplicate experiments.

45. Radiation-Induced Mitotic Recombination in Human Lymphoblastoid Cells

Kouichi Tatsumi, Yuko Hoki, Akira Fujimori, Ikuko Furuno-Fukushi and Akira Tachibana*

(*Kyoto Univ., Radiation Biology Center)

Keywords: *allelic loss, LOH, crossing-over, deletion, breakpoint*

A selectable mutation assay accompanying the real-time detection PCR was developed to analyse the second step in loss-of-function mutations, employing a human lymphoblastoid cell line (LCL) derived from an obligate heterozygote of 2,8-dihydroxyadenine urolithiasis, adenine phosphoribosyltransferase (APRT) deficiency. The proportions of mutant clones with loss of heterozygosity (LOH) for spontaneous mutations and those induced by 2 Gy of gamma-rays were 68 % and 92%, respectively. Determination of the gene dosage revealed that about one half of the spontaneously arising mutant clones and two-thirds of those induced by gamma-rays showed reduction to homozygosity of the constitutionally inactivated APRT allele. The breakpoints of mitotic recombinations and deletions were not distributed randomly, but clustered at the border of the paracentromeric heterochromatin region of the chromosome 16. In an ataxia telangiectasia (AT) cell subline in which a new inactivation mutation had been introduced into an APRT allele by the treatment with ICR-191, mitotic recombination rarely occurred and deletion predominated in spontaneous and X-ray induced APRT mutations (Table 5).

Table 5. Extention of LOH and copy number of inactivated allele in DAP-resistant mutant clones spontaneously arising and gamma-ray-induced from WR10-KY1cells.

Spontaneously arising			Gamma-ray -induced			APRT	D16S 266	D16S 265	D16S 308	D16S 298	D16S 159
Dosage 1	2	Total	Dosage 1	2	Total	(q24.3)	(q23.3)	(q21)	(q12.2)	(p11.2)	(p12)
0	0	0	0	0	0	L	L	L	L	L	L
0	0	0	0	0	0	L	L	L	L	L	R
5	3	8	3	12	15	L	L	L	L	R	R
0	1	1	0	1	1	L	L	L	R	R	R
0	0	0	0	0	0	L	L	R	R	R	R
2	1	3	3	3	6	L	R	R	R	R	R
7	5	12	6	16	22						

L and R denote loss and retention of heterozygosity, respectively.

46. Sprit-dose Fractionation Dose Not Mitigate Radiation-induced Intestinal Death in Atm-disrupted Mice

Takeshi Furuse, Yuko Noda and Kouichi Tatsumi

Keywords: *ataxia telangiectasia, LD50/8, intestinal death, crypt*

Mice homozygous for the disrupted Atm allele was reported to exhibit an extreme hypersensitivity to ionizing radiation (IR), and rapid death in particular was caused by the severe selective toxicity of the gastrointestinal tracts rather than global radiation toxicity (Barlow et al., 1996). The wealth of information regarding the deficient recovery of IR-induced damages in cultured cells from ataxia telangiectasia (AT) patients has not been tested to see if it holds true for in vivo circumstances by utilizing these Atm-disrupted mice. We tred to determine if these mice were in fact defective in recovery from the sublethal effect of acute doses of IR to the whole body by looking at responses to split-dose fractionations.

Mice in 129/SvEv background were subjected to total body irradiation (TBI) with 200 kVp X-rays at 72 cGy/min and obserbed for 30 days thereafter to determine survival in the clean-conventional environment. No wild-type (Atm+/+) mice died after a single irradiation at 6 Gy. Early deaths were noted, however, between the 4th and 9th day post-irradiation among mice receiving a single 12 Gy dose, and also between the 10th to 14th day among mice given a single dose of 8, 9 or 10 Gy. Histopathological analyses on the mice that died within 8days post-irradiation revealed severe epithelial crypt destruction in the intestine together with congestion in tissures including lung, liver, heart and brain, indicating that death was due to the gastrointestinal syndrome. Mice that died between the 10th and 14th day post-irradiation showed histological features of death from bone marrow syndrome, i.e., degradation of bone marrow and extravasation in the brain, heart and lung. Dose-response curves for intestinal death by the 8th day after single TBI indicated that the median lethal dose, LD50/8, was approximately 4.5 Gy, 11 Gy and 11 Gy for Atm-disrupted mice (Atm-/-), heterozygous mice (Atm+/-) and wild type mice, respectively. When wild-type mice were irradiated with two equal doses of 6 Gy separated by an 8-hour interval, they died between the 6th and 13th day post-irradiation, surviving significantly longer than those irradiated one at 12 Gy. In contrast, there was no delay in early death of Atm-disrupted mice receiving two doses of 3 Gy with an 8-hour interval, as compared with those irradiated once at 6 Gy. These resutts suggest that the capacity to recover from sub-lethal damage is impaired in intestinal crypt cells of Atm-disrupted mice.

47. Different Brain Morphologies from Different Genotypes in a Single Teleost Species, the Medaka (Oryzias latipes)

Yuji Ishikawa, Masami Yoshimoto, Naoyuki Yamamoto, and Hironobu Ito

Keywords: *brain, morphology, genotype, genetic variation, inbred strain, vertebrate, wild type, teleost fish, medaka*

In the teleost fish, medaka (Oryzias latipes), many inbred strains have been established from various origins including wild populations. Brains from five genetically different strains, which had been bred and raised under the same conditions, were examined to determine whether there is intraspecific genetic variation. A total of 25 brains from the wild-type strains (HNI-II, HB11A and HB32C) and from the body-colour mutant strains (Hi3 and HO5) were fixed, and the external features of the brains were examined under a stereomicroscope. The differences between the HNI-II brains and the Hi3 brains were the most remarkable in the external features. In order to carry out a volumetric analysis, the brains of all strains were cut into complete serial cryostat sections. Total brain volumes and relative volumes (in % of total brain volume) of the olfactory bulb, telencephalon, optic tectum, and cerebellum were calculated in each brain using a semi-automatic image analyzer. Statistical analysis showed that significant differences in the total brain volumes and the relative volumes of these subdivisions exist not only between wild-type and mutant strains, but also among wild-type strains. Thus, our results demonstrate that the strains with different genotypes possess large variation in brain morphology. This is the first report to demonstrate that there exists intraspecific genetic variation in the gross brain morphology of a wild-type vertebrate.

Publications:

Ishikawa Y., Yoshimoto M., Yamamoto N. and Ito H. : Brain Behav. Evol., 53, 2-9, 1999.

---

48. Construction of EST Database for Genome Analysis of Bombyx mori

Kazuei Mita, Mitsuoki Morimyo, Kazuhiro Okano[1], Susumu Maeda[1] and Toru Shimada[2]

([1]RIKEN; [2]Univ. of Tokyo)

Keywords: *cDNA library, Bombyx mori, EST database, multi-cellular organism*

The silkworm, Bombyx mori, is an established model system for the study of insect physiology, biochemistry, development, metamorphosis and so on. Although numerous strains have been isolated, molecular biological information on the silkworm genome is limited. In order to study the gene expression patterns in the major organs of the silkworm, we initiated the construction of a cDNA database. This cDNA project is the first step in the genome analysis of Bombyx mori.The gene expression patterns significantly depend on tissues as well as developmental stages in multi-cellular organisms, unlike the case of uni-cellular organisms such as yeast. The cDNAs from which the ESTs are derived are present in libraries in proportion to the level of mRNA in the tissues from which the libraries were prepared. Thus, ESTs are subject to 'expression bias' for multi-cellular organisms. Therefore, we took the following strategy: cDNA libraries of various tissues (and different stages) were constructed by the directional cloning method. 1000 cDNA clones were chosen at random from each library and around 700-base nucleotide sequences from the 5' end of the cDNA were determined, followed by gene identification with a protein homology search in public protein databases. 1000 cDNA clones are enough to configure the abundantly expressed genes in the tissue from which the cDNA library is constructed, and the analyses of various tissues (and different stages) will provide a sufficient amount of ESTs for genome analysis. In addition, this approach explicitly represents the gene expression patterns of all genes identified. Another advantage of the cDNA catalog is to configure all members of related genes and display the whole pathway that the cells (or tissues) employ.So far, we have performed the analyses of 22 cDNA libraries: a culture cell (as a control), baculovirus-infected culture cell (2h post-infection, 6h p.i. and 12h p.i.), male and female fat bodies at the 5th instar, the 5th instar midgut, the brain (adult), the prothoracic gland at the 5th instar, the wing disc at the 5th instar day 4, the beginning of spinning and 2 days after spinning, pheromone gland (adult), the testis of the 5th instar larva and pupa, the embryo at 40 h and 96 h after fertilization and so on. We determined more than 16,000 cDNAs, and identified 6,000 genes that will cover a third of the total genes of Bombyx mori.Recently, we have succeeded in the construction of a high quality B. mori BAC library in collaboration with Dr. Pieter de Jong's group at Roswell Park Cancer Institute. Its average insertion size was estimated to be 168 kb with 11 times redundancy. The genome size of B. mori was estimated to be 530 Mb. If 6,200 independent ESTs are available, one BAC clone will have 2-3 EST markers on an average. Therefore, more than 6,200 independent ESTs are needed for the construction of BAC contigs. We initiated the construction of BAC contigs by hybridization using independent ESTs as probes.

Publications:

Mita, K., Morimyo, M., Okano, K., Shimada, T. and Maeda, S.: RIKEN Review, 22, 63-67, 1999.

49. Cockayne Syndrome-like Phenotypes in Mice Lacking the Xeroderma Pigmentosum Group G Gene

Tadahiro Shiomi, Yoshi-nobu Harada, Naoko Shiomi and Manabu Koike

Keywords: *xeroderma pigmentosum, xpg, mouse model, Cockayne syndrome, growth failure*

Patients suffering from xeroderma pigmentosum group G (XP-G) show complex clinical phenotypes. Some patients exhibit the signs and symptoms of both xeroderma pigmentosum and Cockayne syndrome (XP/CS). The reason for this combined phenotype is not known at present. Mutations in five genes, CSA, CSB, XPB, and XPG can cause the CS phenotype. Of these, CSA and CSB function exclusively in transcription and are required for transcription elongation and transcription coupled repair. These are not essential genes for cell survival and thus humans or mice defective in these genes can grow to an average age of 12 years or to adulthood, respectively. The XPB and XPD genes encode the subunits of the general transcription/repair factor TFIIH and hence only missense mutations in these genes are compatible with life. Apparently, some of the mutations in these genes impair transcription to a significant level to cause the XP/CS complex in a subset of XP-B and XP-D patients.

In contrast to the other four genes which have been implicated in CS, at present there is no direct evidence that XPG plays a role in transcription. A clue to a potentially vital role of XPG in survival was shown by the recent findings that XPG is required for transcription-coupled repair of oxidative DNA lesion thymine glycol by base excision repair and XPG stimulates the general genome repair of this lesion. Furthermore, it was found that missense mutations that inactivate the NER nuclease function of XPG do not affect thymine glycol repair or cause CS. Only mutations which gave rise to severely truncated XPG reduced the rate of thymine glycol repair and caused CS which is associated with growth retardation and short life span. In light of these findings, then, a likely cause of early senescence and death of xpg-deficient embryonic mouse cells and of xpg mice is the accumulation of oxidative damage including thymine glycol in the genome of the xpg mutant cells and mice. These lesions may cause the observed phenotypes by blocldng replication and transcription or by causing mutations in important regulatory genes. The fact that we did not find increased sensitivity of xpg null cells to ionizing radiation and H2O2 is not necessarily in disagreement with this reasoning. A 10-20 % reduction in the repair of thymine glycol (and other oxidative lesions such as 8-oxoG) may confer increased sensitivity that is difficult to detect in acute treatments. However, even a marginally perceptible decrease in repair of oxidative damage could lead to lethal phenotype over the long term. In this regard, we note that the XPG/CS cell lines with reduced thymine glycol repair capacity were not reported to have increased sensitivity to ionizing radiation or oxidative stress. Thus, a careful consideration of existing data on XPG mutants both in humans and in mice leads us to speculate that the premature senescence and death of xpg mice is caused by genomic instability induced by oxidative lesions which are repaired at a considerably slower rate in these mutants.

Publications:

Harada, Y., Shiomi, N., Koike, M., Ikawa, M., Okabe, M., Hirota, S., Kitamura, Y., Kitagawa, M., Matsunage, T., Nibaido, 0., Shiomi, T.: Mol. Cell. Biol., 19, 2366-2372, 1999.

50. Analysis of the Expression Pattern of the NPAT Gene after X-ray Irradiation

Yasuharu Ninomiya and Akiyo Nisiyama

Keywords: *NPAT, ATM, X-ray irradiation*

We identified the NPAT gene which shares a promoter with the ATM gene, and found the possibility that the NPAT gene, like the ATM gene, is also related to cellular responses to DNA damage or cell cycle control. We also confirmed that NPAT mRNA and protein expression peak at the G1/S stage and that NPAT is a substrate of cyclin E-CDK2, suggesting that NPAT plays a role in S-phase entry.

Then, to investigate the relationship between NPAT function and cellular responses to DNA damage, we studied the expression pattern of the NPAT gene after X-ray irradiation in human fibroblast cells.

We prepared RNA and protein from cultured cells synchronized by serum starvation after X-ray irradiation. The results of the analysis using the RNA and protein showed that the expression level of NPAT mRNA does not increase after X-ray irradiation, but the expression level of NPAT protein increases at 6 hours after X-ray irradiation. These results suggest that NPAT plays a role in cellular responses to DNA damage and the expression of the NPAT protein is regulated at post-transcriptional levels.

We are presently analyzing the function of the NPAT protein induced by X-ray irradiation.

51. Molecular Analysis of the Germ-line Mutation Induced by Ionizing Radiation

Masatake Yamauchi, Satsuki Tsuji, Toshiyuki Saito, Tada-aki Hori, Yoshiya Shimada, Yoko Ishii, Mayumi Nishimura, Toshiaki Ogiu, Masanori Okamoto, and Tsuneya Matsumoto

Keywords: *radiation, germ-line mutation, mice, scid, genetic instability*

Germ-line mutation induced by ionizing radiation is suspected as a cause for the increased risk of developing cancers in successive generations. However, no increased risk has been observed among children born to atomic bomb survivors exposed at Hiroshima or Nagasaki.

Our three-year project has aimed at investigating the germ-line mutation induced by ionizing radiation using experimental mouse strains, with or without a genetic background that affects radio sensitivity.

The Pc-1 locus is known as a hypervariable minisatellite. In the first fiscal year of the project, we analyzed the Pc-1 locus to detect the spontaneous level of the germ-line mutation (genetic instability). Molecular analysis of the Pc-1 locus in the offspring of CB17 revealed that the spontaneous mutation rate was about 5% under the ordinary breeding conditions used in our institute. The mutation frequency obtained here was 50% lower than that previously reported by another research group. This suggested that the spontaneous germ-line mutation might be considerably affected by the mouse strain and the breeding conditions. The offspring between CB17 and scid showed higher genetic instability compared to the parental strain, CB17, suggesting the scid mutation affects the genetic instability at the Pc-1 locus.

In the second fiscal year, we made modifications in experimental procedures to enhance the accuracy of the molecular analysis, and obtained a number of materials for statistical analysis of the germ-line mutation induced by irradiation. However, the scientific council of our institute declared that the modifications in the experimental procedures on the half way should have not been made, and decided the project should not be extended to the third fiscal year. The materials have been left unanalyzed.

52. Complementary DNA Structure of Mouse Nbs1 Gene That Is the Counterpart of Human Nijmegen Breakage Syndrome Gene

Toshiyuki Saito, Naohiko Seki, Atsushi Hattori[1], Masumi Abe, Mitsuoki Morimyo, Tada-aki Hori, and Yoichi Matsuda[2]

([1]Aisin Cosmos R&D; [2]Nagoya Univ.)

Keywords: *Nijmegen breakage syndrome, NBS1, checkpoint, cell cycle*

Nijmegen breakage syndrome (NBS) is an autosomal recessive disorder characterized by increased cancer incidence, cell cycle checkpoint defects, and cellular hypersensitivity to ionizing radiation. The NBS responsible gene (NBS1) product associates with Rad50 and Mre11 proteins both of which are highly conserved between yeast and human. Although NBS1 protein shows little homology to any yeast proteins, it is critical for the complex formation that is essential for repair of DNA double-strand breaks by radiation. To elucidate the important structures of the NBS1 protein, we started describing the divergence of the counterparts among different species.

A putative full length cDNA was isolated from a mouse testis cDNA library. The DNA sequencing revealed an 84 kiloDalton protein product composed of 751 amino acid residues. Amino acid sequence comparison between human and mouse NBS1 protein suggested conservation of two regions in the amino terminal (approximately 350 amino acids) and carboxy terminal half (110). A possible nuclear localization signal was found in the extreme carboxy terminal of the protein. Polymorphisms causing amino acid substitutions have been identified near the amino terminal of the mouse Nbs1 protein.

53. The Nuclear Localization Signal of the Human Ku70 Is a Variant Bipartite-type Recognized by the Two Components of Nuclear Pore-targeting Complex

Manabu Koike, Togo Ikuta*, Yoshi-nobu Harada, and Tadahiro Shiomi

(*Saitama Cancer Center Reserch Institute)

Keywords: *GFP, Ku70, microinjection, NLS, PTAC58/97*

Ku protein is a complex of two subunits, Ku70 and Ku80. Ku is suspected of participating in both DNA double-strand break repair and transcription. Since both of these processes take place in the cell nucleus, we have been investigating the subcellular localization and nuclear transport of Ku proteins. In the present study, we analyzed the subcellular localization and nuclear localization signal (NLS) of Ku70. Fusion proteins of Ku70 and green fluorescent protein (GFP) transiently expressed in cells were clearly localized in the nuclei of interphase cells. Ku70 staining was distributed throughout both the nucleus and the cytoplasm in late telophase to early G1 phase cells. The NLS of Ku70 was located at the region composed of 18 amino acid residues. This region overlapped with the Ku80- independent DNA-binding domain reported previously. The Ku70 NLS consisted of two basic subregions and a nonbasic intervening region. All the subregions were necessary for complete NLS activity. All of the basic amino acid residues in the basic subregions were conserved among mammalian and avian homologues, confirming their importance in the nuclear translocation of Ku70. The structure of the Ku70 NLS was a variant bipartite-type. The Ku70 NLS was mediated to target to the nuclear rim by two components of the nuclear pore-targeting complex, PTAC58 and PTAC97.

Publications:

1) Koike, M., Miyasaka, T., Mimori, T., and Shiomi, T. : Biochem. Biophys. Res. Commun., 252; 679-685, 1998.

2) Koike, M., Ikuta, T., Miyasaka, T., Shiomi, T. : Exp. Cell Res., 250, 401-413, 1999.

54. Production of Germfree Mice by Embryo Transfer

Masanori Okamoto and Tsuneya Mastumoto

Keywords: *aseptic technique, embryo transfer, germfree mice*

We have been investigating the application of reproductive biotechnology to the strain maintenance of laboratory animals. We have reported that cleaning of Sendai virus-infected mice is possible with an embryo transfer technique. Other researchers have reported that pathogenic microorganisms can be eliminated by transferring embryos harvested from infected animals to clean recipient mice. In the present study, we investigated the applicability of the embryo transfer technique to GF mouse production.

The procedure for producing GF mice by embryo transfer is outlined in the flow chart in Fig. 18. Mature female Jcl:MCH (ICR) mice served as donors for embryo collection after they were mated with mature males of the same strain. The embryo donors and males were mice purchased at 5 to 6 weeks of age and reared in our conventional animal facilities until 8 to 10 weeks of age, when they were used for the experiment. GF female C3H/HeMS mice, which had been maintained at our laboratory animal facility, served as recipients after having been mated with vasectomized GF male of the same strain. To prepare the vasectomized males, a flexible vinyl film isolator containing GF males was connected to the clean bench to be used for aseptic surgery. The spermatic duct of the males was cauterized with a soldering iron. Donor mice were superovulated with 5 IU of PMSG and hCG injected 48 h apart. After mating, the uterus of females with a copulatory plug (plug discovery: day 1) was perfused by modified Whitten's medium for embryo collection on day 4. Embryos of morphologically normal morula and blastocyst stages were stored in a dish containing medium. These embryos were immediately transferred to the uterus horn of recipients on day 3 with aseptic techniques. All sterility tests were performed, in accordance with the methods recommended by the Japan Experimental Animal Research Association with Thioglycollate (TGC), Cooked Meat Medium (CM), Potato Dextrose Broth and GAM semisolid (GAM) as clinical test media. To confirm that the embryos had been collected aseptically, the embryos collected from the donor mice were placed in embryo culture medium. Half of the embryo-containing culture medium was then combined with one of the following, TGC, CM or GAM, and the other half was combined with one of the other clinical test media. The test media were then incubated and observed at 20 or 37°C for two weeks.

The results of the sterility tests on the samples from the fresh feces of the nine vasectomized males, the water bottle rubber stopper, the inside floor of the vinyl film isolator and the gloves were all negative. Microscopic examination of the gram-stained and unstained fecal smears revealed no evidence of microorganisms or parasites in the vasectomized males. The results of the sterility tests of all culture media containing embryos showed they were sterile. The sterility tests of the fresh feces collected from the recipient mice and the inside of the isolator after embryo transfer and delivery were negative. The same test was also carried out on one of the mice cared for in the same isolator, and the result was negative. The autopsy and microscopy of the caecum and duodenum contents of one of the female mice from the same vinyl film isolator revealed no microorganisms or parasites. From the remaining two donor mice, we collected 17 and

12 morphologically normal morulae and blastocysts, respectively. These embryos were transferred to two recipients. One of the recipients, which had a copulatory plug, delivered a litter of six pups after the transfer of 12 embryos. When these pups were weaned, sterility tests on their fresh feces were negative.

The production of GF mice is necessary for the preparation of specific pathogen-free animals and the cleaning of infected animals. Hysterectomy has conventionally been used at our laboratory animal facility to produce GF mice. The average rate of weanlings to newborns produced using the hysterectomy technique over the past three years at our animal facility is 40.0% (156/390). The results of the present study suggest that GF mice can be successfully produced by embryo transfer in addition to conventional hysterectomy. This study shows it is necessary to simplify the experimental procedure from embryo collection to embryo transfer in order to efficiently produce GF mice. Embryo transfer to the GF recipient mouse using frozen-thawed embryo should be examined. It is desirable to establish a procedure for producing GF mice, combined with such reproductive biotechnology techniques as cryopreservation of embryos and spermatozoa; such a goal is useful for strain maintenance and transportation of GF mice, and in vitro fertilization.

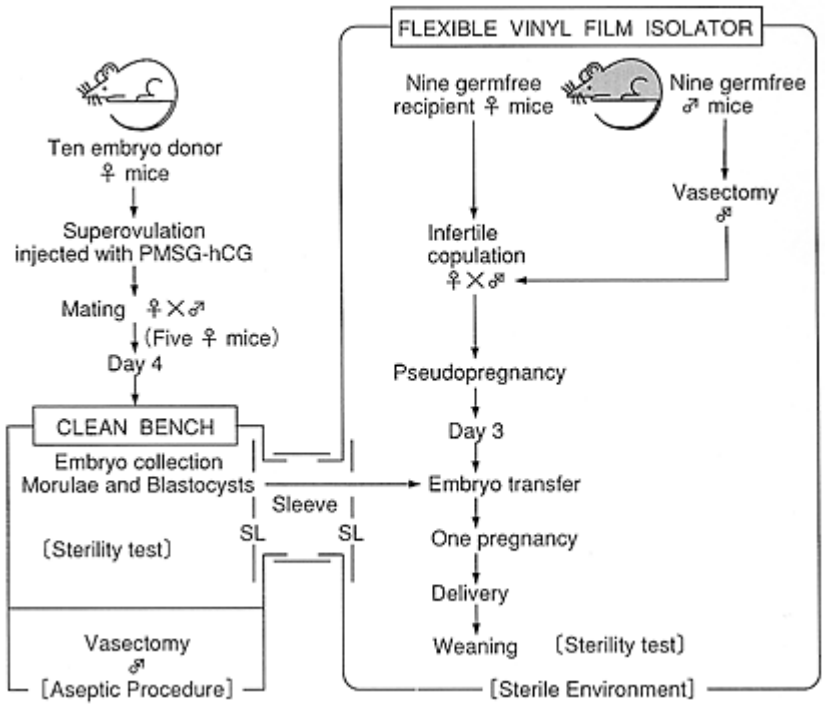

Fig.18. Experimental flowchart of germfree mice production by an embryo transfer technique.
SL: Sterile lock.

Publications:

Okamoto, M. and Matsumoto, T.: Exp. Anim., 48, 59-62, 1999.

55. Low Dose Pre-irradiation Reducing Prenatal Death and Congenital Malformation During the Late Period of Organogenesisi

Bing Wang, Harumi Ohyama, Keiko Haginoya, Takeko Odaka, Kaoru Tanaka, Eiichi Kojima, Takeshi Yamada[*] and Isamu Hayata([*]Toho Univ.)

Keywords: *radioadaptation, organogenesis, prenatal death, malformations, mice*

The adaptive response to ionizing radiation (radioadaptation) has been found in procaryotic and eucaryotic cells as well as in non-mammalian and mammalian systems, however, wether radioadaptation occurs during embryogenesis of mammalians is still uncertain.

In the present study, radioadaptation was demonstrated in embryogenesis of mice. Whole-body irradiation at the dose of 0-50 cGy was given for conditioning pregnant ICR mice on Day 9 to Day 11 of their gestation. Then their whole bodies were exposed to a challenging dose of 5 Gy on the next day. The numbers of living fetuses, prenatal deaths, and of living fetuses with external gross malformations were investigated on Day19. A conditioning dose of 30 cGy on Day 11 significantly increased the rate of living fetuses and reduced the incidence of congenital malformations. This indicates the existence of a critical dose and timing for conditioning in radioadaptation during the late period of organogenesis in mice.

The conditioning irradiation may have increased radioresistance of the fetuses by killing the radiosensitive cells which then reconstructed fetuses with a cquired radioresistant cells. Another assumption is that in decreased the speed of fetal development to allow the effective operation of cell-replacement repair when the challenging dose was given. A conditioning low dose pre-irradiation is believed to trigger changes in the expression of several genes whose products, though most of them are not yet identified, would be related to DNA repair and/or control of cell cycle progression, and induction of apoptosis. Further investigations on the mechanisms are underway.

56. Sequential Study on Pathogenesis of Lung Tumors in Rats Following Inhalation Exposures to Plutonium Dioxide Aerosols

Yoichi Oghiso, Yutaka Yamada and Kumiko Fukutsu

Keywords: *cytokinetics, dose, time, lung tumors, rats,* $^{239}PuO_2$

Sequential examinations were done on the cytokinetics of pulmonary alveolar macrophages(PAM) and lining epithelial cells, proliferative and neoplastic lesions in the lungs of female Wistar strain rats following the inhalation exposures to submicron-size, polydispersed and high-fired $^{239}PuO_2$ aerosols to analyse the pathogenetic processes of pulmonary carcinogenesis as well as the estimation of absorbed lung doses and times required for the development of lung tumors. The early appearance of multinucleated and micronucleated PAM was noted from the period of 1 to 3 months after exposures, when both nitric oxide(NO) and tumor necrosis factor(TNF) activities released from PAM stimulated in vitro with lipopolysaccharides and interferon-g were also significantly increased. The numbers of BrdU-labelled bronchiolar or alveolar epithelial cells significantly increased from 3 months and sustained up to 18 months after exposures. As correlated with these cytokinetic changes occurred in the initial to the late stages after exposures, histopathological findings showed that the early inflammatory lesions associated with exudation of blood leukocytes and alterations of respiratory tract epithelium were reduced, and then both pulmonary fibrosis and hyperplastic metaplasias increased from 3 months, while adenomatous or adenocarcinomatous lesions developed from 6 to 12 months after exposures. The appearance of primary lung tumors, almost all of which were benign adenomas and malignant adenocarcinomas, was observed in the dose range of 1 to 2 Gy from 12 months after exposures. These results indicate that the pathogenetic processes initiated by inflammation and cellular damage, are followed by the increase of proliferative and metaplastic lesions of the lining epithelium leading to the appearance and development of neoplasias at least from 1 year or later when the absorbed lung doses should be estimated to be 1 to 2 Gy after inhalation exposures to $^{239}PuO_2$.

Publications:

Oghiso,Y., Yamada,Y. and Fukutsu,K.: Abstracts for 11th ICRR, edt. M.Moriarty, C.Mothersill, C.Seymour, Radiat.Res., 279, 1999.

57. Validity of ^{241}Am as a Tracer of Plutonium Dioxides in Lungs in External Chest Counting

Nobuhito Ishigure, Hiroko Enomoto, Takashi Nakano and Jiro Inaba

Keywords: *Am-241, tracer, plutonium, external chest counting*

The most difficult radionuclides to measure by external chest counting are the isotopes of plutonium. They are detected through weak emission of low energy L X-rays. The plutonium treated in nuclear fuel cycle is usually accompanied by ^{241}Am produced from ^{241}Pu by β disintegration, which emits γ-rays of 60 keV with the emission rate of 0.36, being more penetrable than the L X-rays. The ^{241}Am could improve the detection limit of chest counting of plutonium by using it as a tracer of plutonium in the lungs. The ratio of lung burdens of ^{241}Am and ^{239}Pu was followed for 15 months by in vivo counting using rats inhaled with plutonium dioxide that contained 4 % of ^{241}Am in α-activity.

The suspension of $Pu(OH)_4$ was nebulized using a compressed-air operated nebulizer. The resultant droplets were passed successively through a heated tube to dry the droplets and on to a high temperature furnace heated to 1150°C to oxidize the dried particles. The size of the PuO_2 particles was 0.47 μm (AMAD) with the geometric standard deviation of 2.1. The inhalation was conducted using a multi-port nose-only exposure chamber, in which the aerosols flow vertically downwards. Young adult female Wistar rats, 12 weeks old and weighing 230 g at the time of exposure, were used. The lung contents of ^{241}Am and ^{239}Pu were measured with three thin NaI(Tl) scintillation detectors, 51 mm in diameter and 1mm in thickness which were housed within a shielded chamber with a 50 mm thick lead wall and a lining of 5 mm of copper and acrylic resin. The usual counting time was 1000 s.

The follow-up of lung content of ^{239}Pu indicated that a proportion of the initial alveolar deposition after exposure was well approximated with a two-component exponential function; about 77% was cleared at the half time of 53 days and 23% is at 794 days.

The ratio of ^{241}Am/^{239}Pu in the lungs is shown in Fig.19. The ratio was almost constant throughout the follow-up period, that is, the ^{241}Am was cleared from lungs at the same rate as ^{239}Pu.

The retention function of ^{239}Pu indicated that the ^{239}Pu inhaled in this study was cleared from lungs very slowly as compounds of Type S. Though the ICRP has assigned americium to Type M for all chemical forms, the ^{241}Am, assumed to be in a matrix of plutonium dioxide, behaves as if it were a material of Type S.

In addition this result suggests that the plutonium dioxide particles are retained in lungs in a particulate state for a long time after exposure and are hard to dissociate.

The concomitance of ^{241}Am with ^{239}Pu obtained in this study supports the validity of the proposal that in some cases ^{241}Am can be used as a substitute for isotopes of plutonium to assess them by external chest counting.

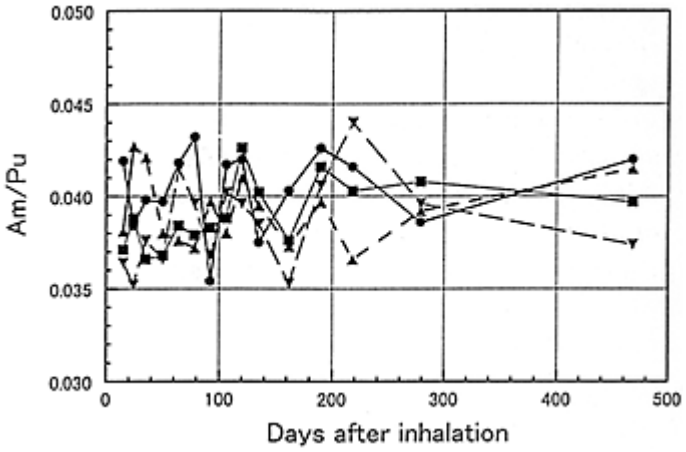

Fig.19. Ratio of lung burdens of ^{241}Am and ^{239}Pu.

Publications:

Ishigure, N., Enomoto, H., Nakano, T. and Inaba, J.: Radiat. Prot. Dosim., 79, 133-136, 1998.

58. Calculation of Monitoring Data for ^{239}Pu Using ICRP Dosimetric Models for Internal Exposure

Nobuhito Ishigure, Takashi Nakano, Hiroko Enomoto and Jiro Inaba

Keywords: *monitoring quantities, Pu-239, ICRP, respiratory tract model, biokinetic model*

Plutonium is one of the most important elements from the viewpoint of radiotoxicology and radiation protection. The International Commission on Radiological Protection (ICRP) recently revised the respiratory tract model (Publication 66) and biokinetic models for selected elements including plutonium (Publication 67). Using these new models, the monitoring quantities for inhaled ^{239}Pu such as lung retention, daily urinary and fecal excretion rate have been computed.

The following ICRP default values for the physical characteristics of the radioactive aerosols were used: AMAD (Activity Median Aerodynamic Diameter) = 5 μm and 1 μm, geometric standard deviation = 2.5, particle density = 3 g/cm^3, particle shape factor = 1.5. The subject exposed to the aerosols is the ICRP reference worker doing light work: light exercise with the ventilation rate of 1.5 m^3/h for 5.5 h + sitting with the ventilation rate of 0.54 m^3/h for 2.5 h.

As well as the monitoring quantities, the conversion coefficients from the measured monitoring quantities to the effective dose have been obtained. An example for the daily fecal excretion rate is shown in Fig.20, (a) is for Type M compounds and (b) for Type S compounds. It is shown that the estimated effective dose based on the feces analysis depends significantly on the types of compounds and the AMAD of aerosol particles.

In addition to the graphical representation, the computed monitoring quantities have been represented approximately by summation of exponential functions. For example, the fecal excretion function F(t)of inhaled ^{239}Pu of type M compounds with the AMAD of 5 μm is approximated as

$$F(t)=2.269\exp(-1.018t) + 5.718\times10^{-4}\exp(-3.018\times10^{-2}t)$$
$$+ 1.500\times10^{-4}\exp(-2.322\times10^{-1}t) + 4.771\times10^{-5}\exp(-1.266\times10^{-2}t)$$
$$+ 1.859\times10^{-5}\exp(-3.699\times10^{-3}t) + 1.317\times10^{-7}\exp(-3.753\times10^{-7}t)$$
$$- 3.540\exp(-1.602t)$$

The present results provide useful data for the design of monitoring programs and for the interpretation of the monitoring results in occupational exposure.

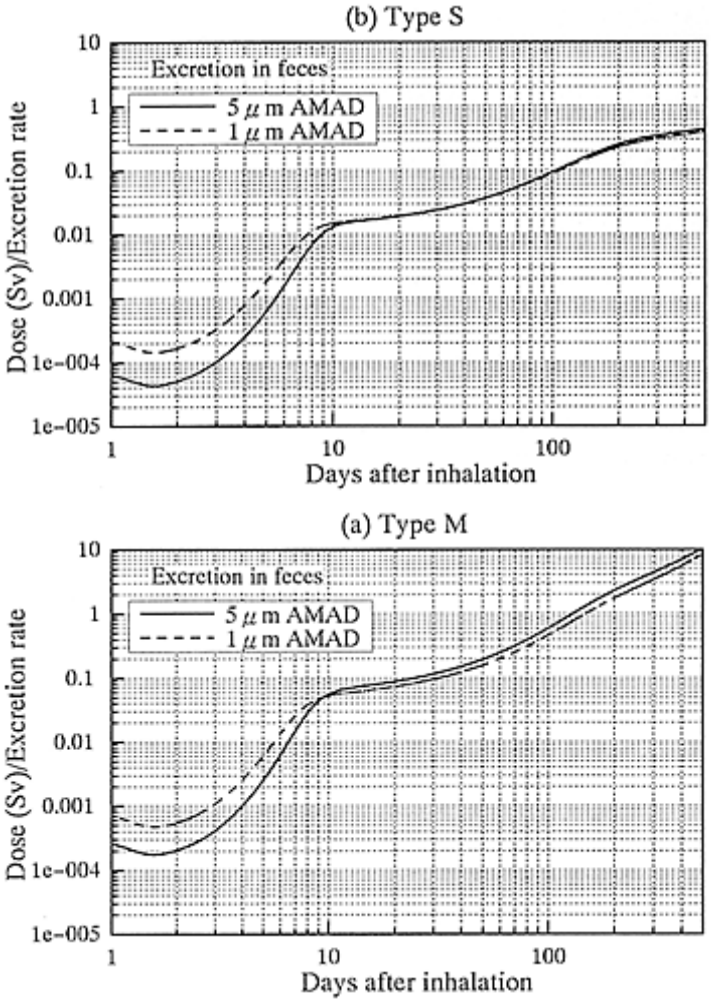

Fig.20. Conversion coefficients (Sv/(Bq/d)) for effective dose per daily fecal excretion rate of inhaled ^{239}Pu; (a) for Type M and (b) for Type S compounds.

Publications:

Ishigure, N., Nakano, T., Enomoto, H. and Inaba, J.: J. Health Physics, 33,415-423, 1998 (in Japanese, English abstract available).

59. Effects of Four CBMIDA Analogues on Removal of Plutonium in Rats

Satoshi Fukuda and Haruzo Iida

Keywords: *plutonium, CBMIDA analogues, oral administration, injection, rats*

We previously reported that the injection of a newly developed chelating agent, catechol-3, 6-bis(methyleiminodiacetic acid) (CBMIDA), removes plutonium particularly from the bones, more effectively than DTPA in rats. Nevertheless, the removed plutonium is later redistributed to the kidney, an undesirable phenomenon, in chelation therapy. Therefore, we wanted to survey the effects of four new analogues of CBMIDA on the removal of plutonium in rats and compare them with CBMIDA. After the intravenous injection of plutonium, CBMIDA and its analogues were administered daily, for 2 weeks by intraperitoneal injection or oral administration. The gathered data indicated that the intraperitoneal administration of two analogues significantly decreased the amounts of plutonium in the bones and liver ($p<0.01$), and the amounts in the spleen, testis and kidney were also reduced. In conclusion, the results indicate that among the tested agents, these two chelating agents present useful characteristics for chelation therapy in individuals contaminated with plutonium.

Publications:

Fukuda s. and Haruzo Iida: J. Health Phys., 33, 331-336, 1998.

60. Removal of Strontium by the Chelating Agent, Acethylamino Prophylidene Diphosphonic Acid, in Rats

Satoshi Fukuda, Haruzo Iida, Yueming Yan[*], Yuyuan Xie[*] and Wenzie Chen[*]

([*]Shanghai Institute of Materia Medica, China)

Keywords: *strontium, APDA, parenteral administration, oral administration, rats*

Studies on the effects of the chelating agent, calcium acetylamino propylidine diphosphonic acid (Ca-APDA) on the removal of radioactive strontium with two administration modalities were carried out in rats. The parenteral (intraperitoneal) administration of 150, 300 and 600 mg/kg Ca-APDA was carried out for 3 days, 10 min after exposure of the animals to the strontium injection. On the first day post-treatment, the retention of strontium in the whole body decreased to 90.1%, 83.9% and 35.1% of that of the control level, respectively. The strontium deposited in femur of the 600 mg/kg Ca-APDA group was lowered to 28.4 % of the control value. A single oral dose of 600 mg/kg Ca-APDA administered simultaneously with, or 10 min after, oral administration of strontium, gave a reduction of radionuclide retention in the whole body after 1 day to 42.9%, or 31.9% of the control, respectively; meanwhile the strontium deposited in the femur was reduced to 16.9% or 29.3% of the control. In conclusion, the results indicate the efficacy of the new agent, Ca-APDA, to remove radioactive strontium from the body, or to inhibit the strontium intestinal absorption, in radio-strontium contaminated individuals.

Publications:

Fukuda S. and Iida H.: Health Phys. 76, 489-494, 1999.

61. Muscarinic Acetylcholinergic Receptors in Human Narcolepsy: A Positron Emission Tomography Study

Yasuhiko Sudo, Tetsuya Suhara, Yutaka Honda, Toru. Nakajima, Yoshiro Okubo, Kazutoshi Suzuki, Yoshifumi Nakashima, Kyosan Yoshikawa, Takashi Okauchi, Yasuhito Sasaki, and Masaaki Matsushita

Keywords: *[^{11}C]NMPB, muscarinic receptors, narcolepsy, clomiplamine*

Objective: To investigate the function of the muscarinic acetylcholinergic receptor (mAchR) in narcolepsy and the effects of pharmacotherapy on mAchR.

Background: Muscarinic neural transmission serves as the main executive system in rapid eye movement (REM) sleep. Studies in canine narcolepsy reported an increase in mAchR in the pons.

Methods: mAchR of 11 drug naïve/free patients with narcolepsy and 21 normal controls were investigated using positron emission tomography (PET) with [^{11}C]N-methyl-4- piperidylbenzilate (NMPB). Measurements were done in the pons, thalamus, striatum and cerebral cortex. Seven of the 11 patients also underwent an additional PET scan after the alleviation of symptoms by pharmacotherapy.

Results: There were no differences in [^{11}C]NMPB binding between the control and drug naïve/free patients in all areas analyzed. At the time of on-medication PET scan, [^{11}C]NMPB binding in the thalamus was inhibited, but only to a small degree compared with that by anticholinergic drugs.

Conclusion: The present results do not support the notion that mAchR is the main site of action of pharmacotherapy in the marked clinical improvement of human cataplexy.

Publications:

Sudo, Y., et al.: Neurology, 51:1297-1302, 1998.

62. Correlation between intratumoral pO_2 and local control in radiation therapy for cervical cancer

Yoshiyuki Suzuki*, Takashi Nakano , Tatsuya Ohno , Atsuko Abe, Shinroku Morita , Yuzuru Niibe and Hirohiko Tsujii

(*Department of Radiology and Radiation Oncology, Gunma University School of Medicine)

Keywords: *hypoxic cells, radiation therapy, pO_2*

Objective: The existence of hypoxic cells is well recognized as one of the major factors for resistance against radiation therapy and local failure. However, in a clinical situation, correlation between intratumoral pO_2 status and local control is a matter of controversy.
Hence, we investigated this relationship for cervical cancer treated with radiation therapy.
Materials and Methods: This study involved 28 patients with squamous cell carcinoma of the uterine cervix who were treated with a combination of external and high dose rate intracavitary irradiation between 1995 and 1998. The pO_2 was measured by using a needle- type polarographic oxygen electrode and a pO_2-monitoring machine. The electrode was inserted 1 cm under the surface of the tumor before radiation therapy and at the 5th radiation therapy day or at 9 Gy (designated at The 5th Day).

Results: The mean intratumoral pO_2 before radiation therapy was 15.4±9.3 mmHg (range, 4.2-38.6 mmHg). The numbers of patients with O_2 =< 20 mmHg and > 20 mm Hg before radiation therapy were 22 and 6, respectively. The 3-year local control rates of patients with pO_2 =< 20 mmHg and > 20 mmHg were 65% and 100%, respectively, which meant no significant difference (p=0.19). At The 5th Day, the mean intratumoral pO_2 was 24.6± 11.7 mmHg (range, 7.2-66.4 mmHg), which was a significant increase compared to the pO_2 before radiation therapy (p=0.002). The numbers of patients with pO_2 =< 20 mmHg and > 20 mmHg at The 5th Day were 11 and 17, respectively. The 3-year local control rates of pO_2 =< 20 mmHg and > 20 mmHg at The 5th Day were 43% and 94%, respectively. The local control rate of the pO_2 =< 20 mmHg at The 5th Day was significantly lower than that of the pO_2 > 20 mmHg (p=0.016).

Conclusion: The increases in both intratumoral pO_2 at The 5th Day and the number of oxygenated tumors indicated that the reoxygenation phenomenon occurred within 1 week after initiation of radiation therapy. The significantly better local control for oxygenated tumors at The 5th Day indicated that reoxygenation by radiation had an important role in local control and an assessment of the intratumoral pO_2 status at The 5th Day was useful for predicting the local control in radiation therapy for cervical cancer.

63. C-erbB-2 Oncoprotein Expression Correlated with Local Control and Long Term Prognosis in Radiation Therapy for Adenocarcinoma of the Uterine Cervix.

Takashi Nakano, Kuniyuki Oka, Atsuko Abe, Shinroku Morita, and Hirohiko Tsujii

Keywords: *C-erbB-2 oncoprotein, radiation therapy, adenocarcinoma, uterine cervix*

Background: The correlation between the c-erbB-2 expression on cancer cells and radiation sensitivity or local control has not been evaluated.

Materials and Methods: A total of 47 patients with stage I-III adenocarcinoma of the uterine cervix were investigated for the prognosite significance of c-erbB-2 expression and epidermal growth factor recepter (EGFR) after radiation therapy alone. The c-erbB-2 expression and EGFR were detected by immuno-histochemical staining.

Results: C-erbB-2 oncoprotein was expressed on the surface membrane of cancer cells. Of 47 patients, 18 (38.3%) were positive for c-erbB-2 expression. The positive incidences for stages, I, II and III were 14.2%, 26.7% and 52.0%, respectively, increasing significantly advancing stages. As for the EGFR expression on the cancer cells, 15 patients (31.9%) were EGFR positive. No significant correlation between c-erbB-2 and EGFR expressions was observed. The 10-year survival rates for patients with c-erbB-2 expression was 28.2%, significantly worse than the 58.6% of those without c-erbB-2 expression ($p<0.01$). This difference was due to local control status rather than distant metastasis. The 10-year survival rate for patients with EGFR expression was somewhat better than that without EGFR expression, although it did not reach a statistical significance (60% vs. 37.8%). Multiple regression analysis indicated that c-erbB-2 oncoprotein expression and tumor volume were independent prognostic indicators.

Conclusion: The c-erbB-2 oncoprotein expression was associated with malignancy of the tumor and was an important predictor for local control and long term prognosis following radiation therapy for adenocarcinoma of the uterine cervix.

64. Clinical Assessment of Tumor/ Tissue Responses of Heavy Ions by Radiobiological Basis and Volume Effect for Treatment Optimization

Takashi Nakano, Atsuko Abe, Tatsuya Ohono, Atsuro Terahara, Shinitiro Sato and Suho Sakata

Keywords: *heavy ion therapy, treatment, cervical cancer*

Acute reaction of intestine was evaluated by frequency and intensity of diarrhea. This reaction due to carbon was significantly smaller than that by photon treatment. The dose volume histogram of the intestine by carbonbeam treatment was significantly smaller than by photon treatment. Chromosomal aberrations of lymphocytes of irradiated patients were analyzed according to the radiation biologic effect. RBE of carbonbeam treatment for chromosomal aberrations of human lymphocytes seems to be approximately 3.

Acute response analysis for cervical cancer patients treated with carbon beam therapy.

Acute reaction of bowel of 22 patients treated with carbon beam therapy was undertaken using the Dose Volume Histogram Analysis Method. The degree and frequency of the diarrhea and bowel movement were compared to those of conventional photon treatment.

Diarrhea developed significantly 3-4 weeks after initiation of radiation, and disappeared with medication. The incidence and degree of the diarrhea were significantly smaller in carbon beam treatment than the conventional photon treatment. There was no significant correlation beteeen acute small intestine reaction and Dose Volume Histogram of small intestine. Similarly, there was no significant correlation beteeen diarrhea and Dose Volume Histogram of large intestine.

Late reaction of rectum and intestine was analyzed by the Dose Volume Histogram Analysis Method. Grade of rectal bleeding and fistula formation, etc. were counted as late reaction according to RTOG late reaction score. Tumor volume irradiated with larger than 65 Gy showed an increase in late reaction. However, there was no apparent trend that patients with large DVH had higher incidence or higher grade of late reaction. Therefore, further intensive analysis in terms of hot spot dose distribution will be required.

65. Clinico-pathological and Molecular Biological Analysis of Heavy Ion Radiation Effect

Takashi Nakano., Yoshiyuki Suzuki., Tatsuya Ohono., Michiya Suzuki., Atsuko Abe., Shinroku Morita., Shinichiro Sato., and Shigeru Yamada.,Nobuyuki Miyahara., Hirohiko Tsujii., Hideo Niibe[*]

([*]Gunma University)

Keywords: *carbon beam therapy, cervical cancer, pO_2*

Objective: High-LET particles are believed to decrease radiation resistance of tumors originating from hypoxia and different radiation sensitivity in the cell cycle. However, no proof of the effect has been provided by clinical trial and related clinical research. Hence, we investigated the radiation biological aspect of the high-LET carbon beam therapy on cervical cancer.

Materials and Methods: This study involved 27 patients with stage 3B and 4A squamous cell carcinomas of the cervix treated with high-LET carbon beams and, as control, 28 patients of the same disease treated with conventional photon beams between 1995 and 1998. The pO_2 was measured by using a needle-type polarographic oxygen electrode and cell proliferation parameters were obtained with immunohistochemical staining.

Results: The cumulative survival rate and local control rate of 27 patients with advanced squamous cell carcinoma indicated the 3-year survival rate of 66.3 % and local control rate of 65 %. Of these, 23 patients were examined for tumor pO_2 status. The mean and median pO_2 of tumors before treatment were 16.5±9.0 mmHg and 13.7 mHg which were significantly increased to 24.4±9.7 mmHg and 25.2 mmHg, at The 5th Day, respectively (p=0.002). The numbers of patients with pO_2 =< 20 mmHg and > 20 mm Hg before treatment were 14 and 9, respectively. The 3-year local control rate of patients with pO_2 =< 20 mmHg and > 20 mmHg were 38 % and 44 %, respectively, which was not a significant difference (p=0.66). The local control rates of the pO_2 =< 20 mmHg and > 20 mmHg before treatment were 64.3% and 66.7 %, respectively, which were almost the same between them and not significantly different. The numbers of patients with pO_2 =< 20 mmHg and > 20 mmHg at The 5th Day were 8 and 15, respectively. The survival rates of the pO_2 =< 20 mmHg and > 20 mmHg at The 5th Day were 33 % and 51%, respectively, which was not a significant difference. (p=0.20). The local control rates of pO_2 =< 20 mmHg and > 20 mmHg at The 5th Day were 50.0 % and 73.3 %, respectively, which was not a significant difference. Recurrence did not correlate with tumor volume. Mitotic index of proliferating cell population of tumor (pMI) is considered to represent cell cycle speed of tumor. The 3 year local control rate of pMI=< 4% was 78.6 %, which was significantly poorer than the 38.5 % of pMI > 4%.

Conclusion: The increases in both pO_2 at The 5th Day and the number of oxygenated tumors indicated that the reoxygenation phenomenon occurred within 1 week after initiation of carbon beam therapy, the same as with photon beam therapy. The similar survival and local control rates for oxygenated tumors and hypoxic tumors before treatment indicated that tumor oxygenation status had not so important a role in local control

in carbon beam therapy. Tumors of high pMI or rapidly proliferating tumors developed significant recurrence. These results indicated that high-LET beam irradiation may overcome radiation resistant nature of anoxic tumors, but it can not overcome tumors with faster cell cycle speed.

66. Clinical Study for Proton Beam Therapy

Takashi Nakano, Shinroku Morita, Shigeo Furukawa, Tatsuaki Kanai, Kouichi Shibayama, Takayoshi Ishii, Takeshi Hiraoka, Atsuko Abe, Tatsuya Ohono and Hirohiko Tsujii

Keywords: *proton beam therapy, ocular melanoma*

A marker ring made of titanium was modified for responsibility of positioning in proton beam therapy. We developed a eye melanoma simulation without marker ring operation and applied this method for one patient with small ocular melanoma. Instead of marker operation, a read particle was placed on the sclera with a sticky anesthetic drug. Position of the read particle was determined according to the vessel of conjunctiva bulba. CT image was taken for the eye with the read particle and treatment planning was done with reference to its position. Patient setup was done succcessfully with the read reference. This method is rather reliable and not expensive.

This year, 11 patients with ocular melanomas were treated with proton beam therapy. By March 1999, 74 patients with ocular melanoma had been treated with protons. Of these 73 were treated to a radical intent; 60 % of them were located contiguous to or involved in the optic disk or macula which are critical organs relating to complications. The 5-and 10-year survival rates were 95% and 89%, respectively. Both 5-and 10-year local control rates were 88%. The 5-year cumulative retention rate of the involved eye after treatment was 70 %. These results suggested that proton beam therapy for ocular melanoma is one of the better treatment modalities.

Preliminary experiment for carbon ion treatment for eye disease was started with rats this year. 60 rat eyes were exposed with 4Gy and 16Gy. Normal tissue response of the eye to carbon beams will be obtained by next year.

Two groups of 30 female Wister Rats (8 weeks old) were irradiated on their eyes with a single irradiation of carbon beams of 4 Gy and 16Gy. Carbon beams of SOBP of 2cm were used. The diameter of the beams was 13mm to encompass the entire eye. The end points for this study are as following;

Examination will be performed at 3 months, 6 months, and 1 year after irradiation.

Retina Early and late reactions
    Histological finding (H&E), Electron microscopy, Electron Retino Graphy
Cornea Early and late reactions
    Histological finding (H&E), Electron microscopy
Lens cataract
    Slit lamp examination
Disk Early and late reactions
    Histological finding (H&E), Electron microscopy

So far the 3 month examination after irradiation has been performed. At 3 months Apparent changes of Electron Retino Graphy were observed for eyes irradiated with 16 Gy. Slight changes of ERG were observed for eyes irradiated with 4Gy.

67. The Cancer Functional Diagnosis and the Evaluation of Therapeutic Effects Using Magnetic Resonance Imaging and Spectroscopy

Masahisa Koga, Kyosan Yoshikawa, Takayuki Obata, Hirotoshi Kato, Susumu Kandatsu, Masanori Kanai, Junetsu Mizoe, Hirohiko Tsujii, Katsuya Yoshida, Tetsuya Suhara, Kazutoshi Suzuki, and Hiroshi Yoshioka

Keywords: *brain neoplasm, magnetic resonance spectroscopy, positron emission tomography, heavy ion therapy, choline*

Thirty-eight patients with brain neoplasms were treated by heavy ion therapy and then followed for more than 12 months. After heavy ion therapy, brain damage due to high radiation dose, radiation encepharitis and necrosis occurs occasionary. But CT and MRI of a recurrent tumor are similar to those of necrosis and encepharitis. Differential diagnosis of brain necrosis and irradiation with regrowth of brain tumor are difficult with MRI and CT.

We studied 1H-CSI and PET (11C-methionine and 18F-Deoxyglucose) in cases of gliomas before and after heavy ion therapy. We compared each pattern of MRS signal (NAA, choline, creatinine, and lactate), and PET images before and after heavy ion radiation therapy. In cases of brain necrosis, loss of choline signal was observed in 7 of 9 cases, but a slight accumulation of methionine was seen in the PET study. In cases of regrowth tumor, elevation of choline signal was significant. MRS diagnosis had 90% sensitivity, 76% specificity, and 83% total accuracy. Methionine PET diagnosis for the same group had 100% sensitivity, 71% specificity and 88% total accuracy. MRS study of brain tumor after irradiation is highly sensitive in the diagnosis of tumor necrosis or recurrance.

68. Functional diagnosis and evaluation of therapeutic effects of cancer using PET

Kyosan Yoshikawa, Katsumi Tamura, Yasunori Imai, Noriyo Matsuno, Masahisa Koga, Masakuni Kanai, Susumu Kandatsu, Hirohiko Tsujii, Tetsuya Suhara, Katsuya Yoshida,Kazutoshi Suzuki, Osamu Inoue[1], Fumio Shishido[2], and Hiroshi Fukuda[3]

([1]Ohsaka Univ.; [2]Fukushima Medical Univ.; [3]Tohoku Univ.)

Keywords: *Positron Emission Tomography, C-11 methionine, Cancer*

The role of PET in clinical diagnosis of cancer and the evaluation of therapeutic effects were studied. Positron emission tomography can demonstrate increased metabolic demand as visual images, and produces alternative information for diagnosis which can be used to complement morphological observations. The recent advance of PET scanner has enabled us to perform whole body PET scan. We studied if PET could be succesfully used for the detection and the evaluation of lung cancer. The lung tumor was detectable by whole body PET in 22 of 24 patients (91.7%). Six of seven (85.7 %) small lung tumors under 2.0 cm in diameter were detected and the minimal size of detectable tumor was 1.3 cm. The visual scale had a tendency to move according to the changes of SUV and size of the tumor. Tumor size of two (-) cases were 1.2 cm and 2.1 cm and SUVs of those were 0.98 and 1.04 respectively. We conclueded that F-18 FDG PET was useful for the detection of small peripheral type lung cancers.

The change of C-11 methionine uptake in tumor between pretreatment and post- treatment using HIMAC was compared with clinical prognosis. PET findings at pretreatment and post-treatment were compared with results of clinical observation of patients. We think that the level of accumulation in the tumor at pretreatment might correlate to the risk of metastasis and the reduction rate might correlate to local control level. If methionine does not accumulate at high levels in the tumor at pretreatment, methionine PET might not be a good indicator of patient prognosis, and we should use other indexes to evaluate patients prognosis after treatment in such cases.

69. Clinical application of autoactivation PET imaging derived from C-12 ion radiotherapy.

Kyosan Yoshikawa, Takehiro Tomitani, Mitsutaka Kanazawa, Tatsuaki Kanai, Masahiro Endo, Masahiko Koga, Hirotoshi Katoh, Susumu Kandatsu, Hiroshi Yoshioka[1], Junetsu Mizoe, Hirohiko Tsujii, Katsuya Yoshida[2], Kazutoshi Suzuki, Fumio Shishido[3], and Hiroshi Fukuda[4]

([1]Tsukuba Univ.; [2]Chiba Univ.; [3]Fukushima Medical Univ.; [4]Tohoku Univ.)

Keywords: *HIMAC, C-12 ion radiotherapy, autoactivation, patient fixation system*

Clinical application of PET imaging of autoactivation derived from C-12 ion radiotherapy was studied. For investigation of how the tissue metabolism would affect the RI distribution in the tissue, live and dead rabbits were irradiated using C-11 beam. When live rabbit was irradiated, the RI in the irradiated field decreased rapidly than when dead rabbit was irradiated. It calculated that the tissue metabolism reduced the RI activity about 50% less than non-metabolism. This mean that the estimation of the irradiated dose should be strongly concern about the regional metabolism, and this kind of examination should give us the important data to the analysis of clinical autoactivation PET image.

We also studied and designed the patient fixation system for autoactivation PET measuring. It is very important to perform the PET measurement under exactly same positioning of patient as HIMAC therapy. By this, it is possible to compare RI distribution with therapy planning. Now we have finished to design the fixation system, and it is under construction. The system will be available at the end of march in 1999.

70. Aging and Fading Effects on Registration Properties for Nuclear Tracks in CR-39

Hiroko Enomoto and Nobuhito Ishigure

Keywords: *CR-39, aging, fading, temperature, α-track, fission-track, bulk etch rate, sensitivity*

The effect of storage on track registration property of CR-39 has been studied. Pieces of CR-39 plate were irradiated with normally incident α-particles and fission fragments using a ^{252}Cf source prior and after their storage in air for one to six months at different temperatures of -80°C, -23°C, 4°C, 23°C and 35°C. The pieces were etched in the solution of NaOH with 7 mol・l^{-1} at 70°C for 4 hours.

Bulk etch rate(V_b) was obtained from the etch pit diameter (D_f) of fission tracks using the equation:

$$V_b = D_f / 2t$$

where t is etching time (h). Alpha-track sensitivity (S) was obtained from the etch pit diameters of α- tracks (D_a) and fission-tracks using the equation:

$$S=\{1+(D_a/D_f)^2\}/\{1-(D_a/D_f)^2\}-1$$

The observed changes in sensitivity of CR-39 during storage at different temperatures are shown in Fig.21: (a) shows the result for the aging experiment and (b) for the fading experiment.

It was found that both the bulk etch rate and α-track sensitivity tended to decrease with storage time and storage temperatures. The most significant effect was observed on the α-track sensitivity at 35°C, which was reduced by 55% for six months. It was found that the storage effect was attributable to some changes in the detector itself, and not to fading of latent tracks.

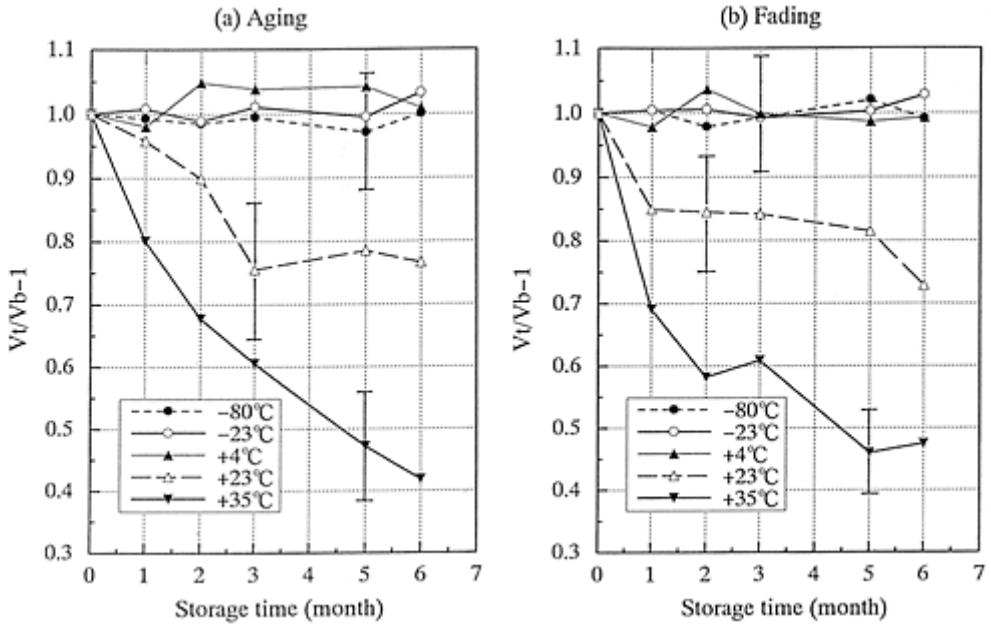

Fig.21. Changes in sensitivity of CR-39 during storage at different temperatures:
(a) shows the result for the aging experiment and (b) for the fading experiment.

Publications:

Enomoto, H. and Ishigure, N.: J. Health Physics, 33, 407-413, 1998 (in Japanese, English abstract available).

71. Second Nationwide Indoor Radon Survey in Japan

Kenzo Fujimoto, Masahiro Doi, and Shinji Tokonami

Keywords: *surveys, radon, indoor*

The second nationwide indoor radon survey was carried out in Japan during 1993-1996 with radon-thoron discriminative passive radon detectors after the first survey during 1985-91 with the passive radon detectors developed in Karlsruhe Nuclear Research Center since the first survey was suspected to overestimate the average indoor radon concentrations due to the thoron contribution to the detector. Twenty houses were selected in each prefecture in Japan for the survey. A total of 940 houses were measured. However, the total available data were reduced to 899 houses (Fig. 22) after scrutinizing the data to find out improper handling of the measurements. The radon monitor was installed in a bedroom or living room in each house for successive four three-month periods. The annual mean indoor radon concentration was estimated from the four measurements in each house. The mean, median and geometric mean of indoor radon concentration in Japan were obtained to be 15.5, 11.7 and 12.7 Bq m^{-3}, respectively, which were about 5 Bq m^{-3} lower than the results obtained by the first nationwide indoor radon survey. In the second survey the data were used only for the estimation of average concentration in Japan and each region but not for each prefecture since sampling number for each prefecture was less than 20. The radon concentration shows approximately a log-normal distribution. Seasonal variation of the radon concentration was found that the radon concentration was high in the fourth quarter (from October to December) and low in summer (from July to September). Variability among house structure types was also found that wooden houses have lower radon concentration than concrete or concrete block houses. The effective dose to the general public due to radon and its progeny was estimated to be 0.44 mSv y^{-1} in Japan using the same assumption given in the UNSCEAR 1993 report.

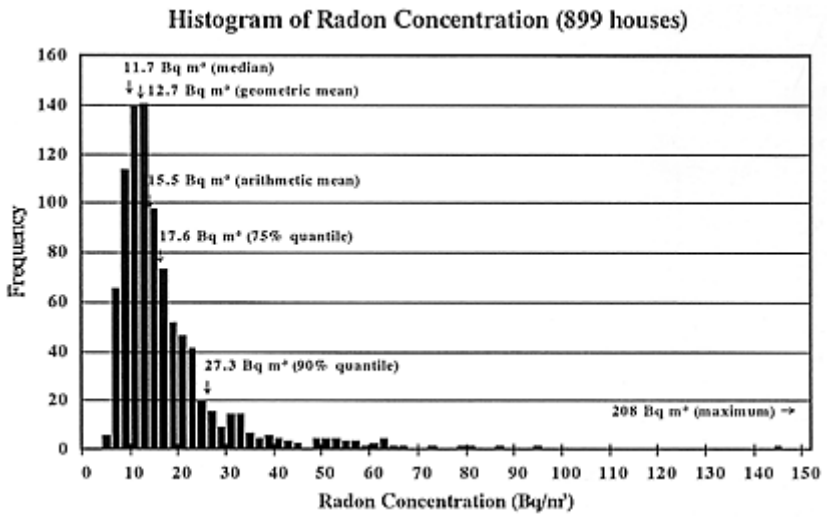

Fig.22. Histogram of indoor radon concentration.

Publications:

1) Fujimoto K. et al.: NIRS-R-32, 1997.

2) Fujimoto K. et al.: NIRS-R-34, 1998.

3) Sanada T., Fujimoto K., Miyano K., Doi M., Tokonami S., Uesugi M. and Takata Y.: Env. Radioactivity , 45, 129-137, 1999.

72. Variation of Cosmic-ray Intensity with Altitude in Asia: Results for Japan, China, and Korea

Masahide Furukawa, Shouzhi Zhang[1], Shian Zhao[1], Zhugang Jiang[2], Lixia Nei[2], Woonhyuk Chung[3], Masaki Matsumoto and Shinji Tokonami

([1]Laboratory of Industrial Hygiene, China; [2]Epidemic Prevention Station of Tibet, China; [3]Dept. Physics, Pusan National Univ., Korea)

Keywords: *cosmic-ray intensity, ionizing component, variation with altitude, Asia*

In the atmosphere, cosmic-ray intensity changes as a function of both altitude and latitude. To estimate the human dose from cosmic-rays, it is necessary to take into consideration these geographic factors. The purpose of this study is to investigate the actual distribution of cosmic-ray intensity by in situ measurement on a global scale.

A nationwide survey in Japan, including Mt. Fuji, Mt. Iwaki, Mt. Kaimon-dake etc., which aimed at the estimation of the variation of cosmic-ray intensity with altitude, was conducted from 1994 to 1998 by NIRS. The measurements were also carried out in the southern part of Korea in July 1996 and in Tibet, the highlands of China, in August 1998 by Korea-NIRS and China-NIRS co-operative research teams, respectively.

Cosmic rays were measured with a multichannel spectrometer with a 3"ϕ×3" cylindrical NaI(Tl) scintillation detector. Dose conversion analysis was made for the energy region from 3 MeV to 7 MeV, and the intensity was converted as the absorbed dose rate in air due to the ionizing component of cosmic rays.

Fig. 23 shows the relationship between cosmic-ray intensity and altitude which we obtained. The intensity increased from about 30 nGy/h to 140 nGy/h with increase of altitude. The minimum value of 28 nGy/h and the maximum value of 141 nGy/h were observed at sea level in Okinawa Prefecture, which is located in the southern part of Japan, and at the altitude of 4250 m in Tibet, respectively. Above 2500 m, the rate of change of the cosmic-ray intensity with altitude was estimated to be about 0.04 nGy/h/m. The rate from sea level to 2500 m was estimated to be about 0.01 nGy/h/m.

These results are considered to be useful information for the estimation of human exposure due to cosmic rays in Asian countries.

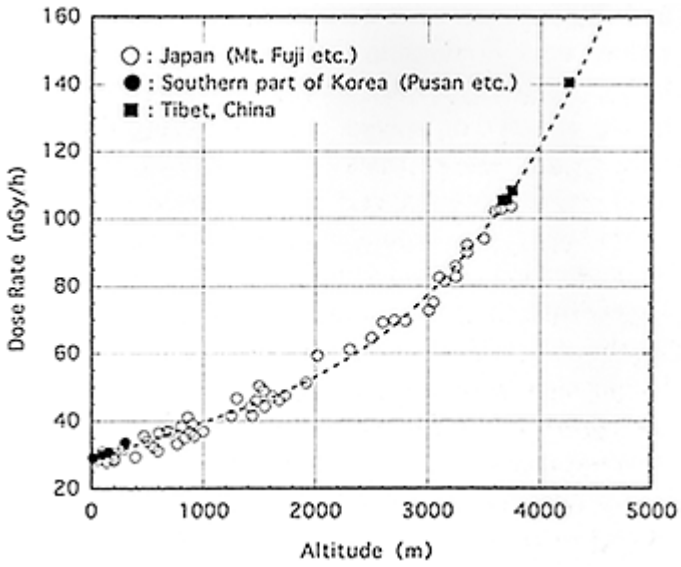

Fig.23. Variation of absorbed dose rate in air from ionizing component of cosmic rays with altitude.

73. Preliminary Survey on Radon and Thoron Concentrations in Korea

Shinji Tokonami, Masahide Furukawa and Woon Hyuk Chung*

(*Dept. of Physics, Pusan National Univ., Korea)

Keywords: *radon, thoron, survey, dose assessment*

A preliminary survey was conducted to determine atmospheric radon and thoron concentrations, and soil gas radon concentrations in South Korea. Over a one-year period, atmospheric radon and thoron measurements were made with a radon-thoron discriminative monitor, while soil gas radon measurements were made with a handmade radon monitor. The six measurement sites in the present survey were Pusan, Daegu, Daejon, Gongju, Iksan and Seoul. A polycarbonate film and a CR-39 detector were used as detectors for the radon-thoron discriminative monitor and the soil gas radon monitor, respectively. The detectors were replaced every 2-3 months during the survey period so as to observe seasonal variations of the concentration.

Table 6 summarizes the annual mean indoor and outdoor radon concentrations at each site. In terms of the radon concentration indoors and outdoors, the relative standard deviations derived from the counting data were estimated to be around 10-20%. The houses in Gongju and Daegu have mud walls and the others concrete or bricks. High indoor radon concentrations in Gongju may arise from the lack of ventilation in the living room because at one house one person stayed at home during the night only. In the case of Daejon, furthermore, the radon level might be enhanced because there are many radon hot springs around the measurement site. The outdoor radon concentration appears to be somewhat higher than the typical value of 10 Bq/m^3 mentioned in the UNSCEAR report. The mean outdoor to indoor concentration ratio (O/I ratio) is estimated to be 0.6. Relatively high thoron levels were observed in some areas. There is little variation on the indoor and outdoor thoron concentrations throughout the survey period at all the sites. The thoron levels fall in the range of 10 to 90 Bq m^{-3}. This finding suggests that attention must be paid to existence of thoron for the accurate dose assessment. The soil gas radon concentration was observed in the range of 3.9-23.1 kBq m^3. In particular, a remarkably high soil gas radon concentration was found in Daegu. In spite of the high soil radon gas, the radon concentrations indoors and outdoors are lower than expected. Since the radon concentration seems to be related not only to geological aspects or meteorological conditions, but also to geographical features at the site, further investigation is needed.

Table 6. Annual mean indoor and outdoor radon concentrations (Bq m^{-3}) at six sites.

site	Pusan	Daegu	Daejon	Gongju	Seoul	Iksan
indoor	16.7	22.3	33.8	65.0	16.0	28.4
outdoor	12.4*	16.0	24.4	21.3	10.6	10.1
O/I ratio	0.74	0.72	0.72	0.33	0.66	0.36

*: incomplete data

O/I ratio: outdoor radon conc./indoor radon conc.

Publications:

Chung, W.H., Tokonami, S. and Furukawa, M.: Radiat. Prot. Dosim., 80, 423-426, 1998.

74. Effect of Phytate and Chitosan on the Accelerating Removal of ^{65}Zn in Rats

Yoshikazu Nishimura, An Yan[*], Hee Sun Kim[**], Yoshito Watanabe and Masae Yukawa

([*]China Institute for Radiation Protection; [**]STA Fellow)

Keywords: *Zn-65, Chitosan, Phytate, Biokinetics*

Radioactive zinc is produced by neutron activation and is sometimes contained in reactor coolant. It is known that naturally occurring phytate found in plant protein can reduce the availability of dietary zinc. Several investigators have confirmed that phytate forms an insoluble calcium-zinc-phytate complex in the intestinal lumen and reduces the reabsorption of endogenous zinc secreted into the intestinal tract. Chitosan is derived from chitin, which is a cellulose-like biopolymer distributed widely in nature, especially in crustaceans, insects, fungi and yeast. It is a natural chelating agent. The purpose of the present study was to investigate whether phytate and chitosan can be applied to animal and human bodies in order to reduce the bioavailability of radio-zinc.

Wistar strain male rats, 8 weeks of age, were used in this experiment. Four groups of rats were given the following dietary treatments: (1) Normal diet (Oriental Yeast Co., Tokyo) and 3 % phytate water, (2) Cubed diet containing 5% of chitosan and distilled water, (3) Cubed diet containing 5% of chitosan and 1 % phytate water, (4) Normal diet and distilled water. Each group consisted of five rats, and they were kept for about 1 week under these conditions. After that, ^{65}Zn chloride was administered orally using a stomach tube. Whole-body retention was then measured. To determine the initial dose of radio-zinc in each animal, whole-body measurements of ^{65}Zn were made immediately after administration and were followed periodically thereafter by in vivo counting with a small animal counter (Armac Model-446, Packard Instrument Co.). Fig. 24 shows the whole-body retention of ^{65}Zn in the rats after oral administration. The whole-body retention of ^{65}Zn decreased sharply in the rats given 3 % phytate water in advance of ^{65}Zn administration when compared with the control rats. The rats given 5% chitosan and 1 % phytate water also showed a significant reduction in radio-zinc. However 5 % chitosan did not have a significant effect on accelerating the removal of radio-zinc in rats. Previous studies have shown that 1% phytate is also not effective in reducing radio-zinc in rats. These results suggest that the effectiveness of phytate and chitosan in reducing the bioavailability of radio-zinc depends on the concentration of phytate and chitosan.

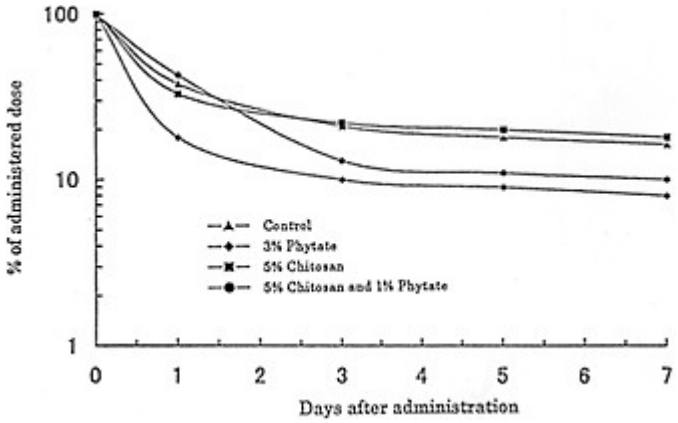

Fig.24. Whole-body retention of ^{65}Zn in rats after fed chitosan and phytate diet.

75. Computer Simulation of a Microorganic Ecology as a Self-sustaining System of Complexity

Masahiro Doi, Tetsuya Sakashita, Shoichi Fuma, Hiroshi Takeda, Kiriko Miyamoto and Yuji Nakamura

Keywords: *aquatic microcosm, protozoa, bacteria, intraspecific, interspecific competition, interaction, feedback system, self-organization*

Ecology is a nonlinear system of complexity structured by interactions among components and environment. Since very powerful mathematics and information tools are now available in terms of heuristic mathematical theory (e.g. cellular automata, genetic algorithm, etc.) and recent computer systems are highly sophisticated, it may be possible to describe how ecological systems and their components are likely to interact using computer simulation techniques by providing a simplified model on the basis of principles in the ecological systems, i.e., self-organization, feedback in response to disturbance, emergent behavior, diversity, etc.

This study explores a microorganic closed-ecosystem by computer simulation to illustrate symbiosis among populations in the microcosm that consists of the heterotroph protozoa, Tetrahymena thermophila B as a consumer, autotroph algae, Euglena gracilis Z as a primary producer and saprotroph Bacteria , Escherichia coli DH5, as a decomposer.

The simulation program is written as a procedure of StarLogoT, which was developed by the Center for Connected Learning and Computer-Based Modeling, Tufts University, which is a super set of StarLogo partly developed by the Media Laboratory, Massachusetts Institute of Technology. The virtual microcosm is structured and operated by the following rules.
Environment is defined as a lattice model, which consists of 10,201 square patches
Each patch has its own attributes, Nutrient, Detritus and absolute coordinates
Components of the species, Tetrahymena, Euglena and E. coli are defined as "turtles", and each turtle has its own attributes as X- and Y-coordinates, heading direction, age, life span potential, energy, breeding threshold, etc.
Each component of the species, Tetrahymena, Euglena and E. coli, lives its life by moving randomly, feeding (or consuming) a Nutrient from the "environment", and excreting its metabolic products to the "environment" as Detritus, breeds if it has more energy than the threshold and dies when its age reaches the life span potential if its energy is lost.
Only Euglena stores part of the sunlight energy as a potential food energy by photosynthesis process (biogeochemical Nutrient cycle), and E. coli breaks down the organic compounds of dead protoplasm or metabolic wastes (Detritus) and releases inorganic substances (Detritus food chain). A schematic figure of the Environment and species in the computer is illustrated in Fig. 25.

It was found that computer simulation is a valuable tool to illustrate symbiosis among populations in the microcosm, where a feedback mechanism acts in response to disturbances and interactions among species and Environment. In the simulation, the results of the population balance showed a probabilistic uncertainty and diversity, since some parameters, i.e., initial energy, initial age, life span potential and breeding energy

threshold, etc, showed significant stochasticity. The selection pressure might be high in the first critical minutes of operation, which consists of both intraspecific and interspecific competitions. More computer-based simulation trials must be carried out.

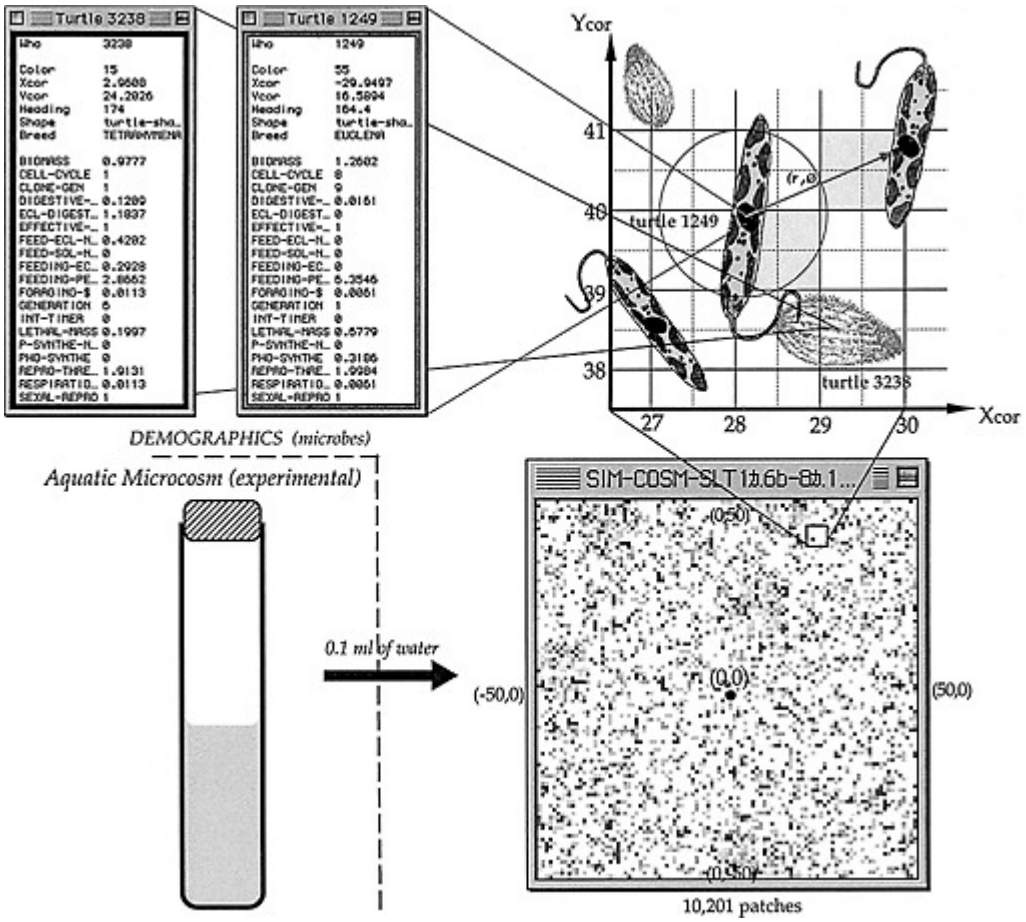

Fig.25. Conceptual scheme of the ecosystem in the computer.

Publications:

Fuma, S. et al. : Proceedings of the International Workshop on Comparative Evaluation of Health Effects of Environmental Toxicants Derived from Advanced Technologies, (Chiba, Japan), 131-144. 1998.

Kawabata, Z. et al. : J. Protozool. Research, 5, 23-26, 1995.

76. Bio-toxicity of $GdCl_3$ on the Movement Activity of Euglena Gracilis

Tetsuya Sakashita, Harald Tahedl*, Donat-P. Hader*, Masahiro Doi and Yuji Nakamura

(*Friedrich-Alexander Universitat, Germany)

Keywords: *Euglena gracilis, $GdCl_3$, motility, ECOTOX, toxicant*

Gadolinium is one of the rare earth elements, which is utilized in several industrial technologies, semi-conductor manufacturing being a typical example. In the nuclear fuel cycle, Gd is also used as a neutron absorber and is encountered in spent fuel waste disposal. The element may be regarded as a potential environmental toxicant, though its bio-toxicity is still open to study. For the purpose of environmental protection for human beings, not only the effects on the human body itself, but also those on the surrounding natural environment, that is the natural ecosystem, due to possible toxicants should be taken into account.

In this paper, a preliminary result on bioassay of microorganisms (Euglena glacilis) exposed to Gd is presented. The toxicity of Gd to microorganisms has already been reported, from the viewpoint of the long-term fatality measured by the temporal change in their population density. Fatality is not, however, a unique indicator to measure toxicity of materials. There may be other indicators which represent non-fatal, but serious effects on the healthy survival of living things. Then, this study discusses three parameters related to movement activity of bioassay organisms.

After logarithmically growing during one week, Euglena gracilis cells were cultivated for 5 days in a batch medium containing no organic carbon source to prevent heterotrophic growth, under conditions of continuous white light from fluorescent lamps (18 Wm^{-2}) at a temperature of 19°C. The cells were automatically mixed with toxic water containing $GdCl_3$ in the ECOTOX bio-monitoring system developed by Tahedl and Hader (Water Res., 33, 426-432, 1999) to observe the change in movement activity of the organisms, including motility (motile activity), r-value (gravitational orientation) and cell shape parameter (compactness). The motility represents the proportion of active cells among total cells. Euglena gracilis normally moves upward in the ECOTOX cell against the orientation of gravity. Randomness in moving orientation of microorganisms will increase with increasing toxicity in the environment. The degree of randomness in moving cells is expressed by the gravitational orientation parameter. The shape parameter represents the defensive structure of cells against toxicants.

Results of the experiment are illustrated in Fig. 26. These three parameters change with increasing concentration of $GdCl_3$. At addition of 50 μM $GdCl_3$, inhibitions from the normal state of both motility and r-value exceed 50% for each. This means that $GdCl_3$ may affect the activity of Euglena gracilis, though not fatally. The bio-toxic effect on the shape of the cells seems to be relatively small compared to that on motile activity. At lower concentration of $GdCl_3$, it seems that the gravitational orientation (r-value) is the most sensitive parameter indicating bio-toxicity of the element.

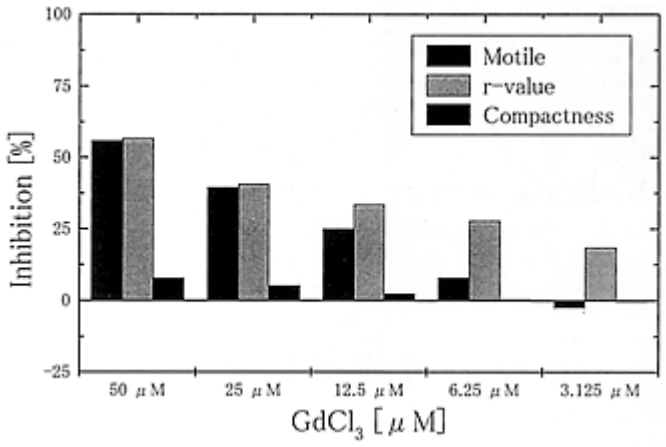

Fig.26. Changes in parameters to evaluate bio-toxicity of $GdCl_3$.

77. Simulation of the Long-distance Atmospheric Transport of Radon-222 Using a Lagrangean-type Model

Tetsuya Sakashita, Shinji Tokonami, Masahiro Doi and Yuji Nakamura

Keywords: *Rn-222, atmospheric transport, numerical simulation, eastern Asia*

Atmospheric transport of radon-222 (hereafter radon) with emanation sources in a distant and region has usually been numerically simulated using an Euler-type model;such a model offers an advantage of reduced execution time. However, the Euler-type model generally has a weak point that it includes a rather large numerical coefficient of 10^4 m^2s^{-1} for the horizontal diffusion process. Thus, a Lagrangean-type model, not including numerical diffusion procedure, was applied to the simulation of atmospheric transport of radon in this study. The study also evaluated exhalation rate of radon as an area-averaged value.

The atmospheric transport model used was based on a random walk method for a lot of Lagrangean particles, which has been described elsewhere. The horizontal diffusion was assumed to follow the Gifford function [Atmos. Environ., 16, 505-512, 1982]. The relational functions derived by Chino [JAERI 1334, 1995] were applied to the vertical diffusion of the particles. The area of the computational simulation covered eastern Asia, with the horizontal length reaching about 4,000 km. Radon was assumed as being emanated from the ground surface throughout the area at a flux of 1 radon atom cm^{-2} s^{-1}, except for an area of 240 km^2 surrounding the point at the National Institute of Radiological Sciences (NIRS) where the atmospheric concentration of radon was actually observed. The inflow flux was not taken into account, because it would give only a small contribution to radon concentration. To make a wind-field, data on grid point value (GPV) provided by the Japanese Meteorological Agency were used. The outdoor (atmospheric) concentrations of radon were measured with the Electrostatic Radon Monitor at NIRS during two periods from 19^{th} - 27^{th} Dec. 1997 and 20^{th} - 30^{th} Jan. 1998.

The observed radon concentrations, the calculated radon concentrations, and half of the calculated ones are shown in Fig. 27. A large discrepancy was found between the calculated radon concentrations (hereafter CR) and the observed. Therefore, several different radon exhalation rates were assumed to minimize the discrepancy, and the exhalation rate of 0.5 radon atom cm^{-2} s^{-1} was found as the best fit. As the result, the magnitude and the phase of the variation pattern on half of the calculated radon concentrations (hereafter HCR) seemed to be very close to those of the observed ones, especially in the term of 22^{th} - 24^{th} Dec. 1997. For these days, atmospheric pressure patterns typical in winter were seen in the weather charts. This mean observed radon concentrations during these days consisted mainly of radon which emanated from a remote land area, i.e. in China. Moreover, it seemed that the tracks of the radon particles transported from remote land surfaces during these days were followed well by the present model. In the second period of 20^{th} - 30^{th} Jan. 1998, the magnitude of HCR was almost the same level as the observed. No diurnal fluctuations were displayed in the HCR. The discrepancy seemed to be caused by a diurnal fluctuation of radon originated from an area near NIRS.

In conclusion, the simulation of long-distance atmospheric transport of radon from a remote land area was carried out by a Lagrangean-type model. The calculated radon concentrations with the exhalation rate of 0.5 radon atom cm^{-2} s^{-1} were very close to the observed ones. In addition, the results showed a Lagrangean-type model was effective for the estimation of an area-averaged exhalation rate of radon.

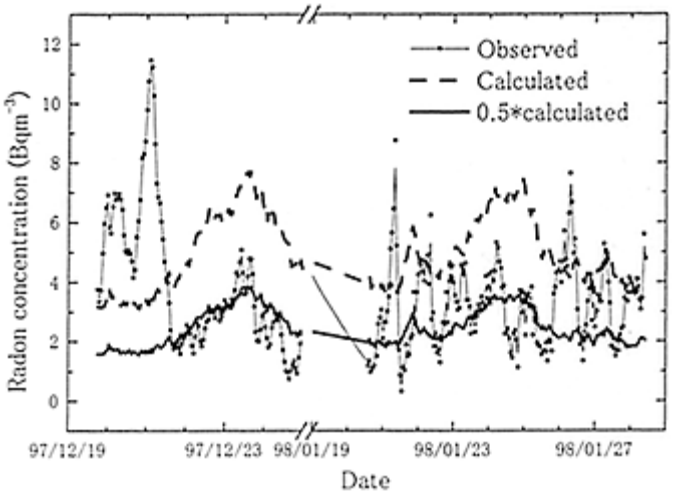

Fig.27. Historical data for radon concentrations.

78. Comparison of Rainout Algorithms Using the Deposition Flux of Air-born Beryllium-7

Tetsuya Sakashita, Masahiro Doi and Yuji Nakamura

Keywords: *rainout algorithm, Be-7, surface deposition, precipitation rate, meteorology, radiological environment*

Several algorithms have been proposed for to analyze the removal process of particles from the atmosphere, that is, the rainout process. In addition to very simple algorithms which include only a precipitation rate as an effective variable, other slightly more complicated algorithms have also been discussed, taking into account coalescence of a raindrop. A simple algorithm, however, seems to be more suitable for analyzing a lot of accumulated data on monthly deposition flux of atmospheric beryllium-7 (^{7}Be).

Four simple algorithms are evaluated in the paper. The first algorithm is the model from Kasibhatla et al. (hereafter K91) [J. Geophys. Res., 96, 18631-18646, 1991]. The algorithm proposed by Giorgi and Chameides (hereafter GC86) [J. Geophys. Res., 91, 14367-14376, 1986] is the second. These two algorithms are based on the scavenging coefficient being defined as the proportion of the precipitation content to the cloud liquid water content. The third one is the model parameterized by Mircea and Stefan (hereafter MS98) [Atmos. Environ., 32, 2931-2938, 1998]. The scavenging coefficient of this algorithm is defined as the function of the intensity of precipitation. In addition to these three algorithms, we provided a new algorithm (hereafter SDN99) for the rainout process under the following assumption: ^{7}Be concentration in the cloud where raindrops are formed, should decrease exponentially due to the supply of ambient ^{7}Be being cut-off at the time when heavy precipitation occurs.

The scavenging coefficient λ related to the rainout process is expressed as,

$$\lambda = \{1-\exp(-J \cdot \rho_w \cdot T_c/LH)\}/T_c \qquad (1)$$

where is the precipitation intensity; ρ_w, the density of water; T_c, the duration of the precipitation; L, the cloud liquid water content; and , the vertical extent of the precipitation.

The total deposition of atmospheric ^{7}Be is expressed as the sum of depositions by three processes, washout, rainout and dry deposition. In our newly developed model, the algorithm from ApSimon et al. [Atmos. Environ., 19, 113-125, 1985] was applied to the washout process, together with the dry deposition algorithm from Wesely et al. [J. Geophys. Res., 90, 2131-2143, 1985]. The monthly averaged scavenging coefficient was estimated from the rainout deposition flux which was calculated by subtracting the contribution of washout and dry deposition fluxes from the observed monthly ^{7}Be total deposition flux. The scavenging coefficients estimated from the observed monthly ^{7}Be deposition flux are shown in Fig. 28, together with those calculated by the four rainout algorithms. The estimated scavenging coefficients correspond to the monthly-averaged value during the 5-year period from 1986 to 1990.

Most of the estimated scavenging coefficients are distributed below a 5 mm/h precipitation intensity. The central estimates of scavenging coefficient and precipitation intensity are about 0.1 s^{-1} and 1.5 mm/h, respectively. The estimates by the GC86 model are closest to the observed among the four models. The results from the MS98 model are far from the observed. Above a precipitation intensity of 5 mm/h, the estimated scavenging coefficients are distributed widely. Therefore, comparison of the four rainout algorithms could not be carried out. A comparison in this region would be impossible, because a long precipitation with a strong intensity is rare. An analysis for each precipitation would be needed for this region.

In conclusion, the result by the GC86 algorithm showed the best fit to the observed scavenging coefficient of ^{7}Be, except for the time of heavy precipitation.

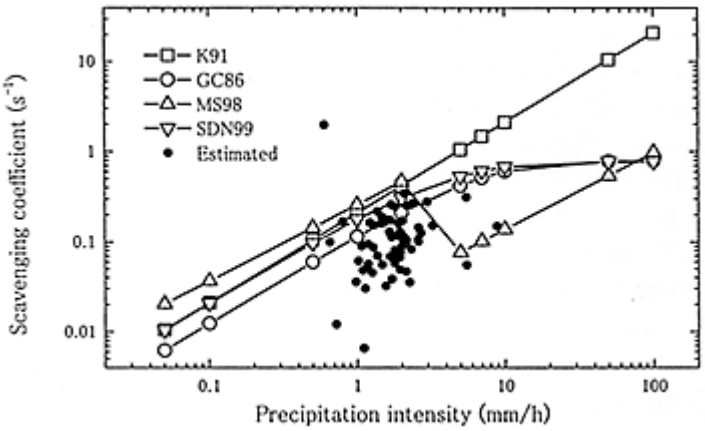

Fig.28. Predictions of scavenging coefficient of ^{7}Be by four rainout algorithms.

79. Transfer Factors of Chernobyl ^{134}Cs and Stable Cs for Mushrooms and Plants in a German Forest

Satoshi Yoshida, Yasuyuki Muramatsu and Werner Rühm*

(*University of Munich)

Keywords: *radiocesium, stable Cs, Cs-134, Cs-137, mushroom, plant, forest*

Radiocesium discharged through nuclear weapons testing and nuclear accidents is accumulated in forest ecosystems. Since removal of radiocesium from a contaminated forest is difficult, studies on the distribution and transfer of radiocesium in forest ecosystems are important in order to predict the future contamination of forest product. As chemical behavior of radiocesium is expected to be similar to that of stable Cs and the other alkali elements, analyses of stable elements must be useful to understand the long term behavior of radiocesium. It is known from agricultural systems that transfer factors for ^{137}Cs originating from global fallout are up to one order of magnitude larger compared to transfer factors for stable Cs. These findings can be explained by the difference of bio-availabilities between radionuclides and stable elements in the soils. In forest ecosystems, however, major fractions of anthropogenic radionuclides are found in the soil organic layers, where the mineral content usually is low and, on favorable conditions, the physico-chemical properties of stable elements and radionuclides are expected to be similar.

Detailed study on the transfer of radiocesium and stable Cs from soil to mushroom and plant was performed in a Norway spruce stand in Hochstadt, Germany. This site has been under investigation since 1987, and the soil layers from which certain species of mushrooms take up radiocesium were estimated by using the ^{137}Cs/^{134}Cs ratios. Soils were collected in 1993, 1995 and 1996. Four different mushroom species and one berry plant were collected in every year from 1993 to 1996. All samples were dried (70°C) and milled. Radiocesium was determined by counting with a Ge-detector. Stable Cs was determined by ICP-MS after digestion in Teflon PFA pressure decomposition vessels with acids (HNO_3, HF and $HClO_4$).

Transfer factors for ^{134}Cs and stable Cs were calculated on the basis of the soil layers, from which the corresponding species take up radioactive ^{134}Cs (Table 7). Most species take up ^{134}Cs from organic layers (L, Of and/or Oh). The resulting transfer factors for stable Cs were close to the corresponding transfer factors for ^{134}Cs, indicating that bio-availabilities of Chernobyl ^{134}Cs and stable Cs are similar. With this result, it is possible to predict the future contamination of radiocesium in understory vegetation of forest ecosystems: changes will occur due to physical decay of radiocesium, and due to migration of radiocesium to or from the rooting zone of the corresponding species. There will be no future change (aging effect) of the bio-availability of radiocesium in the organic layers for the investigated species and site.

Table 7. Transfer factors for mushrooms and berry plant for stable ^{133}Cs and Chernobyl ^{134}Cs, both calculated with respect to the layers from which radiocaesium is taken up (at Hochstadt, Germany).

Species	Horizon	Cs-134*	Cs-133
Lepista nebularis	L&Of	0.5 ± 0.1	1.0 ± 0.4
Xerocomus badius	L&Of&Oh	21.8 ± 2.3	13.1 ± 2.8
Hydnum repandum	Oh	43.6 ± 7.4	24.2 ± 1.9
Russula cyanoxantha	Oh or Ah	Oh: 2.9 ± 1.9 Ah: 15.3 ± 10.2	Oh: 6.2 ± 3.8 Ah: 10.5 ± 6.5
Vaccinium myrtillus (berry leaves)	L&Of	2.5 ± 0.5	3.9 ± 1.5

*The decay correction for Cs-134 was made as to 1986.

Publications:

Ruhm, W., Yoshida, S., Muramatsu, S., Steiner, M. and Wirth, E.: J. Environ. Radioactivity, 45, 253-270, 1999.

80. Improvement of Tc Separation Procedure Using a Chromatographic Resin for Direct Measurement by ICP-MS

Shigeo Uchida and Keiko Tagami

Keywords: *Tc-99, ICP-MS, environmental monitoring, ruthenium, rapid chemical separation*

Technetium-99 ($T_{1/2}$=2.1x10^5y) is produced by fissions of ^{235}U and ^{239}Pu with ca. 6% yield. The main sources of environmental ^{99}Tc are nuclear weapons tests and nuclear industries. To determine ^{99}Tc in environmental samples, chemical separation is necessary. We have been using inductively coupled plasma mass spectrometry (ICP-MS) for that purpose because the detection limit for ^{99}Tc is lower than the limits of other radiation counting methods. Further, measurement time for one sample is within a few minutes. However, ^{99}Tc separation and concentration are still required.

Recently, a novel extraction chromatographic resin (TEVA · Spec resin) has been shown to retain Tc efficiently and selectively from solutions. If we could introduce a diluted final extraction solution obtained from the resin into ICP-MS without any extra-chemical separation, the method would be more useful for environmental monitoring programs. The following conditions should be satisfied when the resin is applied for ICP-MS: 1) to remove Ru and other elements completely and 2) to keep the nitric acid strength in the final solution less than 1M. Ruthenium, which has an isotopic abundance of 12.7% at mass of 99, interferes with ^{99}Tc measurement by ICP-MS. In this study, we focussed on the Ru separation from environmental waters and the nitric acid strength for the final strip solution.

At first, the influence of the nitric acid strength on Tc and Ru absorption behaviour on the resin was investigated. Two hundred mL of both deionized and sea water samples were introduced into each prepacked column. Then, the resins were successively washed with 40 mL (10 mL x 4) of nitric acid solutions. The wash solutions were 1, 2, 4, 6 and 8M HNO_3 for the deionized samples and 1, 2 and 4M HNO_3 for the sea water samples. Then to strip the Tc from the resin, 10 mL (5 mL x 2) of 12M HNO_3 were introduced.

The results for both deionized and sea waters showed that Tc could not be removed with 1 and 2M HNO_3, although the wash solutions with higher than 4M HNO_3 could strip Tc from the resin. It was clear that a nitric acid content in wash solution higher than 4M was too strong to retain Tc on the resin.

For Ru, more than 95% passed through the columns with the sample solution. However, the remaining Ru on the resin was easier to remove with increasing nitric acid concentration. From this result, 12M HNO_3 is not suitable to strip Tc absorbed on the resin. Besides, a high nitric acid solution (e.g., > 1M HNO_3) damages the ICP-MS. A strip solution containing Tc should be diluted to less than 1M for direct measurement of ^{99}Tc with the instrument. It seems that 8M HNO_3 solution can be used for stripping Tc from the resin instead of 12M HNO_3, so that the dilution times could be lowered.

Table 8 shows results from application of the proposed procedure on up to a 2 L sea water sample with added ^{95m}Tc and ^{99}Tc. The second wash solution with 2M HNO_3 contained only 1.8% of 95mTc and the first and the second 2 mL strip solutions with 8M HNO_3 contained 29.4% and 68.8% of ^{95m}Tc, respectively.

The concentration of ^{99}Tc in each 2 mL strip solution with 8M HNO_3 was directly determined with the ICP-MS by ten dilutions with deionized water. The recovery of Tc by ^{99}Tc was almost the same as that by ^{95m}Tc. Ru was removed completely and the detection limit of ^{99}Tc by this procedure was 0.3 mBq L^{-1}.

Table 8. Recoveries of ^{95m}Tc, ^{99}Tc and ^{106}Ru in wash and strip solutions.

Solution		Volume	Recoveries (%)		
		mL	^{95m}Tc	^{99}Tc	^{106}Ru
Eluate	0.1 M HNO_3	2055	0	-	99.2
Wash solution	1st 2M HNO_3	20	0	-	0.7
	2nd 2M HNO_3	20	1.8	-	0.1
Strip solution	1st 8M HNO_3	2	29.4	29.3	0.0
	2nd 8M HNO_3	2	68.8	71.3	0.0
	3rd 8M HNO_3	2	0.0	0.0	0.0

Publications:

Uchida, S. and Tagami, K.: Anal. Chimica Acta, 357, 1-3, 1997.

81. Concentration of Global Fallout ^{99}Tc in Rice Paddy Soils Collected in Japan

Keiko Tagami and Shigeo Uchida

Keywords: *Tc-99, paddy field soil, anaerobic condition, activity ratio, accumulation*

Analysis data of global fallout ^{99}Tc in environmental samples should give useful information for predicting the nuclide behaviour. In this study, ^{99}Tc and ^{137}Cs in paddy field soil samples were determined and activity ratios of ^{99}Tc/^{137}Cs were calculated to clarify Tc mobility in the paddy soil environment.

Five soil samples were collected from the surface layer (< 20 cm) of paddy fields in Japan. After being air-dried and passed through a 2 mm mesh sieve, the samples were incinerated at 450°C. For the determination, 300 - 500 g of the incinerated soil samples were used. The chemical separation and ICP-MS method was described in our previous report (NIRS-63). During ICP-MS measurement, the counts for mass numbers 101 and 102 were checked to identify the separation of Ru from the solution. Both counts were almost the same as those of blank sample, thus, the amount of Ru existing in the sample solutions was assumed to be negligible. The average recovery of ^{95m}Tc from the contaminated soil sample was 58 +/- 6%.

The activities of ^{137}Cs in the soil samples were measured for 80000 s by a Ge detector system (Seiko EG&G) using 100 mL of each soil sample. The same volume standard solution (Amersham, QCY. 46) was used for the ^{137}Cs determination.

Table 9 shows the results of ^{99}Tc and ^{137}Cs. The ranges of ^{99}Tc and ^{137}Cs concentrations are 0.02 - 0.11 Bq/kg dry and 4.9 - 16.9 Bq/kg dry, respectively. The activity ratios of ^{99}Tc/^{137}Cs are in the last column, (2.0 - 5.2) x 10^{-3}. The activity ratio of ^{99}Tc/^{137}Cs from fission is now calculated as 3.0 x 10^{-4} with correction of decay out. The measured ratios in the paddy field soil samples are one order of magnitude higher than the theoretical one from fission.

The higher ^{99}Tc/^{137}Cs activity ratio in soil is presumably influenced by that of depositions containing rain and dry fallout. Ehrhardt and Attrep (1978) reported that the range of the activity ratio of ^{99}Tc/^{137}Cs in rain samples which were collected in the U. S. A. was (0.11 - 2.5) x 10^{-2} during 1961-1974. In Spain, Garcia-Leon et al. (1993) measured similar values of (0.3 - 12.3) x 10^{-2} in rain samples collected during 1984 - 1987. These ratios in rain samples were almost the same as those of the soils.

The mechanisms of Tc accumulation in paddy fields can be explained by the changes of Tc's chemical form in soil under the waterlogged condition. Generally, during the planting period, the paddy field soils are waterlogged and relatively low redox conditions are generated. Although Tc is expected to be in a highly soluble form as pertechnetate under an aerobic condition like that in surface soils, this transforms to insoluble lower oxidation forms through a combination of factors such as the redox condition and microbial activity. Thus Tc might have been accumulating in the paddy fields. However, it is still difficult to understand the ^{99}Tc

behaviour in the atmosphere and terrestrial environments because of the limited numbers of ^{99}Tc data in deposition samples. Our results, at least, lead to a tentative conclusion that more Tc might be fixed on the soil than we had expected before.

Table 9. Concentrations of ^{99}Tc and ^{137}Cs in paddy field soils in Japan on a dry weight basis and activity ratios of ^{99}Tc to ^{137}Cs.

Collection place and type of the soil	Collection year	^{99}Tc (Bq/kg)	^{137}Cs (Bq/kg)	$^{99}Tc/^{137}Cs$ ($x10^{-3}$)
Ogata Village, Akita Pref. Paddy soil	1991	0.11 ± 0.03	28.2 ± 0.8	3.9 ± 1.0
Omagari City, Akita Pref. Paddy soil	1992	0.034 ± 0.005	16.92 ± 0.64	2.0 ± 0.3
Morioka City, Iwate Pref. Paddy soil	1992	0.052 ± 0.01	10.13 ± 0.63	5.1 ± 0.1
Kawazoe Town, Saga Pref. Paddy soil	1991	0.022 ± 0.003	4.94 ± 0.47	1.5 ± 0.8
Imari City, Saga Pref. Paddy soil	1991	0.088 ± 0.015	16.84 ± 0.66	5.2 ± 0.9

(Note) ±: Counting errors in the measurements or statistical errors in calculation.

Publications:

Tagami, K. and Uchida, S.: Environ. Pollut., 95, 151-154, 1997.

82. Biokinetics of Radiocarbon Ingested as a Food in Rats

Hiroshi Takeda, Shoichi Fuma, Kiriko Miyamoto and Tetsuo Iwakura

Keywords: *radiocarbon, ^{14}C-wheat, biokinetics, rats*

Radiocarbon (^{14}C) is formed as a by-product of nuclear power generation, and a part of it is released to the environment. The reprocessing and disposal of spent nuclear fuel will also result in the release of ^{14}C into the environment. The relatively long half-life of ^{14}C (5,730 years), together with its mobility in the environment and in the living organism, make ^{14}C a radionuclide of considerable radiological significance. This nuclide is often released into the environment in the forms of carbon dioxide or bicarbonate. However, a part of such inorganic ^{14}C is transformed into organic ^{14}C by the photosynthetic process in plants and is transferred along the food chain and incorporated into the human body. In our previous study, we investigated the biokinetics of ^{14}C in rats ingested in the form of organic compounds (amino acids, fatty acid, mono-saccharide and nucleoside) or as an inorganic compound (bicarbonate) and clarified the higher radiation doses to the majority of the tissues from organic ^{14}C as compared with those from inorganic ^{14}C by a variety of factors. But, to date, a study on biokinetics of ^{14}C-labelled foodstuff and its dose estimation have not been made.

The present study deals with the biokinetics of ^{14}C-labeled wheat; wheat is one of the most common foodstuffs for humans. The ^{14}C-wheat was administered to Wistar strain male rats by mixed it with their pulverized food, and this was continued for 14 weeks. During these continuous 14 weeks, the rats were killed at various intervals and dissected to obtain more than 10 tissues. These tissue samples were combusted in an oxidizer which automatically adds an aquatic scintillator and the radioactivities in the combustion water were determined with a liquid scintillation counter. The data were expressed in terms of relative concentration, defined as the percentage of radioactivity administered per g of body weight of individual rat.

As can be seen in Fig. 29, the time course of relative concentration of ^{14}C determined in the tissues of rats during continuous ingestion of ^{14}C-wheat was different from tissue to tissue. It was suggested that biokinetics of ^{14}C would be dependent on the metabolic characteristics of each tissue. The concentration of ^{14}C in the liver increased at the fastest rate and reached an equilibrium level at 3 to 4 weeks after start of continuous ingestion. The equilibrium in other tissues, except for adipose tissue, was attained within 10 weeks after start of the ingestion. At the termination of the continuous ingestion (14 weeks), the highest ^{14}C concentration was found in the adipose tissue, followed by the liver, these concentrations were, respectively, 5 and 3 times higher than that in testes which showed the lowest concentration among all the examined tissues. Thus, a difference in a fairly wide range was observed in the concentration of ^{14}C incorporated into the tissues, even at an equilibrium condition of continuous ingestion.

For the purpose of radiation protection, the ICRP assumes that ingested ^{14}C is distributed instantaneously and uniformly throughout all organs and tissues of the body. However, as can be estimated from the results in the present study, dose calculation on the basis of this assumption will not necessarily lead to a proper dose assessment for ^{14}C ingested in foodstuffs.

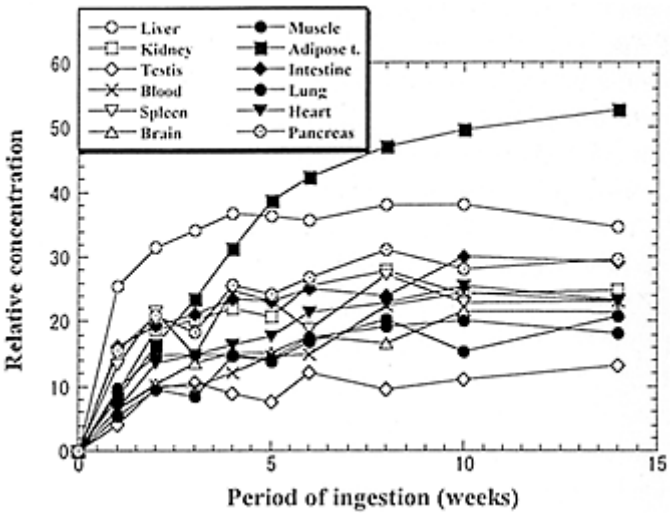

Fig.29. The concentration of ^{14}C in the wet tissues of rats during continuous ingestion of ^{14}C-wheat.

Publications:

Takeda H., Fuma S., Miyamoto K., Nishimura Y. and Inaba J.: Radiation Protection Dosimetry 79, 169-174, 1998.

83. A Species-defined Microcosm Test for Ecotoxicity of Manganese to Aquatic Microbial Communities

Shoichi Fuma, Hiroshi Takeda, Kiriko Miyamoto, Kei Yanagisawa, Yoshikazu Inoue, Nobuyoshi Ishii, Kazunori Sugai and Zen'ichiro Kawabata[*](* Kyoto University)

Keywords: *aquatic microcosm, ecological assessment, Escherichia coli, Euglena gracilis, manganese, model ecosystem, Tetrahymena thermophila*

Manganese has found a variety of uses in industry and agriculture owing to its physical and chemical properties. As a result, large amounts of anthropogenic discharges of manganese into ecosystems are a serious threat to all living things. In aquatic ecosystems, microbial communities play an important role in material cycles, which is known as the microbial loop. It is necessary to evaluate the effects of manganese on microbial communities for protection of entire aquatic ecosystems. However, ecosystems consist of many species that have complex interactions such as competition, predation and association, and so ecological effects at the community level cannot be deduced from the results of a single-species test. Microcosms are experimental ecosystems constructed in the laboratory to have some of the physical, chemical and biological elements of natural ecosystems, and they contain interactions among those elements as do natural ecosystems. In this study the authors tried to evaluate manganese toxicity to aquatic microbial communities using a species-defined microcosm.

The microcosm used in this study was developed by Kawabata et al. (J. Protozool. Res., 5, 23-26, 1995). It consists of flagellate algae Euglena gracilis Z as a producer, ciliated protozoa Tetrahymena thermophila B as a consumer and bacteria Escherichia coli DH5α as a decomposer. Each organism was axenic. The culture medium was a half strength modified #36 Taub and Dollar's salt solution containing proteose peptone. The medium originally contained 0.27 mg/L manganese. The microcosm was constructed in 250 mL polypropylene bottles, fitted with screw caps, by inoculating the organisms into 150 mL of sterilized medium, and then statically culturing them in an incubator with fluorescent lamps under 2500 lx and a 12h light-dark cycle at 25°C. In the microcosm the population change of each organism reached a steady state 50 days after inoculation as a result of interactions between the species. The microcosm systems on the 102nd day after the inoculation were exposed to manganese in the form of $MnCl_2$. A pure-culture system of each organism was also exposed to manganese. The population density of each organism was measured after the exposure.

Fig. 30 shows the changes in the population densities of the three species in the microcosm after the exposure to manganese. In the controls, the populations of each species remained almost constant for the duration of the test. At 5.5 mg/L and 27 mg/L, the populations of E. coli temporarily decreased compared with controls on the 13th day after the exposure. However, they recovered to the control levels on the 20th day, and then they were maintained at the control levels for the duration of the test. The populations of Eu. gracilis and T. thermophila were not changed.

At 55 mg/L, the populations of E. coli temporarily decreased compared with controls on the 6th day after the exposure. The decrease occurred earlier than at 5.5 and 27 mg/L. However, the populations almost recovered to the control levels on the 9th day, though they tended to be maintained at lower levels than controls after that. The populations of T. thermophila were slightly lower than controls, and those of Eu. gracilis were slightly higher than controls.

At 550 mg/L, E. coli first died out on the 9th day after the exposure, and then T. thermophila also died out on the 20th day. The populations of Eu. gracilis were slightly higher than controls. Extinction of E. coli can be considered to be a direct effect of manganese, because E. coli cultured alone also died out at the same concentration of manganese. On the other hand, the extinction of T. thermophila in the microcosm can be considered to be a secondary effect of manganese, because the populations of T. thermophila cultured alone were not significantly affected at 550 mg/L manganese. That is, it is thought that 550 mg/L manganese extinguished T. thermophila in the microcosm by extinguishing E. coli, because T. thermophila in the microcosm grazes E. coli as its staple food, and T. thermophila cannot exist in the microcosm medium without E.coli for more than 20 days. The same mechanism accounted for decrease or extinction of T. thermophila in the microcosm exposed to 500 or 1000 Gy gamma rays, pH 4 acidification, and 6.4 mg/L copper.

As described above, the microcosm test detected not only direct effects of manganese but also secondary effects at the community level. Single-species assessment, which is popular in ecotoxicological assessment, cannot detect the secondary effects. It is therefore concluded that microcosm tests are necessary for evaluation of ecotoxicity at the community level.

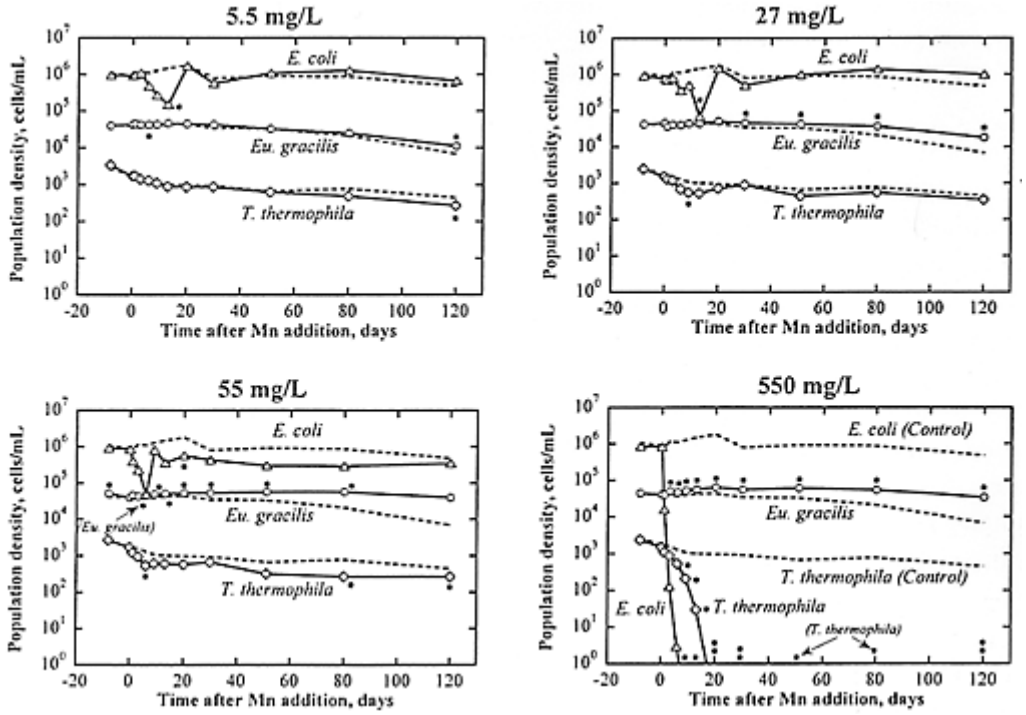

Fig.30. Effects of manganese on the populations in the microcosm. Solid lines represent results of the microcosm exposed to manganese. Broken lines represent results of controls. Values are the mean of three replicates. Asterisks indicate statistically significant differences from controls ($p < 0.05$, Student's t-test).

Publications:

1) Fuma S., Takeda H., Miyamoto K., Yanagisawa K., Inoue Y., Sato N., Hirano M. and Kawabata Z.: Int. J. Radiat. Biol., 74, 145-150, 1998.

2) Fuma S., Takeda H., Miyamoto K., Yanagisawa K., Inoue Y., Sato N., Hirano M. and Kawabata Z.: Comparative Evaluation of Environmental Toxicants, 131-144, Kodansha Scientific Ltd., Tokyo, 1998.

84. Accumulation of Iodine in Soil

Yasuyuki Muramatsu, Satoshi Yoshida and Atsushi Tanaka[*](*Kaken Co.)

Keywords: *iodine, soil, accumulation, ICP-MS analysis*

Iodine is an important nutrient element because of its role in the thyroid gland of humans and animals. From a radioecological viewpoint, considerable attention should be paid to the levels and behavior of radioiodine in the environment. In our previous studies using radioiodine tracer we found that soils have high ability in adsorbing iodine. In this study we have studied the levels of iodine in soil samples collected from various places in Japan.

An outline of the analytical method is as follows. Powdered samples (about 300 mg) were mixed with V_2O_5 in a small ceramic boat and placed in a quartz combustion tube (diameter: 20 mm and length: 450 mm). The end of the quartz tube was connected (using a ball-joint) to a trap containing 7 ml of H_2O, 0.4 ml of TMAH (tetramethyl ammonium hydroxide, Tama Chemicals Co. Ltd., 25% TMAH) and 0.1 ml of 5000 ppm Na_2SO_3 solution. A wet oxygen flow (50-200 ml/min) was passed through the tube during the heating at 1000-1100 C for about 15 min. Sample solutions were adjusted to 10 ml by adding H_2O. Iodine concentrations were determined with ICP-MS (Yokogawa PMS 2000).

Analytical results on the iodine concentrations (mean values of 2 - 3 analyses) in typical Japanese soils are shown in Table 10 together with the data on rocks typically found in Japan. Iodine concentrations in soils range from 0.63 to 44.9 ppm (on a dry weight basis). Average iodine concentrations are 32 ppm for Andosol (upland fields), 8.6 ppm for Yellow soil (upland fields), and 1.6 ppm for Gray lowland soil (lowland fields) and Gley soil (lowland fields).

These data also indicate that the iodine levels in upland soils are much higher than those in common crustal rocks in Japan. It is interesting to note that the concentrations of iodine in Andosol of upland fields are very high, even through the samples are collected from different places in Japan. The levels are about 3 orders of magnitude higher than those in the parent materials (i.e. basalt and andesite), suggesting that Andosol has specifically higher ability for iodine accumulation than the other soils analyzed in this study. Since the sorptions of iodide (I^-) and iodate (IO_3^-) on common clay minerals such as kaolinite, bentonite, quartz and allophane are usually not very high, it is expected that organic materials and/or microorganisms may play important roles in the accumulation of iodine in soils from water, e.g. rainwater, irrigation water. Entering of fallen plant materials, on which iodine was deposited from the air, into the soil environment also seems to be important in the accumulation pathway.

Autoclaving treatment of soils resulted in a significant decrease of the sorption of iodide (I^-), while that of iodate (IO_3^-) did not change markedly. The decreased iodide sorption in the autoclaved soil was recovered by incubation of the soils with a small amount of fresh soil. Microorganisms and/or their products (e.g. enzymes) may be participating in the sorption processes of iodine.

There is a marked difference in the iodine concentrations between lowland soils (rice paddy soils) and upland soils, as shown in Table 10. Iodine concentration in the 8 rice paddy soils studied was on average 1.6 ppm. This value was significantly lower than that in the 8 upland soils (average: 23 ppm) we analyzed. This suggested that iodine could be expected to be eluviated from rice fields through reclamation and rice cultivation under flooded conditions. The decrease of iodine from the flooded soil is due to the reducing conditions (low Eh) created by the effects of soil microorganisms.

Table 10. Iodine concentration in major soil types in Japan and in the possible parent materials.

Sample types*	Code	Sampling location	ppm I (dry)
Upland soils	F-007	Mito/Ibaraki	32.6
Andosol	F-015	Shiojiri/Nagano	26.0
(Andosol)	F-025	Kimotukigun/Kagoshima	24.2
	F-045	Rokkasho/Aomori	44.9
	F-064	Kawasaki/Kanagawa	33.0
		Mean (5)	32.1
Yellow soil	F-017	Toyohashi/Aichi	11.3
(Orthic Acrisol)	F-021	Fukuyama/Hiroshima	2.8
	F-068	Takayama/Gifu	11.8
		Mean (3)	8.6
Lowland soils (paddy soils)	P-013	Kumagaya/Saitama	0.63
	P-015	Mito/Ibaraki	1.93
Gray lowland soil	P-028	Oomagari/Akita	1.64
(Dystric Fluvisol)	P-038	Koriyama/Fukushima	2.76
	P-050	Kashihara/Nara	0.92
		Mean (5)	1.58
Gley soil	P-012	Kumagaya/Saitama	1.32
(Dystric Gleysol)	P-042	Gamougun/Shiga	1.46
	P-068	Nakakanbaragun/Niigata	2.08
		Mean (3)	
Possible parent materials for soils			
Basalt		JB-1 (GSJ)	0.028
Andesite		JA-2 (GSJ)	0.004
Granodirite		JG-1 (GSJ)	0.005

* Soil names recommended by FAO/UNESCO are described in brackets.

** Rock samples are standard rocks of the Geological Survey of Japan (GSJ).

Publications:

1) Muramatsu, Y. and Wedepohl, K.H.: Chemical geology, 147, 201-216, 1998.

2) Yoshida, S., Muramatsu, Y. and Uchida, S.: Radiochimica Acta, 82, 293-297, 1998.

3) Muramatsu, Y. and Yoshida, S.: Geomicrobiology Journal, 16, 85-93, 1999.

85. The Fate of ^{137}Cs in the Coastal Seas of Japan and Resultant Dose from Intake through Fishery Products

Teruhisa Watabe, Mitsue Matsuba and Setsuko Yokosuka

Keywords: *Cs-137, coastal sea, fishery products, dose commitment*

The relationship between the flux of the atmospheric ^{137}Cs at the surface of the sea and its concentration in seawater was studied in order to elucidate the fate of ^{137}Cs in the marine environment and to assess the radiological impacts to the human population. A simplified mathematical model which expressed the time course of radioactivity concentration in seawater in the first order kinetics was introduced to the present study:

$$\frac{dC}{dt} = F(t) - \lambda C \qquad (1)$$

where C is the time-dependent function of the ^{137}Cs concentration in seawater, F(t) is the flux of ^{137}Cs to the sea and λ is the constant of depletion of ^{137}Cs in the sea. As far as the fallout ^{137}Cs originating from nuclear test explosions in the past is of concern, it would be difficult to give a specific function to F(t) in the equation above because of the irregularity both in the time and scale of the events. The solution of Eq (1) can be given as follows when the initial concentration of ^{137}Cs in seawater is given as C_0 without the additional inputs.

$$C=C_0\exp(-\lambda t) \qquad (2)$$

If the deposition density of ^{137}Cs is observed at intervals of time, τ, the concentration in seawater is given as follows, when ^{137}Cs is supposed to deposit at the very beginning of the period of time, τ:

$$C=d\cdot F_1\cdot\exp[-\lambda(m-1)\tau]+\cdots+d\cdot F_1\cdot\exp[-\lambda(m-1)\tau]+\cdots$$
$$+d\cdot F_{m-1}\cdot\exp[-\lambda\tau]+d\cdot F_m$$
$$\sum d\cdot F_i\cdot\exp[-\lambda(m-i)\tau] \qquad (3)$$

where F_i is the deposition density at the i-th interval of a total of m times observations, d is the conversion factor from the deposition density to concentration in seawater with a dimension of L^{-1}. The parameters, d and λ, relating to the oceanographic properties of the sea are expected to be provided by means of a least square method when the data both on the deposition density of ^{137}Cs and on its concentration in seawater are given. If a set of data mentioned above is given along with the approximate values, d1 and λ_1 for the parameters, d and λ, the exact value of ^{137}Cs concentration in seawater can be estimated in the following formula as a result of the Taylor's expansion of Eq (3):

$$C_{ext}=C_{app}+(d-d_1)\left(\frac{\partial C}{\partial d}\right)_{d=d_1}+(\lambda-\lambda_1)\left(\frac{\partial C}{\partial \lambda}\right)_{\lambda=\lambda_1} \qquad (4)$$

where C_{ext} and C_{app} are exact values, namely, the observed concentration of ^{137}Cs in seawater and the concentration obtained by calculation, respectively. Eq(4) can be regarded as analogous to the equation expressed in the form, $Y=AX_1+BX_2$, and therefore, the second approximate values, d_2 and λ_2 can be derived by an ordinary least square method. The most probable values for the parameters d and λ thus can be determined when the difference between the results of the repetition of calculation becomes negligibly small.

If ^{137}Cs is released uniformly to the sea in the same manner as in the worldwide fallout, the infinite time integrated concentration of radioactivity in the seawater can be given as follows.

$$\int_0^\infty C dt = \lim_{n\to\infty}\left[d\cdot\tau\cdot F + d\cdot\tau\cdot F\exp(-\lambda\tau)+\cdots + d\cdot\tau\cdot F\exp(-n\lambda\tau)\right] = \frac{d\cdot\tau\cdot F}{1-\exp(-\lambda\tau)} \quad (5)$$

The dose commitment for a member of the public denoted by E and that for the whole population denoted by Eg affected by the release of ^{137}Cs to the sea would be provided as follows:

$$E = \Phi\sum_r I_r\cdot CF_r\cdot\int C dt, \qquad E_g = \Phi\sum Q_r\cdot CF_r\cdot\int C dt \quad (6)$$

where Φ is the dose intake conversion factor, CF_r is the concentration factor of ^{137}Cs by the species of marine organism r, I_r is the consumption rate of the organism r by an individual, and Q_r is the total catch of the organism r.

The parameters involved in Eq(3) were numerically derived for three regions of the coastal sea of Japan by regression analyses as mentioned above from radioactivity survey data reported since 1960 for past thirty years. Fig. 31 shows a schematic representation of the results obtained for the coast near Ibaraki and Fukushima Prefectures. It was anticipated that ^{137}Cs was retained in the coastal sea of Japan with a half-life period ranging from 5.3 to 6.8 years without a great difference between the Pacific Ocean and the Japan Sea. The integrated concentrations of ^{137}Cs in sea water were determined as 0.191, 0.173 and 0.120 mBq・a/l, respectively for the coasts of Ibaraki/Fukushima, Niigata and Fukui Prefectures as a result of the deposition at a unit density ($1MBq/km^2$). The resultant dose commitments to the respective populations would correspond to 4.5, 2.4 and 0.9×10^{-3} man・Sv through consumption of the coastal fishery products.

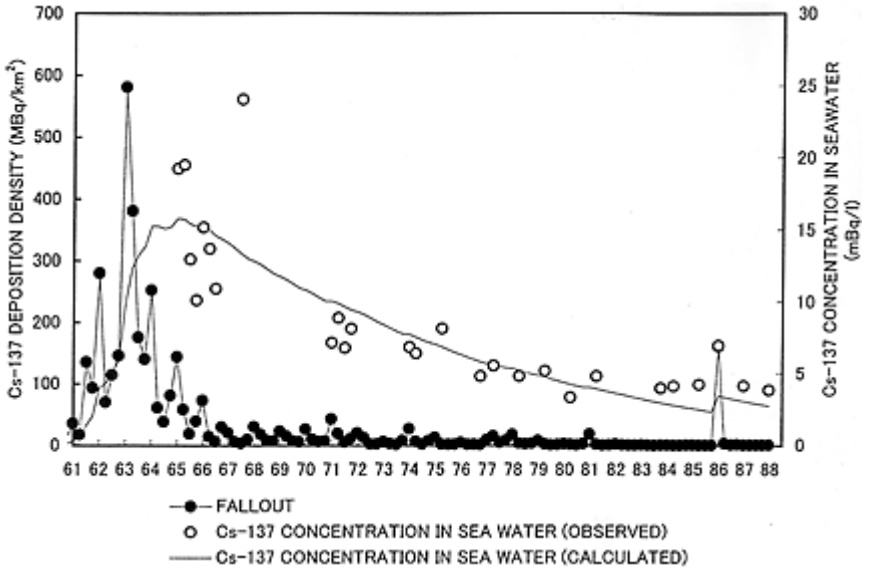

Fig.31. Time course of deposition of ^{137}Cs observed in Ibaraki and Fukushima Prefectures and the resultant changes in its concentration in seawater near the coast.

Publications:

Watabe, T., Matsuba, M. and Yokosuka, S.: Hokenbutsuri, 33, 151 - 161, 1998.